Amorphous Phase Formation in $In_xGa_{1-x}As$, $In_xGa_{1-x}P$ and $Si_{1-x}Ge_x$

Zohair Shakir Hussain

A thesis submitted for the degree of

Doctor of Philosophy

Of

The Australian National University

Australian National University

2013

This thesis does not include any material previously submitted for a degree or diploma at any university and to the best of my knowledge does not contain any material published or written by any other person except where due reference is made in the text.

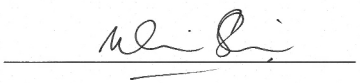

Zohair Shakir Hussain

Acknowledgements

I am indebted to Professor Mark Ridgway for his excellent supervision throughout my academic career at the Department of Electronic Materials Engineering at ANU. Without his support, patience and belief in me I would not be where I am today.

I would also like to thank Professor Werner Wesch, Dr. Elke Wendler, Dr. Leandro Araujo and Dr. Patrick Kluth for their advice and support during my PhD work. I have had a wonderful time working with my colleagues Dr. Bernt Johannessen, Dr. David Sprouster, Dr. Raquel Giulian, and Dr. Claudia Schnohr. Thanks are also due to David Llewellyn for his help with TEM sample preparation and microscopy. Dr. Kidane Belay has been invaluable for his help with maintaining and scheduling of the ion beam equipment.

A special thanks to Dr. Abid Ghous, Dr. Deepak Sardana and Kamran Khan for their unconditional friendship over the years.

Finally, I would like to thank my family, especially my wife Genevieve, my mum, and my kids, Azhar, Ahmed Yusef and Jahangir for their patience, love, and support which has enabled me to finish this thesis.

Publications

A list of publications resulting during the course of this PhD.

Lift-off protocols for thin films for use in EXAFS experiments
S. Decoster, C. J. Glover, B. Johannessen, R. Giulian, D.J. Sprouster, P. Kluth, L. L. Araujo, Z.S. Hussain, C.S. Schnohr, H. Salama,.F. Kremer, K. Temst, A. Vantomme, M.C. Ridgway , Journal of Synchrotron Radiation **20,** 426 - 432 (2013).

An in-situ heater for the XAS beamline (12-ID) in Australia
B. Johannessen, Z. S. Hussain, D. R. East, M. A. Gibson, J. Phys. Conference Series **430,** (2013).

Structural modification of swift heavy ion irradiated amorphous Ge layers
W. Wesch, C. S. Schnohr, P. Kluth, Z. S. Hussain, L. L. Araujo, R. Giulian, D. J. Sprouster, A. P. Byrne and M. C. Ridgway, Journal of Physics D-Applied Physics **42** (2009).

Rapid ion-implantation-induced amorphization of $In_xGa_{1-x}As$ relative to InAs and GaAs
Z. S. Hussain, E. Wendler, W. Wesch, G. J. Foran, C. S. Schnohr, D. J. Llewellyn and M. C. Ridgway, Physical Review B **79** (2009).

Atomic scale characterization of ion-induced amorphization of GaAs and InAs using perturbed angular correlation spectroscopy
R. Dogra, A. P. Byrne, Z. S. Hussain and M. C. Ridgway, Nuclear Instruments & Methods in Physics Research Section B-Beam Interactions with Materials and Atoms **266**, 1460-1463 (2008).

Amorphous phase formation in ion implanted $In_xGa_{1-x}As$
Z. S. Hussain, W. Wesch, E. Wendler and M. C. Ridgway, Nuclear Instruments and Methods in Physics Research Section B: Beam Interactions with Materials and Atoms **257**, 344-347 (2007).

Characterization of radiation damage annealing of recoil-implanted GaP
R. Dogra, Z. S. Hussain and A. K. Sharma, Materials Characterization **58**, 652-657 (2007).

X-ray absorption Spectroscopy and Small Angle X-ray Scattering studies of Metal nanoparticles using Synchrotron Radiation
M. C. Ridgway, P. Kluth, L. L. Araujo, R. Giulian, Z. S. Hussain, B. Johannessen, D. J. Llewellyn, C. S. Schnohr, D. J. Sprouster, D. J. Cookson and G. J. Foran, Chemistry in Australia **74**, 15-16 (2007).

Rapid amorphization in $In_xGa_{1-x}As$ alloys at temperatures between 15 K and 300 K
W. Wesch, E. Wendler, Z. S. Hussain, S. M. Kluth and M. C. Ridgway, Nuclear Instruments and Methods in Physics Research Section B: Beam Interactions with Materials and Atoms **242**, 480-483 (2006).

Atomic-scale structure of irradiated GaN compared to amorphised GaP and GaAs
M. C. Ridgway, S. E. Everett, C. J. Glover, S. M. Kluth, P. Kluth, B. Johannessen, Z. S. Hussain, D. J. Llewellyn, G. J. Foran and G. d. M. Azevedo, Nuclear Instruments & Methods in Physics Research Section B-Beam Interactions with Materials and Atoms **250**, 287-290 (2006).

Abstract

Amorphous semiconductors have found uses in an increasing variety of electronic and photonic devices over the last few decades, many of which are now commonplace. The ubiquitous Thin Film Transistor (TFT) LCD/LED flat panel display is a multibillion dollar per annum industry. Other examples include photovoltaic cells and night vision systems. A thorough understanding of the physical characteristics of this class of materials is of commercial, military, scientific and technological interest. In particular, a deeper understanding of the amorphisation process may assist in accelerating the uptake of this technology.

This thesis investigates the amorphisation kinetics of three semiconducting materials, $In_xGa_{1-x}As$, $In_xGa_{1-x}P$ and $Si_{1-x}Ge_x$, to gain an understanding of the damage production process in these materials via ion implantation. Ion implantation is a commonly used technique in the semiconductor industry for rendering materials amorphous due to the precise control it offers over the implanted ion fluence and ion species. All three of these materials are of technological importance for their use and development in fields such as solar cells for space applications, quantum well FETs, wireless LAN and GPS applications.

Ion implantation was performed using Ge ions to render $In_xGa_{1-x}As$, $In_xGa_{1-x}P$ and $Si_{1-x}Ge_x$ amorphous. Implantation induced disorder was quantified with Rutherford backscattering spectroscopy in the channelling configuration (RBS-C). EXAFS measurements were performed to study the local atomic structure of the crystalline material. Parameters such as bond length, bond angle and structural disorder were

deduced from the EXAFS measurements. These results were then correlated to RBS-C to help explain the amorphisation behaviour observed in $In_xGa_{1-x}As$, $In_xGa_{1-x}P$ and $Si_{1-x}Ge_x$.

It was found that distortion in both bond length and bond angle distribution was apparent for both $In_xGa_{1-x}As$ and $In_xGa_{1-x}P$ with the structural disorder primarily being accommodated by bond angle distribution. This leads to the presence of local regions of strain giving rise to preferential sites for stimulated amorphisation. The amorphisation kinetics observed in $In_xGa_{1-x}As$ and $In_xGa_{1-x}P$ are attributed to these pre-existing local strain regions. The structural disorder observed in crystalline $Si_{1-x}Ge_x$ was much reduced in comparison to the $In_xGa_{1-x}As$ and $In_xGa_{1-x}P$. Hence, amorphisation kinetics observed in $Si_{1-x}Ge_x$ differ from those observed in $In_xGa_{1-x}As$ and $In_xGa_{1-x}P$. It is hoped that the insights gained by this thesis into the amorphisation kinetics of these materials will help open up more avenues and application for the use of these and materials similar to these in the electronics industry.

Contents

List of Figures

Chapter 1 Amorphous phase formation in $In_xGa_{1-x}As$, $In_xGa_{1-x}P$ and $Si_{1-x}Ge_x$

1.1 Introduction

Compound semiconductors are the materials of choice for a number of well-established commercial technologies, as well as new cutting-edge classes of electronic and optoelectronic devices. Some examples of cutting-edge devices and applications include photo receivers for optic fibre transmission; high sensitivity and high resolution short wave infrared (SWIR) cameras (including those used for night vision and military applications); high frequency transistors for mobile phone communications; lasers and light emitting diodes [1-6].

The ability to manipulate material properties in a controllable manner is of great importance in almost all scientific and engineering fields. Using compound semiconductors provides an additional avenue to vary these properties by altering the composition or stoichiometry of these materials. For example, the bandgap energy of a ternary semiconductor compound can be varied by changing the composition of the constituent elements *(see Figure 1-1)*. The resulting properties are generally between the two binary extremes [7, 8]. For example, the ion fluence required to amorphise $Al_xGa_{1-x}As$ increases with increasing Al content [9], with AlAs requiring the highest ion fluence to render it amorphous.

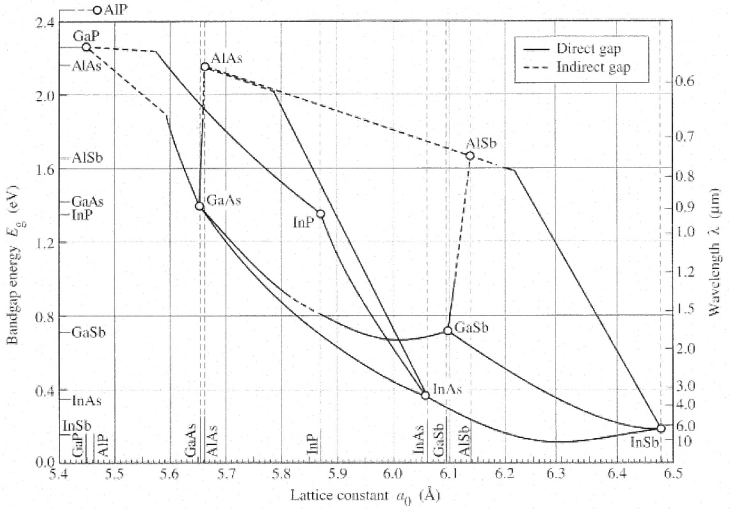

Figure 1-1 Band gap energy and lattice constant of various III-V semiconductors at room temperature (adopted from Tien, 1988).

In contrast to $Al_xGa_{1-x}As$ amorphisation, a study of $In_{0.53}Ga_{0.47}As$ amorphisation [10] revealed that $In_{0.53}Ga_{0.47}As$ was easier to amorphise compared with both InAs and GaAs, thus indicating that the amorphisation properties of $In_xGa_{1-x}As$ were *not* intermediate between the two binary extremes. Investigation of this anomaly in semiconductor compounds forms the basis of this thesis.

The aim of this thesis was to investigate the ion beam induced amorphisation behaviour in three semiconductor compounds, namely, $In_xGa_{1-x}As$, $In_xGa_{1-x}P$ and $Si_{1-x}Ge_x$, as a function of stoichiometry. The resulting damage was studied using Rutherford backscattering in the channelling configuration (RBS-C). Extend X-ray Absorption fine structure (EXAFS) was used to determine the change in bond length, bond angle and structural disorder with varying composition. Results from EXAFS were then correlated

with RBS-C to explain the amorphisation behaviour observed in these semiconductor compounds.

1.2 Ion Implantation

Ion implantation is a process by which energetic ions are introduced into a solid to change its properties (physical, electrical, optical etc.). It is a vital process in many industries and research areas [11] including semiconductor device fabrication, superconductors, hardening and surface treatment of metals, and nuclear physics. Ion implantation provides an alternative and non-equilibrium method of introducing dopant atoms into the lattice or substrate material. The use of energetic ions, typically eV-MeV range, allows virtually any element, independent of thermodynamic factors, to be introduced in to a substrate material. This process provides a high degree of control over the ion fluence[1] of the implanted ions and their depth in to the substrate material (ion energy). It is due to this high degree of control over the implanted species that the ion implantation technique forms an integral part of the semiconductor device fabrication process.

1.3 Ion-Solid Interaction

Atoms of the species to be implanted are ionised and then accelerated in the direction of the target or the substrate. Lattice disorder and radiation damage effects are produced by the incident ions as they traverse through the substrate material by a series of collisions with its nuclei and electrons. As the ions collide with the target and gradually lose their energy, both from occasional collisions with target nuclei, i.e., *nuclear stopping*, which

[1] Ion fluence is the number of ions implanted per unit area of a given material.

causes abrupt energy transfers; and from a mild drag due to interactions with electrons or *electronic stopping*, which is a continuous process. The loss of ion energy in the target is called ion stopping and is dependent on the energy, mass and atomic number of the ions as well as the mass, atomic number and density of the substrate.

Both nuclear and electronic energy losses increase with increasing energy, reach a maximum and then decrease. The relative importance of the two energy-loss mechanisms changes rapidly with the energy E and atomic number Z_1 of the particle: nuclear stopping predominates for low E and high Z_1, whereas electronic stopping takes over for high E and low Z_1. Electronic energy loss reaches its maximum (Bragg peak) at energies which are orders of magnitude higher than that for nuclear energy loss (see Figure 1-2). The range of ion implantation energies used during the course of this thesis is keV to low MeV. For this range, nuclear stopping is the dominant form of energy loss mechanism. The average depth or the range of the ions depends on the energy of the incident ion, the ion species and the composition of the target material: and is typically < 5 μm. This makes ion implantation especially useful for near-surface studies, as the chemical or structural change is close to the surface of the target.

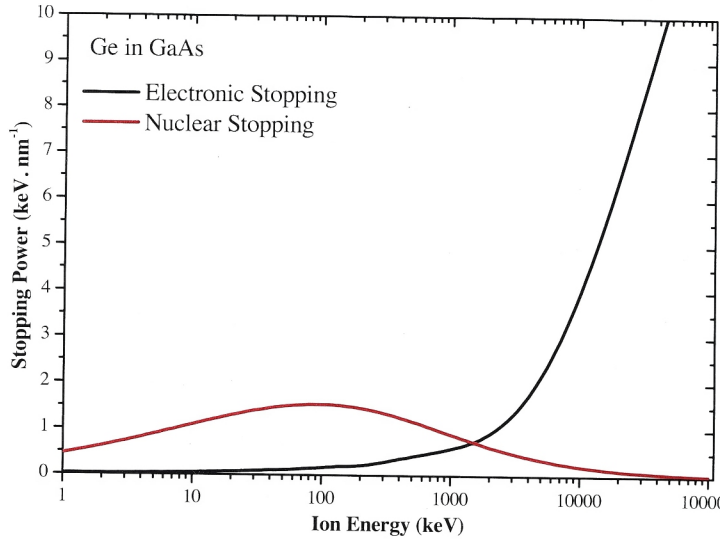

Figure 1-2 Electronic and nuclear energy loss vs. ion energy for Ge ions implanted into GaAs.

Nuclear interaction can involve large discrete energy-losses and significant angular deflection of the trajectory of the ion. This process is responsible for the production of lattice disorder by the displacement of atoms from their positions in the lattice. The displaced atoms can themselves interact with other target atoms leading to a collision cascade. Nuclear ion stopping can lead to the creation of point defects in the target crystal, such as vacancies and interstitials. These point defects can migrate and cluster, resulting in dislocation loops and other defects. Depending on the ion implantation parameters, ion stopping can also result in the formation of amorphous zones. In some cases, complete amorphisation of a target is preferable to a highly defective crystal: for example, amorphous layers can be regrown at a lower temperature than required to anneal a highly damaged crystal. For the energy range investigated in this study, the

electronic interactions involve much smaller energy-losses per interaction, negligible deflection of the ion trajectory, and negligible lattice disorder.

1.4 Mechanisms of damage formation in semiconductors

The type and extent of the resulting damage due to ion-solid interaction is influenced by various factors [12-16] including, but not limited to, target temperature, ion energy and ion fluence, in addition to the mass of the implanted ions, as mentioned earlier.

To counter the strong influence of the atomic number, ion fluence (N_I) can be normalised to the atomic density (N_0) to give the number of displacements per lattice atom, η_{dpa}, such that:

$$\eta_{dpa} = N_{displ} * \frac{N_I}{N_0} \qquad (1.1)$$

where N_{displ} is the effect from a single ion impact i.e. the number of displacements per ion per Å and is calculated using SRIM [17]. Use of the term η_{dpa} allows comparison of results from different ion species implanted into one material or of one ion species into various materials.

Intrinsic defects, such as vacancies or interstitials, may become mobile with increasing temperature allowing for defect recombination within the primary collision cascades. This results in a reduction in residual damage after implantation. This reduction in residual damage was shown by Wendler *et al.* [14], where the defect concentration in Si

implanted InP was shown to reduce with increasing implantation temperature as a result of dynamic annealing.

Increasing the incident ion energy shifts the maximum of the ion distribution in the crystal lattice to greater depths as the nuclear energy loss occurs at the end of the range of the implanted ions. In addition, this maximum value decreases due to enhanced straggling of the high energetic ions.

1.4.1 Amorphisation Models

Homogenous amorphisation is generally associated with the steady accumulation of point defects until a critical concentration is reached; after this point amorphisation can occur spontaneously being the energetically favourable route. Ion irradiation induced amorphisation is generally attributed to heterogeneous amorphisation. In this case the amorphous clusters are produced within a single ion impact, which accumulates to form an extended amorphous layer with continued irradiation. Heterogeneous amorphisation has been associated with several possible mechanisms. These include direct-impact amorphisation; overlap of collision cascades as a result of local accumulation of high defect concentrations; nucleation and growth; or a combination of these models.

Several models, mechanisms and simulations have been suggested to describe the amorphisation behaviour of materials. Jencic *et al.* [18] modelled amorphous zones in semiconductors using the randomisation-and-relaxation method, however, they found no significant difference between AlGaAs and GaAs with this model. Brown and Williams [19] used the Morehead and Crowder model [20] to describe the amorphous layer formation. Nord *et al.* [21] have discussed the Gibbons model, the amorphisation theory of Wang *et al.* [12], and the Hecking model [22] to define the amorphisation behaviour

of Si, Ge and GaAs. They found the Hecking model and the model of Wang *et al.* both give good fits to the amorphous fraction formation during ion irradiation. The Hecking model has been widely used [10, 23, 24] to describe the amorphisation behaviour of III-V semiconductors including $A_xlG_{1-x}aAs$ and $In_xGa_{1-x}As$. On this basis, the Hecking model was chosen to model the damage formation for all materials in this thesis. A good reference for amorphisation mechanisms and models is a review by Weber [25].

1.4.1.1 The Hecking Model

Hecking *et al.* [22] investigated the ion fluence and temperature dependent damage in Si from temperatures ranging from 125 K to 475 K and proposed a new model for defect interaction and amorphisation. They identified various stages of the damage accumulation process which included: a proportional increase in damage with fluence (low fluence region); an increasing recombination of defects; stabilisation of defects in clusters and progressive increase of amorphised regions; and disorder saturation resulting in continuous amorphous regions.

Hecking *et al.* defined amorphisation as occurring from point defects or from amorphous regions or both. They developed a model that takes into account recombination, clustering and saturation of point defects along with direct-impact and interface stimulated amorphisation thus allowing for modelling of various stages of damage build up depending on temperature and ion fluence. The interface-stimulated term takes into account the defect-stimulated, cascade-stimulated or implanted-ion-stimulated growth of amorphous regions. They express disorder production mathematically as two differential equations:

$$\frac{df_p}{dN_I} = P_p\left[e^{(-R^2N_I^2)}\right](1-f_a) + Cf_p\left(1-\frac{f_p}{f_p^*}\right) - \frac{df_a}{dN_I}\frac{f_p}{1-f_a} \quad (1.2)$$

$$\frac{df_a}{dN_I} = (P_a + A_s f_a)(1-f_a) \quad (1.3)$$

Here the accumulated amorphous fraction f = f_p + f_a, where f_p is the relative fractions of point defects and f_a is the relative fraction of amorphous regions. P_p and P_a are parameters for primary production of point defects and amorphous regions; A_s is the stimulated amorphisation term; R, C and s_p^* refer to recombination, clustering and saturation of point defects and N_I is the ion fluence. Hecking *et al.* Introduced the term (1-f_a) to allow for the fact that simple defects are only produced in crystalline regions. A solution to the above differential equations is given by Weber [25]:

$$f = 1 - \frac{(P_a + A_s)}{\{P_a + A_s e^{[(P_a+A_s)N_I]}\}} \quad (1.4)$$

where P_a and A_s are the probabilities for direct-impact and stimulated amorphisation, respectively.

1.5 Comparison of $Al_xGa_{1-x}As$ and $In_xGa_{1-x}As$

The observed difference in the amorphisation behaviour of $In_{0.53}Ga_{0.47}As$ [10] and $Al_xGa_{1-x}As$, [9] in comparison to their respective binary extremes, forms the basis of this thesis. This section outlines the findings of these two studies and a brief overview of the literature in relation to them.

1.5.1 $Al_xGa_{1-x}As$

Both AlAs and GaAs have a zinc-blende structure and have almost similar lattice constants, 5.6615 Å and 5.6533 Å respectively. Hence, when AlAs and GaAs are 'mixed' together, the resulting AlGaAs is expected to be like an alloy of AlAs and GaAs and follow the Virtual Crystal Approximation (VCA) model. This model suggests that in a ternary compound like $A_xB_{1-x}C$, the atoms are located at the 'ideal' lattice sites of the average unit cell, without any distortions.

The amorphisation of $Al_xGa_{1-x}As$ has been extensively studied [9, 23, 26-34]. The higher the Al content, the more difficult it is to amorphise the ternary alloy. Tan *et al.* [9] also showed that in $Al_xGa_{1-x}As$, the threshold ion fluence for amorphisation increases with increasing Al content (see Figure 1-4). The amorphisation threshold of the two binary extremes (GaAs and AlAs) differs by two orders of magnitude (see Figure 1-3).

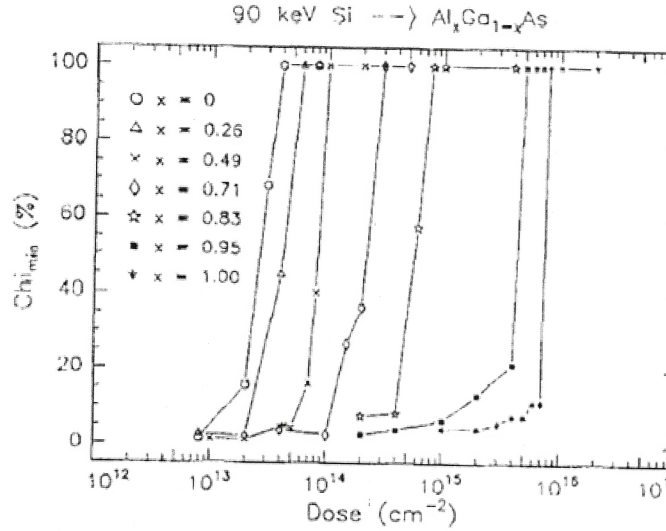

Figure 1-3 Amorphisation of $Al_xGa_{1-x}As$ from Tan *et al.* [9]. Irradiations were performed at liquid-nitrogen temperature. Chi_{min} of 0% and 100% correspond to unimplanted and amorphous material, respectively.

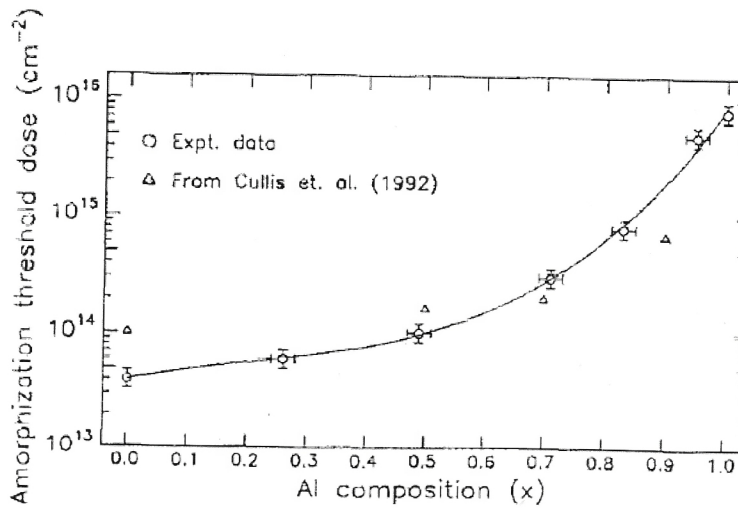

Figure 1-4 Amorphisation threshold for $Al_xGa_{1-x}As$ taken from Tan *et al.* [9].

Tan *et al.* suggested that for lower Al content, amorphisation occurs via overlap of damage cascades and amorphous zones created by incident ions. Whereas for higher Al content, disorder builds up in the form of stacking faults and other extended defects until a critical defect density is reached, after which the material collapses into an amorphous phase with any further increase in ion fluence [35].

Lagow *et al.* [31] reported similar observations for $Al_xGa_{1-x}As$ with respect to higher ion fluence required for amorphisation with increasing Al content. However, they questioned the need for formation of planar defects or extended defects prior to amorphisation, as that would require dynamic annealing, and dynamic annealing is in contradiction to the experimental fact that the damage accumulation at such low temperatures is nearly independent of the flux. Hence, they suggested a model which avoids the need for formation of planar defects prior to amorphisation. They assumed that direct impact amorphisation and point defect build up processes are also responsible for damage formation in the case of $x > 0.8$. This means the amorphisation mechanism does not change for the entire range of x. Based on the composition dependence of density, heat capacity and melting temperature (which ultimately effect the thermal spike lifetime responsible for determining the vacancy distribution in the cascade volume), Lagow *et al.* conclude that the probability for creating an amorphous pocket should decrease rapidly with increasing x. This may explain the strong dependence of damage formation on the composition [28].

Data from Figure 1-3 was fit using Eq. 1.4 to obtain values of P_a and A_s, and is shown in Figure 1-5.

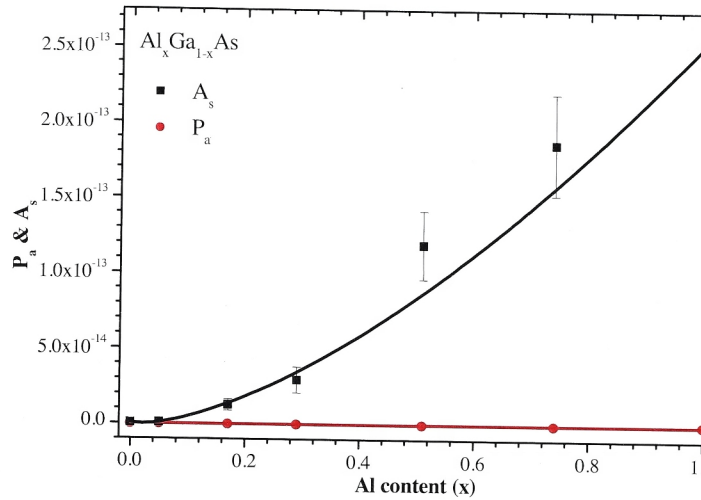

Figure 1-5 Probabilities for direct impact (P_a) and stimulated (A_s) amorphisation as a function of Al content (x) for $Al_xGa_{1-x}As$.

From Figure 1-5 it is evident that stimulated amorphisation process (A_s) is dominant relative to direct impact amorphisation (P_a) over the entire range of x. In addition, A_s shows a trend similar to the amorphisation threshold reported for $Al_xGa_{1-x}As$ by Tan *et al.* [9], as was shown in Figure 1-4.

1.5.2 $In_xGa_{1-x}As$

Compared with $Al_xGa_{1-x}As$, the two binary extremes in $In_xGa_{1-x}As$ differ considerably in terms of their lattice constant, with GaAs having a lattice constant of 5.6533 Å and InAs 6.0583 Å. However, they both have the same zinc-blende crystal structure.

Although, amorphous-layer formation in $In_xGa_{1-x}As$ by ion implantation has been previously investigated by several authors [36-38], its rapid amorphisation behaviour [10] was not apparent in the absence of a comparison with both InAs and GaAs. Akano

et al. [36] compared disorder and dynamic annealing processes in $In_{0.53}Ga_{0.47}As$ and InP as a function of implantation temperature and flux. They reported that $In_{0.53}Ga_{0.47}As$ was more difficult to amorphise than InP. Yu and Hsu [37, 38] studied amorphous-layer formation in $In_xGa_{1-x}As$ for x = 0 – 0.5 and suggested that a homogeneous amorphisation process was operative at room temperature in the presence of significant dynamic annealing. In contrast, a heterogeneous process dominated at liquid-nitrogen implant temperatures, where dynamic annealing was much reduced.

Wesch and Ridgway [10] studied the amorphisation behaviour of $In_{0.53}Ga_{0.47}As$ at room temperature and at 15 K. They found that the critical nuclear energy deposition required to amorphise $In_{0.53}Ga_{0.47}As$ was less than that required for both InAs or GaAs (see Figure 1-6). This is in contrast to the amorphisation behaviour of $Al_xGa_{1-x}As$, where the critical nuclear energy deposition required to amorphise $Al_xGa_{1-x}As$ is between the two binary extremes, AlAs and GaAs, as reported in the section 1.5.1. They used the Hecking model [22] of defect interaction and amorphisation to model the amorphisation behaviour of $In_{0.53}Ga_{0.47}As$, InAs and GaAs. They concluded that rapid amorphisation of $In_{0.53}Ga_{0.47}As$ resulted from a greater probability of stimulated amorphisation. A detailed description of $In_xGa_{1-x}As$ amorphisation along with P_a and A_s curves will be discussed in Chapter 3.

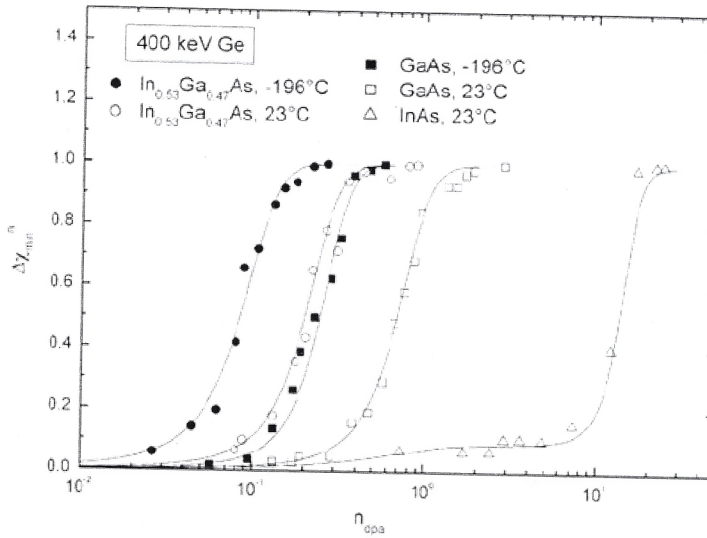

Figure 1-6 Amorphisation of $In_{0.53}Ga_{0.47}As$, InAs and GaAs as a function of nuclear energy deposition (η_{dpa}) from Wesch & Ridgway [10]. $\Delta\chi_{min}$ value of 0 and 1 represent crystalline and amorphous materials, respectively.

Wesch and Ridgway suggested that the rapid amorphisation of $In_{0.53}Ga_{0.47}As$ was a result of a greater probability of stimulated amorphisation, and that the amorphous nuclei, produced as a result of ion irradiation, serve as a means of relieving the strain present (at the atomic scale) due to the significant difference in In-As and Ga-As bond lengths, as reported both theoretically [39] and experimentally [40].

Empirically, the structure of $In_xGa_{1-x}As$ has been investigated in detail by Mikkelsen and Boyce [40] using EXAFS. They found that although the cation – cation distance is close to the VCA, there is a significant deviation from the VCA in the near-neighbour cation – anion distances (see Figure 1-7). The In-As and Ga-As bond lengths in $In_xGa_{1-x}As$ remain closer to the binary InAs and GaAs bond lengths, as opposed to following the

VCA. Also, the cation – anion distance was found to be bimodal, with the As-Ga-As and In-As-In distances staying close to those in pure GaAs and InAs.

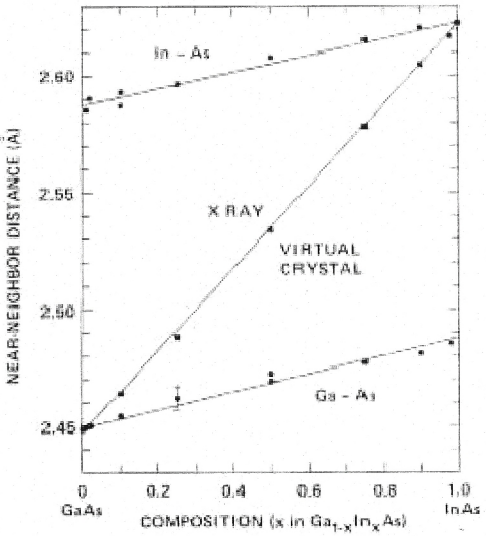

Figure 1-7 In-As and Ga-As bond length as a function of alloy composition determined using EXAFS from [40].

The data shown in Figure 1-7 were modelled theoretically by Cai and Thorpe [39]. Their model described a topological rigidity parameter (a**) as a measure of the rigidity of the lattice. a** was calculated as 0.8 for $In_xGa_{1-x}As$. Here, when a** = 1, only bond bending is active and at the other extreme, when a** = 0, only bond stretching is active. This parameter, as it applies to $In_xGa_{1-x}As$, $In_xGa_{1-x}P$ and $Si_{1-x}Ge_x$ will be discussed in more detail in Chapters 3, 4 and 5.

$In_xGa_{1-x}P$ is very similar to $In_xGa_{1-x}As$ in terms of the difference in lattice constant between InP (5.869 Å) and GaP (5.451 Å). It has shown to have a similar bimodal cation – anion bond length as observed in $In_xGa_{1-x}As$ [41]. $Si_{1-x}Ge_x$ has also been shown to

have a composition dependent bond length [42] similar to both $In_xGa_{1-x}As$ and $In_xGa_{1-x}P$. To examine if the amorphisation behaviour observed in $In_xGa_{1-x}P$ and $Si_{1-x}Ge_x$ is also similar to that of $In_xGa_{1-x}As$, this thesis investigates the amorphisation kinetics of $In_xGa_{1-x}P$ in Chapter 4 and $Si_{1-x}Ge_x$ in Chapter 5.

1.6 Thesis Structure

This thesis consists of six chapters as follows:

Chapter 1: has given a brief introduction to the topic and the contents of this thesis along with a general literature review and background to the research work presented in this thesis.

Chapter 2: discusses the most significant experimental techniques utilised and sample preparation techniques.

Chapter 3, 4 and 5 present the studies carried out on $In_xGa_{1-x}As$, $In_xGa_{1-x}P$ and $Si_{1-x}Ge_x$, respectively, along with a review of literature pertinent to each material.

Chapter 6: presents a conclusion and suggestions for future work.

Chapter 2 Experimental Techniques

2.1 Ion Implantation

An introduction to ion implantation technique was given in section 1.2. This section describes the instrumentation for ion implantation.

2.1.1 NEC Tandem (5SDH) High-Energy Ion Implanter

An ion implanter typically consists of a source, where ions of the desired element are produced; an accelerator, where the ions are electrostatically accelerated to a high energy; and a target chamber, where the ions impinge on a target. The actual amount of material (ions) implanted is the ion fluence.

The Electronic Materials Engineering Department (EME) at ANU houses a 1.7 MV NEC Tandem high-energy ion implanter. A schematic diagram of this machine is shown in Figure 2-1.

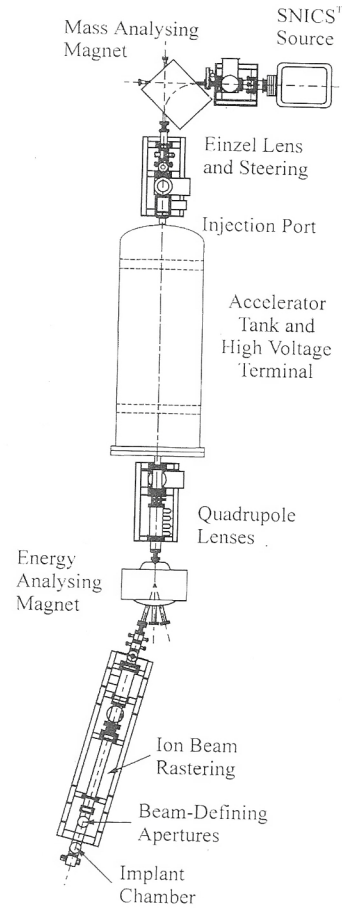

Figure 2-1 Schematic of the National Electrostatics Corporation 5SDH-4 1.7 MV high energy ion implanter.

The ion implantation facility at the ANU is a high-current, high-energy tandem accelerator which uses a "Source of negative ions by Caesium sputtering" (SNICS II) to produce negative ions. Cs vapour is ionised by the hot ioniser, producing Cs^+ ions. These ions are accelerated towards the cathode maintained at a potential of – (5 – 10) kV, sputtering particles from it through the condensed Cs layer on the surface of the cathode. Most sputtered particles are neutral, however, some sputter as negative ions and

others as positive. Negative ions are accelerated away from the cathode through an extractor having a potential of around 10 – 15 kV. This process is outlined in Figure 2-2 below.

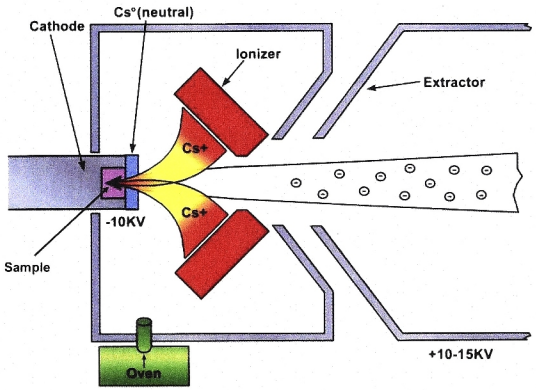

Figure 2-2 Schematic of Source of Negative Ions by Cs Sputtering (SNICS II).

An additional acceleration with a bias potential of 45 – 60 kV and an Einzel lens are used to increase the energy and focus the beam, respectively. The negative ions then pass through the 90° electromagnet to select the desired ion mass and eliminate any impurities. The relationship between the magnetic field (B), the mass (m) and the charge (q) of the ions is given by the following equation:

$$B = \frac{\sqrt{2}}{r}\sqrt{\frac{mV}{q}} \qquad (2.1)$$

where r is the bending radius of the magnet and V is the source potential.

Using an Einzel lens, the beam is then focused into the high energy tandem accelerator. This has ground potential at both ends and a positively charged high voltage terminal in the middle. The terminal can reach a maximum potential of 1.7 MV. Positive charge is supplied to this terminal by four nylon chains interconnected with steel pellets. N_2 is used as a stripper gas which converts the incoming negative ions into positive ions. These positively charged particles are repelled by the high voltage terminal, thus further accelerating them with the final energy of the ion at the high energy end of the accelerator as:

$$E_f = q[V_i(1+n)V_t] \tag{2.2}$$

where V_i is the total potential out of the ion source and V_t is the terminal potential.

The ions exiting the accelerator have a range of energies depending on their charge state. A second electromagnet is used for energy analysis to select the desired charged state of the ions. The ion beam is then raster scanned in the x and y-planes to produce a uniform distribution of the beam on the target.

The samples are mounted on a variable temperature sample holder made of Ni. A Cu cage surrounds the target. This is maintained at -300 V to suppress any secondary electrons and at liquid N_2 temperature to avoid surface contamination from hydrocarbons during the irradiation process. The implanted area A is defined by a Ta aperture placed before the sample holder. Current I can be measured on the target to provide a measure of the implanted ion fluence Φ, using Eq. 2.3.

$$\Phi = \frac{1}{nqA}\int_0^t I\,dt \tag{2.3}$$

A detailed discussion of the ion implantation process is out of the scope of this thesis and readers are directed to references [43] and [44].

2.2 Rutherford Backscattering Spectrometry – Channelling

RBS is an ion beam technique widely used for quantitative analysis of composition and structural disorder in semiconducting materials.

High energy alpha particles (2 MeV He^+ used in this study) are directed onto the sample and the energy of the backscattered projectiles is recorded with an energy sensitive detector (solid state detector). The incident ions, having mass M_1 and initial energy E_o, are elastically scattered from the atoms in the sample. The interaction between the atomic nuclei can be modelled using the 'hard sphere model' of elastic collisions, which uses simple laws of conservation of energy and momentum. The resulting energy E_1, of the backscattered ions is given by $E_1 = KE_0$, where K is the kinematic factor given by:

$$K = \frac{E_1}{E_0} = \left\{ \frac{[1 - (M_1 \sin\theta)^2] + \frac{M_1 \cos\theta}{M_2}}{1 + \frac{M_1}{M_2}} \right\} \qquad (2.4)$$

where θ is the scattering angle and M_2 is the mass of the target nucleus initially at rest. By measuring the energy of the scattered ions, at a fixed angle, we can determine the composition of the sample as a function of depth. E_1 will also vary depending on whether the particles backscatter from the surface of the sample (higher E_1) or from some depth within the sample (lower E_1). This difference in energy, as a result of the

distance travelled by incident ion within the sample, helps determine the sample layer thickness (depth profiling).

The probability that a backscattered particle will scatter into the detector at a given angle is called the scattering cross section, and is given by:

$$\frac{d\sigma}{d\Omega} = \left(\frac{Z_1 Z_2 e^2}{4E}\right)^2 \frac{4}{\sin^4\theta} \frac{\left[\sqrt{\frac{1-(M_1\sin\theta)}{M_2}} + \cos\theta\right]^2}{\sqrt{1-\left(\frac{M_1\sin\theta}{M_2}\right)}} \qquad (2.5)$$

where Z_1 and Z_2 are the atomic numbers of incident and target particles, respectively; M_1 and M_2 are the masses of incident and target particles, respectively; and E is energy of incident particle. A schematic for this is shown in Figure 2-3.

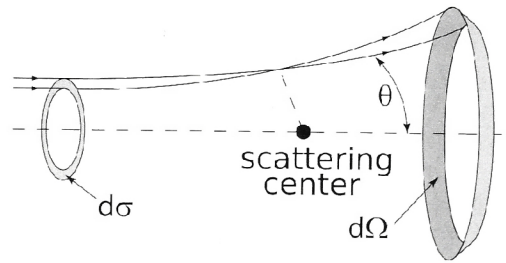

Figure 2-3 Schematic depicting the scattering cross section [45].

Here, dσ represents a finite region for an incoming particle, whereas dΩ represents the solid scattering angle after the scattering event. The scattering cross section is directly proportional to the square of the atomic number of the target atom and thus we expect a

larger scattering cross section for heavier atoms. This implies that RBS is more sensitive for heavier elements (greater yield) than for lighter elements.

If a crystalline sample is aligned such that the rows of atoms in the lattice are parallel to the incident He^+ beam direction then the number of backscattered particles is greatly reduced. This is known as *channelling* because the particles are steered by the rows of atoms and penetrate much deeper into the sample (crystal) with a reduced probability of coming into contact with a scatterer (Figure 2-4). Any crystalline imperfections in the sample will lead to an increase in backscattered ion yield. This occurs because any defects within the crystal provide a source of scattering for the channelled particles into non-channelling paths. This scattering process is known as *dechannelling*. Each defect has a specific effect on the channelled particle and can be associated with a corresponding dechannelling factor. Hence, channelling can be used as a measure of the depth profile and the type of defects present in the material. The difference in yield of backscattered particles between an aligned and a non-aligned sample is an indication of the crystallinity of the material.

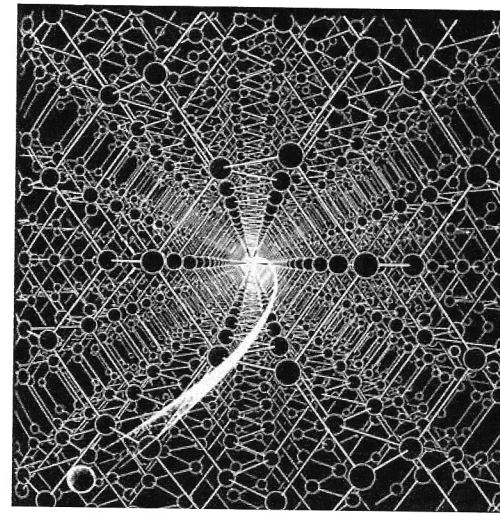

Figure 2-4 Artist's conception of the channelling process on a microscopic scale adapted from [46, 47].

Some dechannelling, however, does occur in perfect crystals. As a result of multiple scattering from the target nuclei and electrons, the transverse energy of the channelled particles steadily increases as it channels into the target. Eventually some particles acquire enough transverse energy to overcome the potential barrier of the channel and escape into the crystal as part of the random beam component, i.e. are dechannelled. The dechannelled fraction is a monotonically increasing function of penetration depth because, particles once dechannelled, remain so. It is important to note that the experimentally measured yield (see Figure 2-5) is the sum of the yield from channelled particles scattered directly from displaced atoms and that from dechannelled particles scattered from all atoms in the target.

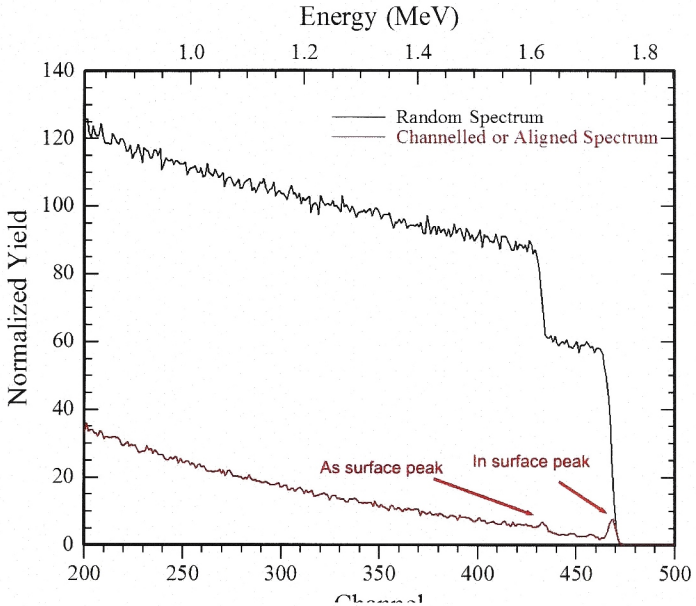

Figure 2-5 RBS measurements on crystalline InAs showing both random and channelled spectra. The surface peaks from both In and As atoms are also shown.

Even when a sample is aligned in the channelling direction, the He^+ particles will backscatter from the first few mono layers of the material at the same rate as a non-aligned material leading to surface peaks in backscattering spectra (Figure 2-5). The RBS-C measurement shown here was performed on crystalline InAs and the surface peaks can be seen, as indicated, resulting from the In and As atoms. Given the scattering cross section (hence the yield) is directly proportional to the square of the atomic number of the target atom as per Eq. 2.5, we expect the ratio of yield seen in Figure 2-5 to follow the same rule. The ratio of the atomic number for In and As is $\approx$ 2.21. The yield for In is $\approx$ 58 and that for As is $\approx$ 26 with the ratio between them being $\approx$ 2.23.

Figure 2-6 shows the channelled data for $In_{0.53}Ga_{0.47}As$ irradiated at 300 K using 60 keV ^{74}Ge ions. The conversion from backscattered ion energy to depth was performed using the DICADA program [48].

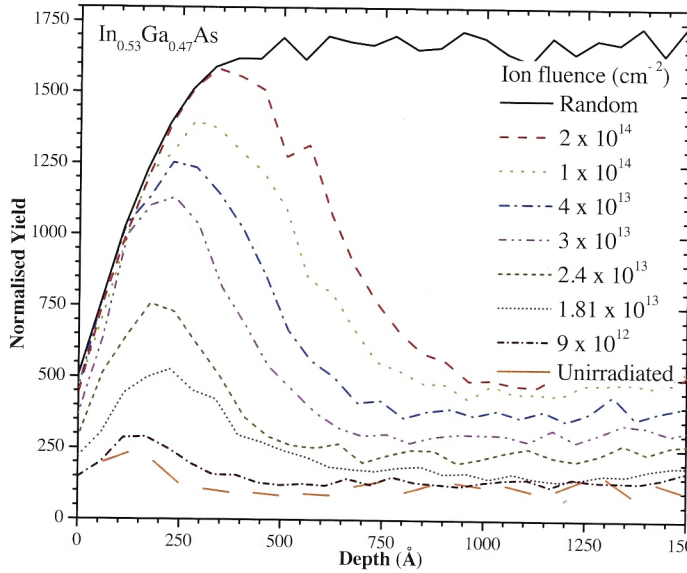

Figure 2-6 RBS-C spectra of $In_{0.53}Ga_{0.47}As$ irradiated at 300 K.

The amount of disorder increases with increasing ion fluence. Observation of this increased damage is a result of direct backscattering of the incident ions and is indicative of the formation of point defects, clusters and possibly small pockets of amorphous zones created by individual ion tracks. As the ion fluence increases, the density of these defects increases, thus resulting in a higher backscattered yield, until it reaches the random level. In this case, an ion fluence of 2 x 10^{14} cm^{-2} was sufficient to amorphise $In_{0.53}Ga_{0.47}As$. Any further increase in ion fluence would only result in an increase in the amorphous layer thickness.

Channelling can be performed along several directions including <100>, <110> and <111>. The degree of channelling will vary from one channelling direction to another based on the distance between atoms in a row. However, the <100> direction was chosen for this study for convenience as it is perpendicular to the surface and makes sample alignment easier. References [47, 49] contain detailed discussions of the channelling process.

The Department of Electronic Materials Engineering has a 3SDH pelletron accelerator. A schematic of this machine is shown in Figure 2-7. It operates in a similar way to the ion implanter described in Section 2.1.1. A radio-frequency (RF) source is used to ionise He gas to He^+ ions. Rb vapour is used to reduce He^+ to He^- ions. These ions are then accelerated through the high voltage terminal. An electromagnet is used to select the desired ion charge state (He^+ in this case) before impinging on the target. The samples are mounted on a 4-axis goniometer (with two rotational and two translational axes) for RBS-C measurements. The angular orientation can be stepped in 0.1° increments sufficient to align the sample with a channelling direction. Backscattered ions are collected by two Si Au-surface barrier detectors; one fixed at a scattering angle of 168° while the other is moveable in the scattering angle range of 90 – 120°.

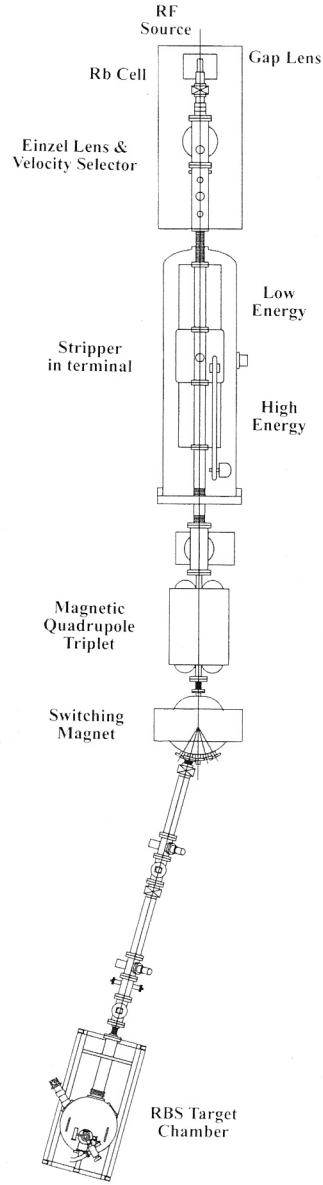

Figure 2-7 Schematic of the National Electrostatics Corporation 3SDH pelletron accelerator

In this thesis, RBS was used to determine the stoichiometry of the as-grown epitaxial layers and to quantify the implantation induced disorder via channelling. Figure 2-8 shows a RUMP simulation to determine the stoichiometry of the as grown $Si_{0.50}Ge_{0.50}$. The Si fraction was found to be 0.54 ± 0.02 and the Ge fraction 0.46 ± 0.02. Similar analysis was applied to all materials to determine the actual stoichiometry as opposed to the nominal one.

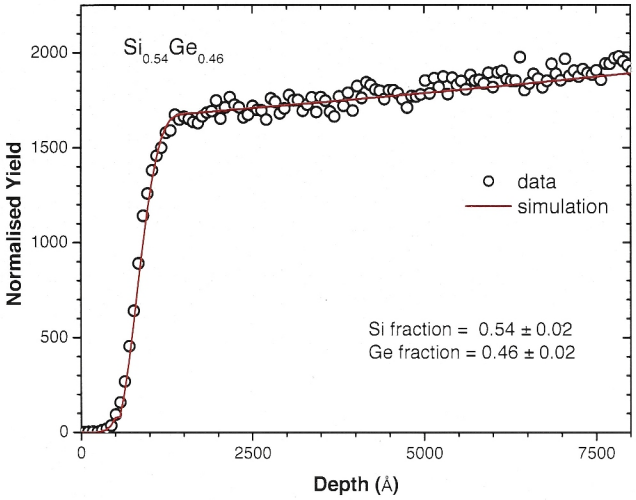

Figure 2-8 RUMP simulation for $Si_{1-x}Ge_x$ RBS data.

From the RBS-C spectra, the quantity $\Delta\chi_{min}$ was calculated using:

$$\Delta\chi_{min} = \frac{Y_{implanted} - Y_{unimplanted}}{Y_{random} - Y_{unimplanted}} \qquad (2.6)$$

where $Y_{implanted}$ and $Y_{unimplanted}$ are the integrated backscattered ion yields over a particular region of interest in the channelling direction for the implanted and

unimplanted sample, respectively, and Y_{random} is the random yield. $\Delta\chi_{min}$ is an approximate measure of lattice disorder. A $\Delta\chi_{min}$ value of zero corresponds to unimplanted material, while a value of one represents no epitaxial alignment, consistent with amorphous material. These $\Delta\chi_{min}$ values were then fit using the Hecking model to yield the probabilities for direct impact (A_s) and stimulated amorphisations (P_a).

2.3 Extended X-ray Absorption Fine Structure

EXAFS is a powerful analysis technique used to study the local atomic structure including bond length, coordination number, type of neighbour and structural disorder [50]. This phenomenon was first reported by Fricke [51] and early theoretical work was carried out by Kronig [52]. The development of synchrotron radiation revolutionised the EXAFS technique, enabling experiments to be performed in a much superior manner due to the tunability and intensity of a synchrotron source. Since the 1970s when we saw the development of modern EXAFS theory, this technique has received considerable attention and has been used as a quantitative structural tool across a variety of scientific disciplines. An excellent reference [53] deals with the theory of EXAFS [54], data analysis [55], and applications in fields such as biochemistry [56], catalysis [57], and amorphous and liquid systems [35].

Figure 2-9 shows a typical layout of a synchrotron radiation facility. Electrons are first produced via the electron gun and accelerated to relativistic velocities using a linear accelerator and then transferred to the booster ring where the electrons increase in energy to a few GeV. They are then transferred to the outer storage ring. The straight sections of the storage ring contain insertion devices (IDs) such as wigglers and

undulators. It is the deflection of the electrons through the magnetic field of the bending magnet and IDs which produces the synchrotron radiation.

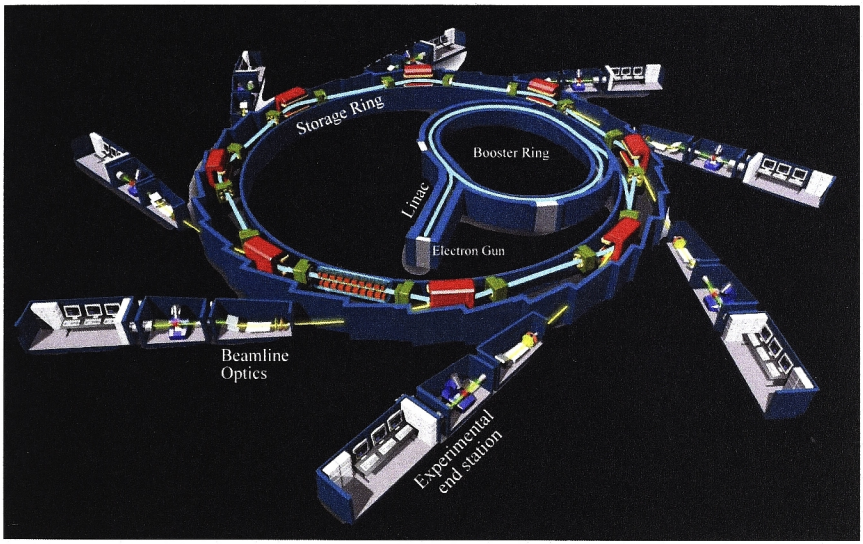

Figure 2-9 Typical layout of a synchrotron facility. Adapted from [58].

IDs are used to significantly increase the beam intensity by the use of alternating magnetic fields that force the electrons to oscillate either strongly in the case of a wiggler or gently as in an undulator. An illustration of how the electron beam is deflected by a bending magnet, wiggler and an undulator is shown in Figure 2-10.

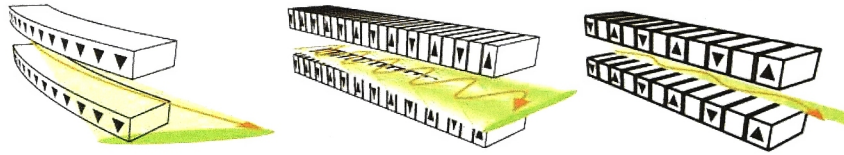

(a) Bending Magnet (b) Wiggler (c) Undulator

Figure 2-10 Illustration of (a) a bending magnet, (b) wiggler and (c) an undulator used to deflect the electron beam under the influence of a magnetic field hence producing synchrotron radiation (from [59]).

The main difference between radiation produced by a wiggler and undulator is that the wiggler has a broad spectrum of incoherent radiation with a continuous energy spectrum. An undulator, on the other hand, produces a coherent beam which has very intense radiation concentrated in narrow energy bands of the radiation spectrum. The characteristics of the resulting beam dictate which ID would be best suited for a particular experiment.

2.3.1 Theory of EXAFS

According to the Beer-Lambert Law, the transmitted intensity (I_t) through a sample is related to the sample thickness t via an exponential attenuation law such that:

$$I_t = I_0 e^{-\mu(E)t} \tag{2.7}$$

where I_0 is the incident intensity and μ(E) is the energy dependent x-ray absorption coefficient [60] varying with atomic number Z such that:

$$\mu(E) \approx \frac{\rho Z^4}{AE^3} \tag{2.8}$$

where ρ is the target density and A is the atomic mass. In the fluorescence mode $\mu(E) \propto {}^{I_f}/_{I_0}$, where I_f is the fluorescence intensity associated with the absorption process. In general, μ(E) decreases with increasing photon energy except when the photon energy equals that of a core level electron (or absorption edge) where there is a sharp increase in μ(E). It is the modulation of the x-ray absorption coefficient (μ) at energies just above an x-ray absorption edge that forms the basis of EXAFS.

2.3.1.1 X-ray Absorption

X-rays are absorbed by all matter through the photo-electric effect, resulting in the promotion of a core level electron (K, L or M shell) into the continuum leaving the atom in an excited state with an empty electronic level (a core hole). The electron ejected from the atom is called the photo-electron. This process is shown schematically in Figure 2-11.

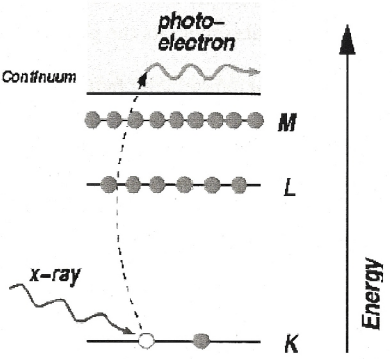

Figure 2-11 The photoelectric effect. An x-ray is absorbed and a core level electron is ejected from the atom and into the continuum.

The resulting photo-electron (treated quantum mechanically as a spherical wave) is scattered by the neighbouring atoms; the outgoing and the scattered waves can interfere constructively and/or destructively leading to an interference pattern. This phenomenon of outgoing waves interacting with neighbouring atoms is shown in Figure 2-12.

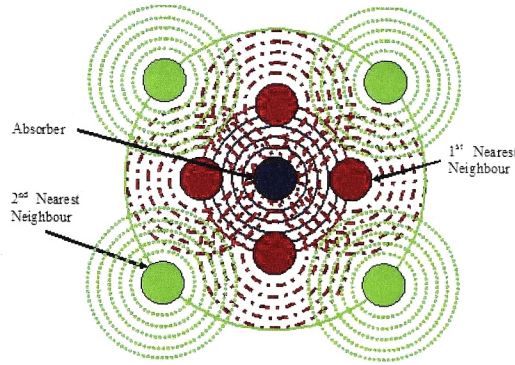

Figure 2-12 Interference between outgoing photo-electron wave and the backscatter from the neighbouring atoms.

This interference is dependent on the photo-electron wavelength and the geometry of the surrounding atoms in relation to the absorber. As the photo-electron energy changes, the wavelength λ changes and hence the phase shift between the outgoing and scattering wave is changed. The constructive and destructive interference give rise to an energy dependent fine structure in the absorbance, as shown in Figure 2-13. The modulations seen in the above edge (EXAFS) region are especially sensitive to co-ordination number, distances, structural and vibrational disorder, and the species of atoms surrounding the absorbing atom.

Figure 2-13 shows the X-ray absorption fine structure (XAFS) at the Ga K edge from a crystalline GaAs sample. When the incident x-ray has an energy equal to that of the

binding energy of a core-level electron, there is a sharp rise in absorption resulting in an absorption edge corresponding to the promotion of this core-level to the continuum. EXAFS is the modulation in x-ray absorption coefficient above the edge.

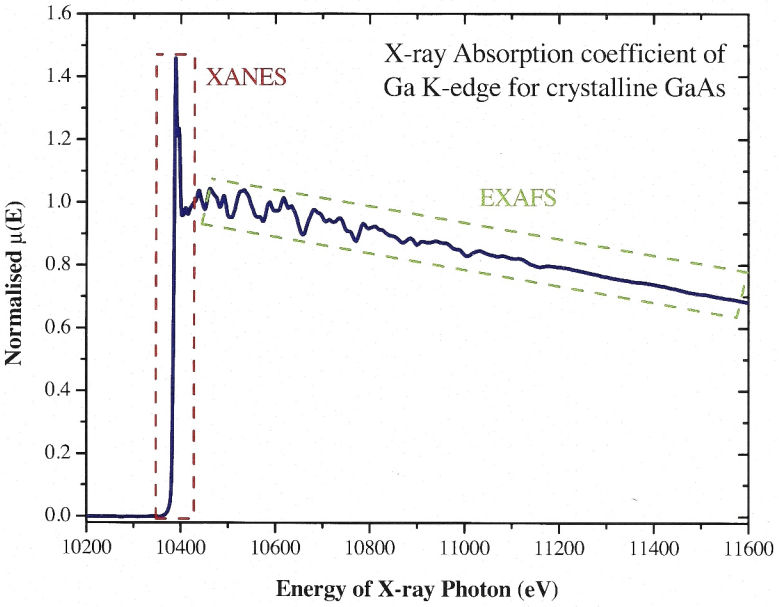

Figure 2-13 Ga K edge XAFS for crystalline GaAs.

The region immediately above the absorption edge (30 – 50 eV) is known as the X-ray absorption near edge structure (XANES), and the region further past the edge (to ~ 1000 eV) is the extended XAFS or EXAFS.

XANES is a result of the core electron being excited to an unoccupied bound orbital. Consequently XANES is sensitive to the chemical bonding (oxidation states) of the absorbing atom. XANES also depends on the geometry of the crystal structure thus

providing a means of distinguishing between different crystal phases. Analysis of XANES typically compares the measured spectra to known standards and quantifies their ratios in the sample by using linear combination fitting.

EXAFS is independent of chemical bonding and depends on the atomic arrangement around the absorber. It contains information about the coordination number, interatomic distances and structural and thermal disorder around a particular atomic species. EXAFS is not limited to materials with long range order (as XRD is) and is well suited to materials that have only short range order. Hence, this technique is well suited to the study of amorphous or disordered materials.

Only the EXAFS region of the measured samples was investigated as part of this thesis to determine bond lengths, bond angles and structural disorder.

2.3.1.2 The EXAFS Equation

The EXAFS fine structure function $\chi(E)$ is defined as:

$$\chi(E) = \frac{\mu(E) - \mu_o(E)}{\Delta\mu_o(E)} \tag{2.9}$$

where $\mu(E)$ is the measured absorption coefficient which gives the probability that an x-ray will be absorbed, $\mu_0(E)$ the smooth background function representing the absorption of an isolated atom without any interference from waves scattered by neighbouring atoms, and $\Delta\mu_0(E)$ is the measured jump in the absorption $\mu(E)$ at the threshold energy E_0 [60].

The EXAFS function χ can also be represented in terms of a wave number k as EXAFS is best understood through the wave behaviour of the photo-electron:

$$k = \sqrt{\frac{2m(E - E_0)}{\hbar^2}} \tag{2.10}$$

Here m is the electron mass, E_0 is the edge energy and ħ is Planck's constant divided by 2π. χ(k) is a summation of the contributions from each scattering shell and is defined as:

$$\chi(k) = \sum_j S_0^2 N_j \frac{f_j(k)}{kR_j^2} e^{-\frac{2R_j}{\lambda(k)}} e^{-2\sigma_j^2 k^2} \sin\left[2kR_j + 2\delta_c(k) + \delta_j(k)\right] \tag{2.11}$$

N_j represents the number of atoms in the j^{th} shell or coordination number around the absorbing atom at interatomic distance R_j. $f_j(k) = |f_j(k)|e^{i\delta_j(k)}$ is the complex backscattering amplitude. The strength of scattering and thus the magnitude of the EXAFS depends on the number (N_j) and type of scattering atoms and scattering amplitude $|f_j(k)|$. S_0^2 is the amplitude reduction factor, which takes into account the relaxation of the remaining electrons in the absorbing atom after the creation of a core-hole [61]. σ_j^2 is the Debye-Waller factor and is the relative mean square displacement between absorbing atom and j^{th} atom from both static and thermal contributions.

$\delta_c(k)$ is the phase shift experienced by the photo-electron wave in the potential of the absorbing atom. The potential of the absorbing or scattering atom leads to a phase shift of the electron wave represented by δ_c and δ_j, respectively. The absorber potential acts twice on the electron wave, once on the way out and once after being backscattered. The

resulting term $2\delta_c(k) + \delta_j(k)$ appears in the sine function of the EXAFS equation. The sin $[2kR_j]$ term accounts for contributions to the interference pattern from both the photo-electron energy and the interatomic distance.

The term $e^{-\frac{2R_j}{\lambda(k)}}$ represents the finite lifetimes of the core-hole and the photo-electron and accounts for the increasing decay of the wave with increasing distance R_j. Both effects are similar in magnitude and are included via the energy-dependent mean free path length $\lambda(k)$, i.e. the distance travelled by the photo-electron before scattering inelastically or before the core hole is filled ($\lambda(k) \approx 8$Å).

2.3.1.3 Corrections to the EXAFS equation

An improvement to EXAFS theory was the inclusion of multiple scattering and curved wave effects by Rehr and Albers [62]. Multiple scattering occurs when the photo-electron wave scatters off two or more neighbours. The effective scattering path is determined by the geometry of the scatterers and is larger for a multiple scattering path as compared with a single scattering path of an atom in the nearest neighbour shell. The other correction to the EXAFS equation was replacing the plane wave scattering amplitude f(k) by a curved wave effective scattering amplitude $f_{eff}(k,R)$. Computer code such as FEFF [61] calculates not only effective scattering amplitudes for a given absorber environment but also other k-dependent parameters such as $\delta_c(k)$, $\delta_j(k)$ and $\lambda(k)$, thus enabling a refinement of the structural parameters by comparing theoretical and experimental data.

2.3.1.4 EXAFS Data Analysis

EXAFS experiments are a measure of the absorption coefficient as a function of energy, i.e., $\mu(E)$. However, to convert this to $\chi(k)$ and then determine the various structural

parameters requires several steps such as background subtraction, normalisation and alignment of the EXAFS data, etc. Most of these steps can be performed with the help of the computer program ATHENA [63]. Figure 2-14 outlines some of the steps involved in the extraction of the EXAFS oscillations and structural refinement using ATHENA.

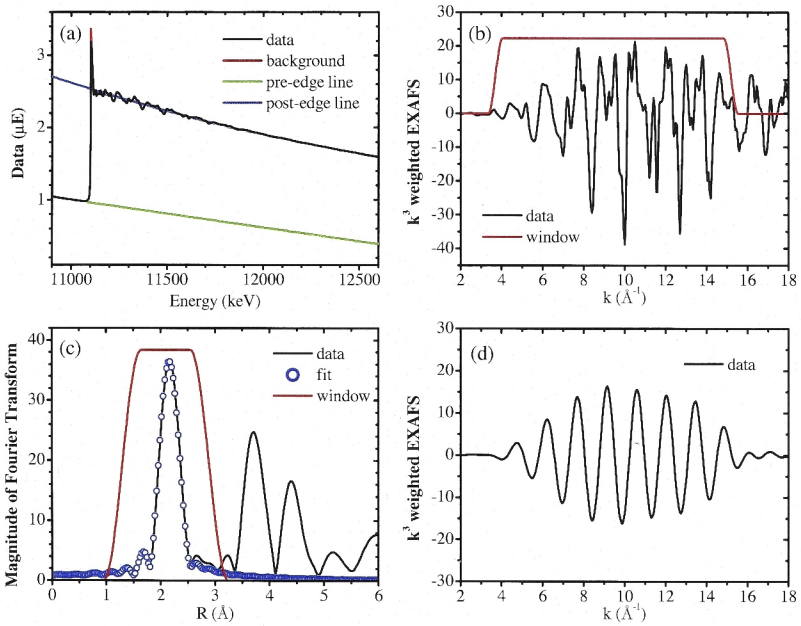

Figure 2-14 An example of the various stages of EXAFS data analysis shown using Ge K edge data: (a) Raw EXAFS data with background, pre and post-edge functions, (b) k^3 weighted $\chi(k)$, (c) conversion of $\chi(k)$ to R-space using Fourier Transform, and (d) Back Fourier Transformed data showing scattering contributions from the first nearest neighbour shell only.

Figure 2-14 (a) shows the raw EXAFS data showing $\mu(E)$ as a function of energy for crystalline Ge at the K-edge. The first step in data reduction is to subtract a smooth pre-edge function to eliminate any instrumental background and absorption from other edges. The second step is to approximate the absorption background $\mu_0(E)$ by a spline function that approaches a smooth post-edge function at high energies. This isolates the

fine structure. Data is then normalised with respect to the height of the absorption edge to remove any sample concentration and thickness effects. The position of E_0 is determined from the maximum of the first derivative of the absorption spectra $\mu(E)$. The pre-edge, post-edge and background along with the raw EXAFS data for crystalline Ge is shown in Figure 2-14 (a).

The data is then converted from $\chi(E)$ to $\chi(k)$ using Eq. 2.10 as EXAFS is best understood in terms of wave behaviour of the photo-electron created in the absorption process. $\chi(k)$ is oscillatory and decays quickly with k, hence, to emphasise the high k, $\chi(k)$ is usually shown as k^3 weighted as is shown in Figure 2-14 (b). Care must be taken when choosing to emphasise high k data as any noise in the data will also be emphasised.

To convert the $\chi(k)$ k^3 weighted data in R-space, the data is Fourier Transformed (FT) over a suitable k range using a smooth window function. The k-range used in Figure 2-14 (b) is 3.7 – 15.2 $Å^{-1}$ using a Hanning window function. The choice of k-range is governed by wanting to avoid contributions from the XANES region at the lower end and excessive noise being included from the end of the spectrum. A Hanning window (a mathematical function) is used to reduce aliasing in Fourier transforms i.e. to reduce the effect that causes different signals to become indistinguishable.

The fit to the data in R-space shown in Figure 2-14 (c), FEFF6 [61] and ARTEMIS [63] were used. Both ARTEMIS and ATHENA are part of the IFEFFIT code [64]. Although fits can also be performed in the q (back Fourier transform) and k space, R-space was chosen as it gave the best fit as determined by the lowest statistical parameters for the fit (measurement uncertainty). This and other statistical parameters for the fit are obtained

through ARTEMIS. EXAFS data is most commonly presented in the R-space as it provides a visual display of the radial distribution of atoms. Note that historically data shown in R-space is not phase corrected. This norm has been followed in this thesis as well.

A back FT can be performed to isolate scattering contributions from a particular nearest neighbour. Figure 2-14 (d) shows the back FT for Ge first nearest neighbour performed over an R range of 1.3 – 2.9 Å. The Hanning window used for the back FT is shown in Figure 2-14 (c). The resulting back FT is dominated by a single frequency as it consists of contributions from the first nearest neighbour only, which in this case is Ge.

Details of data fitting are discussed in Chapters 4, 5 and 6 as relevant to each material.

A detailed description of EXAFS data reduction and modelling can be found in several references [55, 60, 65].

2.3.2 Experimental Setup

Two possible means of measuring the absorption coefficient exist: transmission mode and fluorescence mode. Figure 2-15 shows the experimental setup for both modes in the context of BL-20B, the Australian National Beamline Facility (ANBF) at the Photon Factory in Tsukuba, Japan.

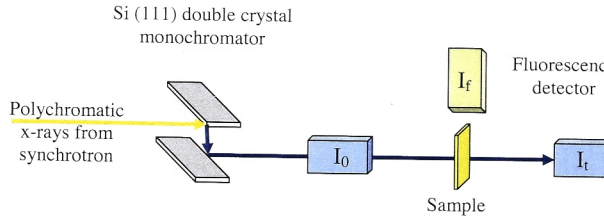

Figure 2-15 Experimental setup of the XAFS experiment at the ANBF on BL-20B depicting both transmission and fluorescence measurements.

In transmission mode both the incoming (I_0) and the transmitted (I_t) beam intensities are measured using gas filled ion chambers placed before and after the sample, respectively. The sample is situated in a cryostat maintained at 10-15 K to minimise thermal vibrations. This is important so that we only measure structural disorder as at elevated temperatures both structural and thermal disorders are present. The absorption coefficient can then be determined using Eq. 2.7. Transmission measurements are well suited to concentrated samples and usually require highly homogeneous samples free of pinholes and having a constant thickness.

In contrast, using the fluorescence mode, highly dilute, non-homogeneous samples can be measured. Samples are rotated ~ 45° to the incident beam towards the fluorescence detector to minimise elastic scattering and maximise the signal from the sample into the detector. This detection mode relies on the characteristic x-rays that are emitted when the core-hole is filled with an electron from a higher energy level. Detection of the fluorescence signal is however more complicated compared with the transmission mode. The fluorescence signal must be isolated from other x-rays, especially the elastically scattered beam.

2.3.2.1 Australian National Beamline Facility (BL-20B)

The EXAFS experiments in this thesis were performed in the transmission mode at beamline 20-B, the hard x-ray Australian National Beamline Facility (ANBF) at the Photon Factory (PF) in Tsukuba, Japan. Access to this beamline was through the Australian Synchrotron Research Program (ASRP). The PF is a second generation synchrotron radiation facility (i.e. a dedicated source of synchrotron radiation) with 21 beamlines that are used by scientists for various experimental techniques.

The synchrotron source provides a range of x-ray wavelengths using a bending magnet; a particular energy is selected by using a monochromator. The monochromator consists of two parallel Si (111) crystals oriented at an angle θ satisfying the Bragg condition for a particular energy. The resolution of the monochromator is approximately 1eV at 10 keV. The energy range at the ANBF is 4 - 25 keV. A schematic of the typical experimental setup at BL20-B was shown in Figure 2-15.

2.4 Summary

This chapter outlined the main equipment and experimental techniques utilised for the data presented in this thesis. An ion implanter was used to implant Ge ions in the samples studied in this thesis. RBS was used to determine the composition of the epitaxially grown layers for all samples and RBS-C was used to quantify the as-grown and the ion implanted disorder in these materials. EXAFS measurements were carried out in the transmission mode to determine the structural parameters such as bond length, bond angle and structural disorder in the crystalline materials.

Chapter 3 $In_xGa_{1-x}As$

3.1 Introduction

The use of $In_xGa_{1-x}As$ in electronic and photonic device fabrication [1, 3, 4, 66-68] has generated considerable interest in this ternary alloy, whose material properties can be precisely tailored by varying the stoichiometry x. The resulting properties are generally intermediate between the two binary extremes [7, 8] including, for example, a band gap that progressively decreases as x increases. In contrast, it has been shown that $In_{0.53}Ga_{0.47}As$ [10] is rendered amorphous by ion implantation at fluences lower than those required for both InAs and GaAs. A literature review for $In_xGa_{1-x}As$ was given in Chapter 1, section 1.5.2.

Transmission Electron Microscopy (TEM) was utilised to observe the presence (or absence) of misfit dislocations in the as-grown material. Using Rutherford backscattering spectroscopy in the channelling configuration (RBS-C), the effect of misfit dislocations on the amorphisation process was studied. RBS-C was then utilised to deduce the stoichiometry most easily amorphised and identify the mechanism governing the amorphisation process. Using extended x-ray absorption fine structure (EXAFS) spectroscopy, bond-length and bond-angle distributions for $In_xGa_{1-x}As$ as well as InAs, GaAs and $Al_{0.50}Ga_{0.50}As$ were determined and structural distortion in these materials was compared.

3.2 Experimental

Epitaxial $In_xGa_{1-x}As$ layers, with x = 0.06, 0.28, 0.37, 0.53, 0.75 and 0.90, were grown by metal organic chemical vapour deposition (MOCVD) on (100) substrates. All epitaxial layers were grown using the AIXTRON AIX 200/4 MOCVD facility at the Department of Electronic Materials Engineering. Stoichiometries of x = 0.06, 0.28 and 0.37 were grown on GaAs, x = 0.53 and 0.75 were grown on InP while x = 0.90 was grown on InAs. The substrate material was chosen to minimise lattice mismatch between the substrate and epitaxial layer and hence reduce the misfit dislocation density. The thickness of the epitaxial layers was 0.10 ± 0.01 μm with the exception of lattice-matched $In_{0.53}Ga_{0.47}As$ where the layer was 0.6 μm thick. The lattice matched $In_{0.53}Ga_{0.47}As$ was grown at 650 °C with a V/III flow rate of 57. All other layers were grown under similar conditions. Nominally undoped InAs, GaAs and $In_xGa_{1-x}As$ samples were implanted simultaneously with 60 keV ^{74}Ge ions at 300 K. Thicker layers (1 – 2 μm) were grown for samples used for EXAFS measurements.

Figure 3-1 shows a SRIM simulation of the vacancy profile from 60 keV ^{74}Ge implanted in $In_{0.53}Ga_{0.47}As$ using full cascade mode and a displacement energy of 25 eV. The figure shows that most of the damage is concentrated within ~ 0.1 μm from the surface of the material.

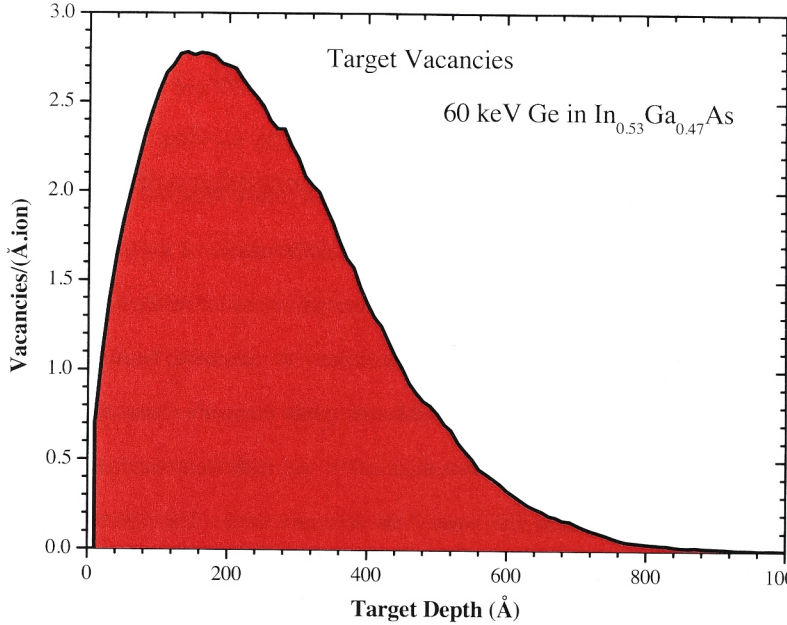

Figure 3-1 Vacancy profile of 60 keV ^{74}Ge in $In_{0.53}Ga_{0.47}As$.

Having previously determined the ion fluence required to amorphise $In_{0.53}Ga_{0.47}As$ layers (see Figure 2-6) the corresponding athermal vacancy production was determined as ~2.78 vacancies/Å.ion using SRIM simulations. Additional calculations were then performed to determine the energies required to create a uniform damage layer in the thicker samples as shown in Figure 3-2.

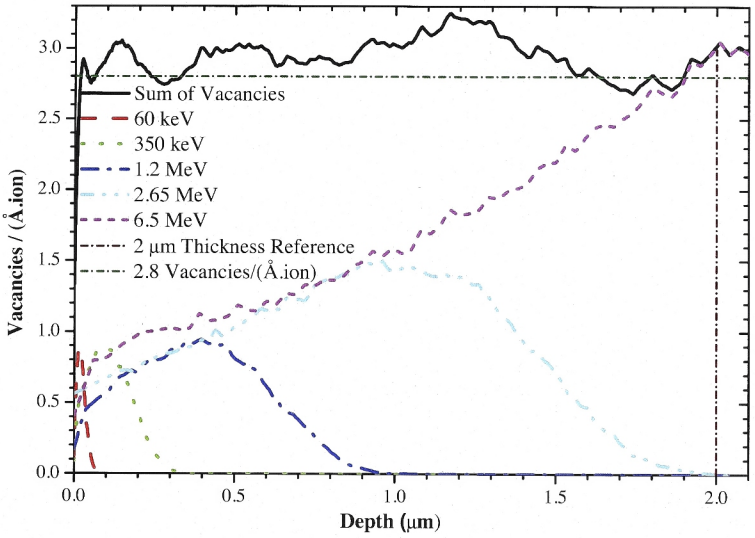

Figure 3-2 Vacancy profile for multiple energy As implants into 2 µm $In_{0.53}Ga_{0.47}As$.

RBS-C was used to measure the implantation-induced disorder on the In sub-lattice for $In_xGa_{1-x}As$ and InAs samples and on the Ga/As sub-lattices for GaAs samples. The In sub-lattice was chosen for $In_xGa_{1-x}As$ as, in this case, the Ga/As sub-lattice has scattering contributions from the In sub lattice as well. RBS-C measurements were performed along the <100> direction with 2.0 MeV He ions and a scattering angle of 168°. A lesser scattering angle would have yielded superior depth resolution but inferior mass resolution. The choice of scattering angle was governed by the need to avoid the overlap of scattering contributions from In and Ga/As atoms within the implanted layer. From the RBS-C spectra, the backscattered ion yield was integrated over a depth range (typically 50 – 350 Å) to determine $\Delta\chi_{min}$ (see section 2.2).

In Chapter 2, Figure 2-6 showed a representative RBS-C spectra of $In_{0.53}Ga_{0.47}As$ (0.6 µm thick) as a function of fluence, showing only scattering contributions from the In

sub-lattice. Clearly an increase in fluence resulted in an increase in backscattered ion yield consistent with the progression of the crystalline-to-amorphous phase transformation [12].

In the SRIM simulations, displacement energies of 25 eV were used for all atoms. $\Delta\chi_{min}$ data as a function of η_{dpa} was fit to the defect interaction and amorphisation model of Hecking *et al.* [22, 25] to determine the probabilities for direct-impact and stimulated amorphisation, P_a and A_s, respectively. Figure 3-3 (a) shows the effect on the Hecking curve of varying P_a while keeping A_s fixed and Figure 3-3 (b) shows the effect on the Hecking curve as A_s is varied while keeping P_a remains unchanged. In general, a decrease in P_a yields an increase in slope while a decrease in A_s shifts the curve to higher η_{dpa} values.

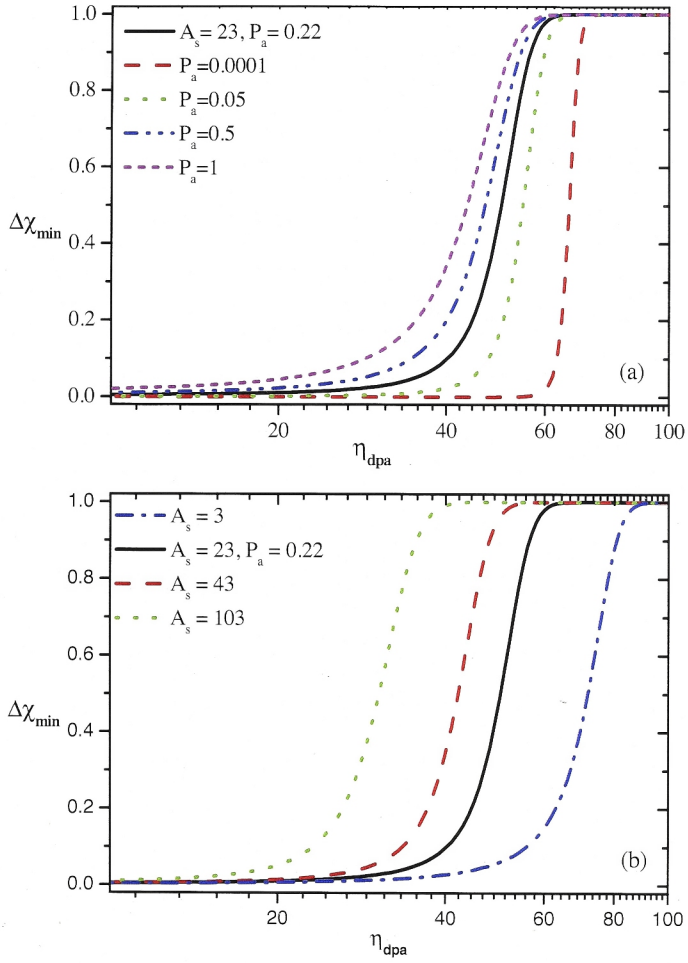

Figure 3-3 Simulation of effect of varying (a) P_a and (b) A_s on the Hecking curves.

As $\Delta\chi_{min}$ approaches unity, the slope approaches zero, yielding significant ambiguity in quantifying the η_{dpa} value required for complete amorphisation. Given the subtle differences in the amorphisation kinetics of the $In_xGa_{1-x}As$ alloys presented below, it

was necessary to reduce the uncertainty in the comparative study by defining the "critical η_{dpa}" as the inflection point of the Hecking fit.

For EXAFS samples measured in transmission mode, the sample thickness is governed by the absorption length ($1/\mu$). It is the distance over which the x-ray intensity decreases by a factor of 1/e or approximately 37%. For $\ln(I_o/I_t) = \mu t = 1$, the sample thickness (t) will be one absorption length. For $In_xGa_{1-x}As$ the sample thickness required is approximately between 8 – 12 μm depending on which edge is to be measured. The maximum layer thickness grown, without compromising the epitaxial quality, was about 2 μm for non lattice matched $In_xGa_{1-x}As$. These layers were removed from the substrate (described below) and then stacked together to give the appropriate thickness for the edge to be measured at.

Prior to the EXAFS measurements, the epitaxial $In_xGa_{1-x}As$ layer was separated from the substrate by dissolving the latter using a selective chemical etchant ($HCl:H_2O$ or $H_2O_2:NH_4OH$ to dissolve InP or GaAs, respectively) [69-73]. These epitaxial layers were then stacked together to achieve the desired thickness. Removal of the substrate was necessary to eliminate contributions from In, Ga and/or As atoms in the substrate to the measured EXAFS spectra of the ternary alloy layers. In the case of implanted material, it was essential to etch off the substrate prior to implantation as damage/implantation reduced the selectivity of the etchants.

Multiple As implants were used for the 2 μm thick $In_{0.53}Ga_{0.47}As$ so as to damage/amorphise the entire epitaxial layer. This was necessary so as to have data from only implanted material. As ions were used instead of Ge ions to amorphise the layer

used for EXAFS measurements so as to avoid contributions from Ge atoms in the EXAFS signal for the Ga K - edge.

EXAFS measurements were performed in the transmission mode at the In, Ga and As K edges. Si (311) and (111) monochromators, the latter detuned by 50%, were utilised at the In and Ga/As edges, respectively.

ATHENA was used for background removal and normalisation of the spectra. Structural parameters were then determined with ARTEMIS over a photo-electron wavenumber (k) range of ~ 3 – 15 $Å^{-1}$ and non-phase-corrected radial distance (r) range of ~ 1.7 – 4.5 Å. The choice of k range is determined by the quality of the data and wanting to avoid contributions from the XANES region. The r range is determined by the range at which the fit needs to be performed. For each sample, the In, Ga and As spectra were fit simultaneously with the bond lengths and Debye-Waller factors for a given pair of atoms set equal for the analysis of data at each K edge. For each bond type (Ga-As and In-As), the first nearest neighbour (NN) and next nearest neighbour (NNN) distances were extracted from which the bond angles for each NNN configuration were then calculated. A complete multiple-scattering analysis was applied. Both ATHENA and ARTEMIS are part of the IFEFFIT [63, 64] code for EXAFS data analysis.

3.3 Results and Discussion

3.3.1 RBS-C

With the exception of $In_{0.53}Ga_{0.47}As/InP$, all $In_xGa_{1-x}As$ layers were lattice mismatched with their respective substrates, generating misfit dislocations within the epitaxial layer during the growth process. For our given lattice mismatched stoichiometries and

substrates, a layer thickness of 0.1 μm exceeded the critical layer thickness reported by Anderson *et al.* [74] based on the pioneering work of Matthews and Blakeslee [75]. Epitaxial layers up to the critical thickness are strained but free of dislocations. Beyond the critical layer thickness, the strain is relieved due to the formation of dislocations which is the energetically favourable route compared with a strained structure [76]. Figure 3-4 shows the presence of misfit dislocations in a plan-view TEM image of $In_{0.20}Ga_{0.80}As$ viewed under two-beam, dark field conditions. The dislocations observed are 60^0 type oriented along the <110> direction, consistent with the work of Edirisinghe *et al.* [77].

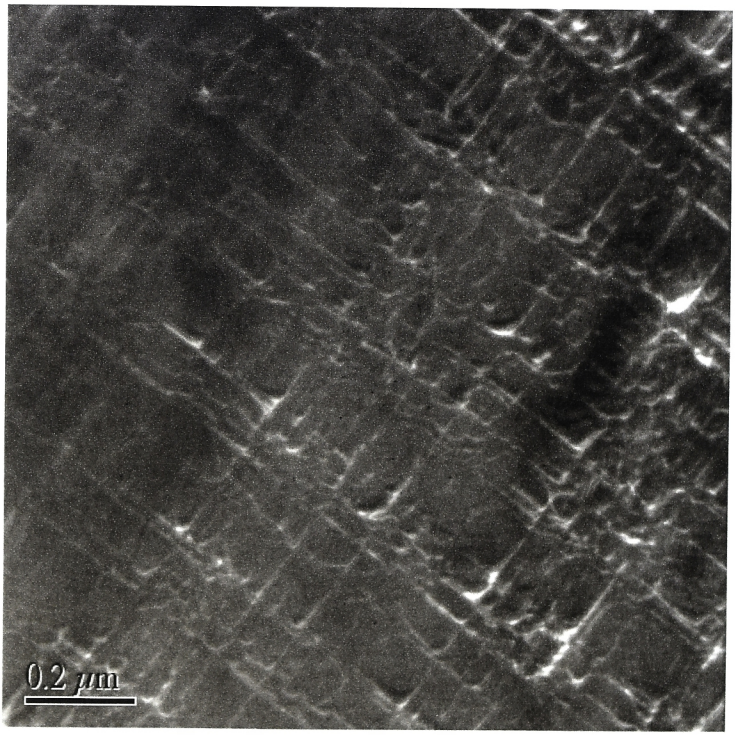

Figure 3-4 Plan view TEM image of $In_{0.20}Ga_{0.80}As$ imaged under two beam, dark field condition, showing the presence of misfit dislocations.

To assess the potential influence of misfit dislocations on the amorphisation kinetics, $In_{0.53}Ga_{0.47}As$ was grown on both lattice-matched InP and lattice-mismatched GaAs yielding epitaxial layers without and with dislocations, respectively. Ion implantation was then performed on both samples simultaneously followed by RBS-C measurements. Figure 3-5 shows $\Delta\chi_{min}$ data as a function of η_{dpa} and the respective fits to the Hecking model.

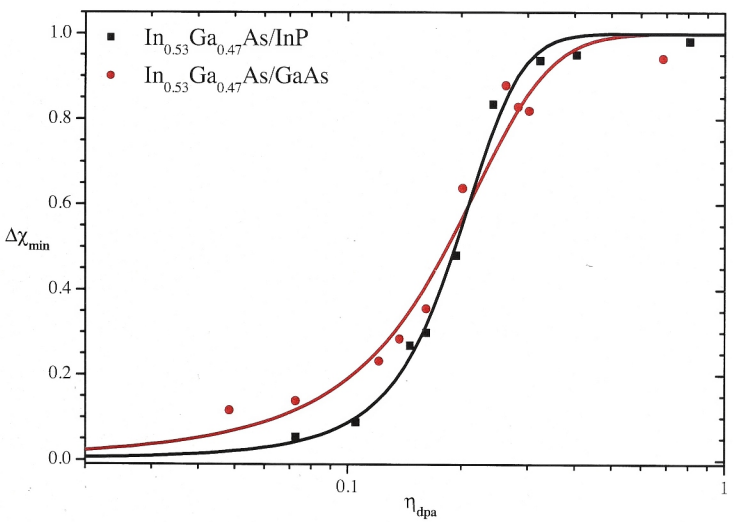

Figure 3-5 $\Delta\chi_{min}$ as a function of the number of displacements per atom comparing $In_{0.53}Ga_{0.47}As$ grown on InP and GaAs. The curves are fits to the experimental data points.

Note that such a comparison (as in Figure 3-5) represents a "worst-case scenario" with the greatest lattice mismatch between the ternary alloy and substrate for all samples examined in this study (as manifested by $Y_{unimplanted}$ values of ~ 0.80 and ~ 0.05 for lattice mismatched and matched samples, respectively). Nevertheless, equal values of

critical η_{dpa} (0.18 ± 0.05 and 0.19 ± 0.04 η_{dpa} for $In_{0.53}Ga_{0.47}As$ with and without dislocations, respectively) were determined. The probability of direct impact amorphisation differed by a factor of five for samples with (1.03 ± 0.25) and without (0.23 ± 0.05) dislocations whilst that for stimulated amorphisation in the dislocated alloy (13.9 ± 2.4) was half that of the dislocation-free sample (24.12 ± 1.7). Dislocations are known to getter mobile defects and impurities; this explains the higher value of stimulated amorphisation for samples with dislocations. Nevertheless, clearly implantation-induced disorder production in $In_{0.53}Ga_{0.47}As$ is dominated by stimulated amorphisation regardless of the presence of misfit dislocations. Furthermore, both samples have a lesser critical η_{dpa} value than InAs and GaAs (shown below in Figure 3-6), demonstrating that the rapid amorphisation behaviour did not result from the presence of pre-existing extended defects.

Figure 3-6 shows the fits for $\Delta\chi_{min}$ as a function of η_{dpa} over the entire stoichiometry range and includes the two fits for $In_{0.53}Ga_{0.47}As$ presented in Figure 3-5. For clarity, individual experimental points have not been included. It is readily apparent that the ternary alloys of $In_xGa_{1-x}As$ with stoichiometry $x \leq 0.53$ are amorphised at η_{dpa} values less than those required for both InAs and GaAs. In contrast, the In-rich alloys with $x \geq 0.75$ are rendered amorphous at η_{dpa} values intermediate between those necessary for the two binary extremes.

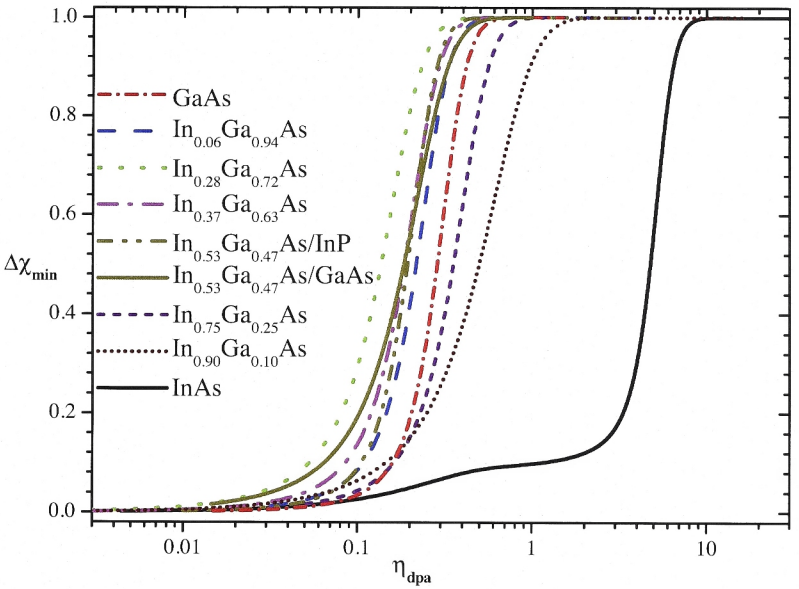

Figure 3-6 $\Delta\chi_{min}$ as a function of the number of displacements per atom measured over the entire stoichiometry range x for $In_xGa_{1-x}As$. The curves are fits to the experimental data points with the latter not shown for clarity.

Values of critical η_{dpa} and the parameters P_a and A_s, the latter derived from fits to the $\Delta\chi_{min}$ data, are plotted as a function of stoichiometry in Figure 3-7.

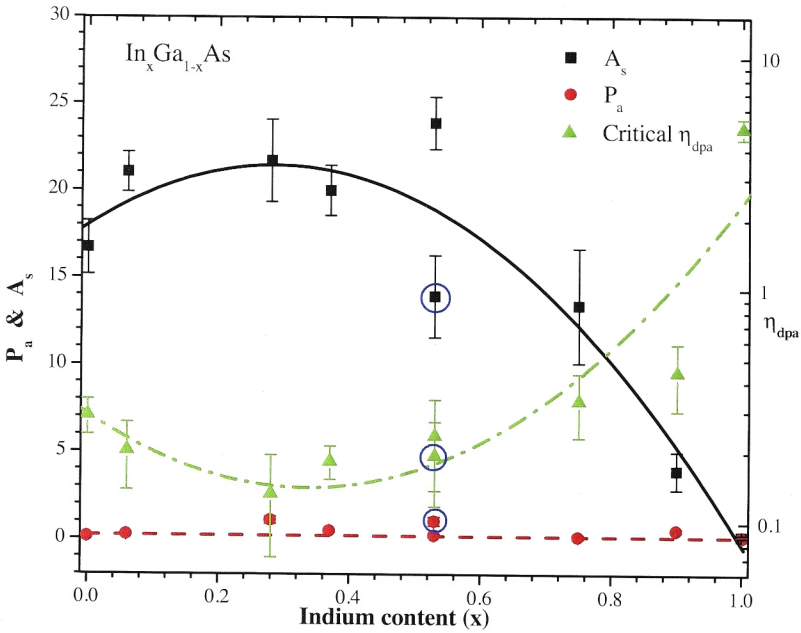

Figure 3-7 Critical η_{dpa} and probabilities for direct impact (P_a) and stimulated (A_s) amorphisation as a function of stoichiometry for $In_xGa_{1-x}As$. The circled values denote data from $In_{0.53}Ga_{0.47}As$/GaAs samples.

The quadratic fit to the η_{dpa} data indicates that an $In_xGa_{1-x}As$ alloy with stoichiometry of $x = 0.34 \pm 0.17$ is most easily amorphised. P_a is effectively independent of stoichiometry while A_s exhibits parabolic behaviour with a maximum at $x = 0.28 \pm 0.18$. Note the maximum in A_s is well correlated with the minimum in critical η_{dpa}. Clearly a stimulated amorphisation process (A_s) is dominant relative to direct impact amorphisation (P_a) over the entire stoichiometry range and the differences in critical η_{dpa} value as a function of stoichiometry are governed by differences in the probability for stimulated amorphisation. This preference for stimulated amorphisation is most likely due to bond angle distortions present in the $In_xGa_{1-x}As$ alloy giving rise to preferential nucleation sites for amorphous phase formation, as will be investigated in the next section.

3.3.2 EXAFS

To identify the atomistic configurations responsible for the amorphisation behaviour described above, EXAFS was utilised to probe the short-range order about the relevant constituent atoms of the binary and ternary compounds.

Figure 3-8 shows Fourier-transformed EXAFS spectra of unimplanted GaAs, $In_{0.53}Ga_{0.47}As$ and $Al_{0.50}Ga_{0.50}As$ measured at the Ga K edge. A nearest neighbour (NN) peak is apparent in all spectra at a non-phase-corrected radial distance of 2.1-2.3 Å. The NN shell about a Ga atom for GaAs, $In_{0.53}Ga_{0.47}As$ and $Al_{0.50}Ga_{0.50}As$ comprises of four As atoms. The amplitude of the NN peak is governed by multiple influences including an atomic-number (Z), dependence of the scattering factor for the atoms of the NN shell, an inverse square ($1/R^2$) dependence on radial distance to account for the loss of intensity of outgoing and scattered photo-electron waves (where R is the radial distance separating absorbing and scattering atoms) and the presence of structural disorder (characterised by the Debye-Waller factor). The Fourier transforms shown here are non-phase-corrected and hence the apparent radial distances do not correspond to the actual bond lengths (see Table 3-1).

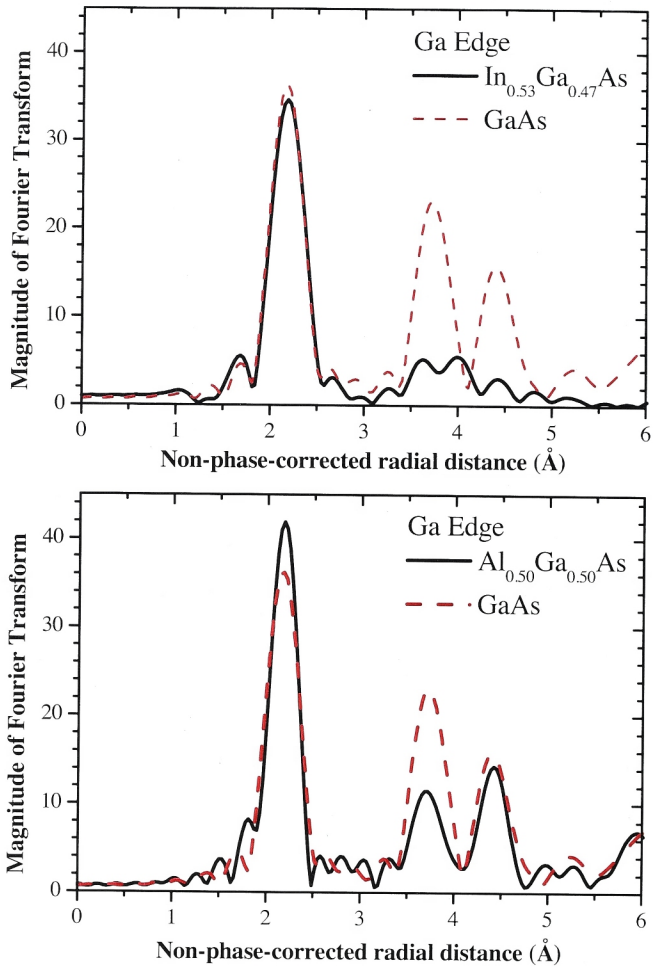

Figure 3-8 Fourier transform of EXAFS spectra measured at the Ga K edge for crystalline GaAs, lattice matched $In_{0.53}Ga_{0.47}As$ and $Al_{0.50}Ga_{0.50}As$.

Consider now the next-nearest neighbour (NNN) peak in Figure 3-8 at a non-phase-corrected radial distance of 3.7 - 4.0 Å. (consisting of Ga in GaAs, In and Ga in $In_{0.53}Ga_{0.47}As$ and Al and Ga in $Al_{0.50}Ga_{0.50}As$ atoms (12 in total)). The amplitude of the NNN peak in $In_{0.53}Ga_{0.47}As$ is clearly much smaller than those of GaAs and

$Al_{0.50}Ga_{0.50}As$ consistent with enhanced structural disorder in the bond-angle distribution (see Table 3-1 later in the text). For a perfect zinc-blende structure, the NNN amplitude for $In_{0.53}Ga_{0.47}As$ would be greater than that of GaAs and $Al_{0.50}Ga_{0.50}As$ given In is a stronger scatterer than both Al and Ga. The slight reduction in NNN amplitude of $Al_{0.50}Ga_{0.50}As$ compared with GaAs is expected, since in $Al_{0.50}Ga_{0.50}As$ the NNN shell is a mix of both Al and Ga, compared with just Ga in GaAs, with Al being a weaker scatterer than Ga. This shows that even in the crystalline form, $In_{0.53}Ga_{0.47}As$ has a pronounced disorder around the NNN shell compared with $Al_{0.50}Ga_{0.50}As$. Given the disorder is around the NNN shell, this suggests that the disorder is due to bond angle distortions.

Structural disorder also results from ion implantation and can be studied using EXAFS. Figure 3-9 shows the non-phase corrected radial distribution of $In_{0.53}Ga_{0.47}As$ as a function of the nuclear energy deposition, η_{dpa}. The amplitude of the NN and NNN peaks decrease with increasing η_{dpa}, indicative of increased structural disorder. A reduction in the NNN peak amplitude implies a loss of long range order characteristic of disordered materials. For the highest η_{dpa} value of 1.76 the NNN peak is non-existent, hence suggesting that $In_{0.53}Ga_{0.47}As$ is rendered amorphous at this ion fluence, consistent with RBS-C results.

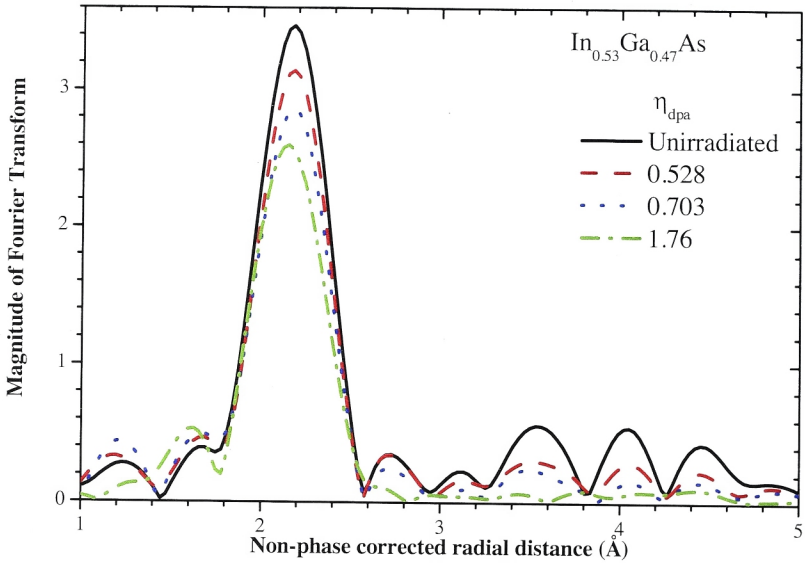

Figure 3-9 Fourier transform of EXAFS spectra measured at the Ga K edge as a function of ion fluence for $In_{0.53}Ga_{0.47}As$.

Using ARTEMIS [63] the EXAFS data for crystalline InAs, GaAs, $Al_{0.50}Ga_{0.50}As$ and $In_xGa_{1-x}As$ were fit using conditions described previously in section 3.2. These fits were in excellent agreement with the back transformed experimental data, as shown in Figure 3-10 - Figure 3-13 for the common As K edge for these materials. All other fits are shown in the Appendix. The parameters determined from these fits are shown in Table 3-1.

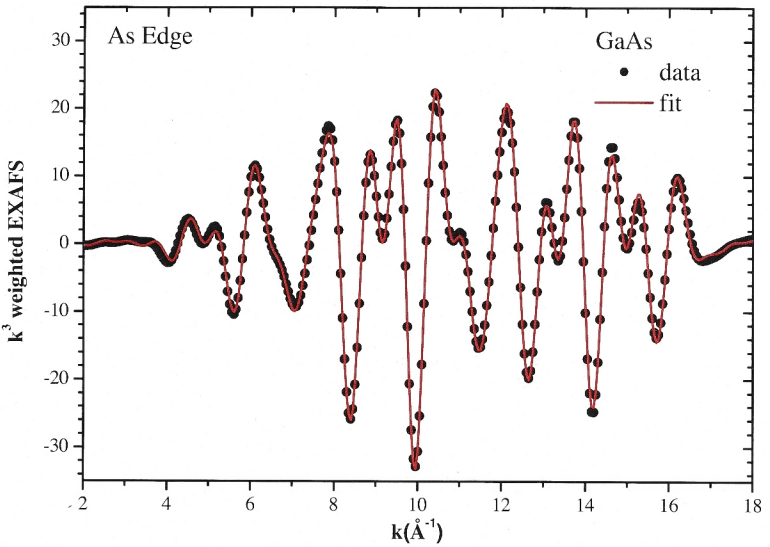

Figure 3-10 Best fit for GaAs at the As K - edge to k^3 weighted back-transformed experimental data using ARTEMIS.

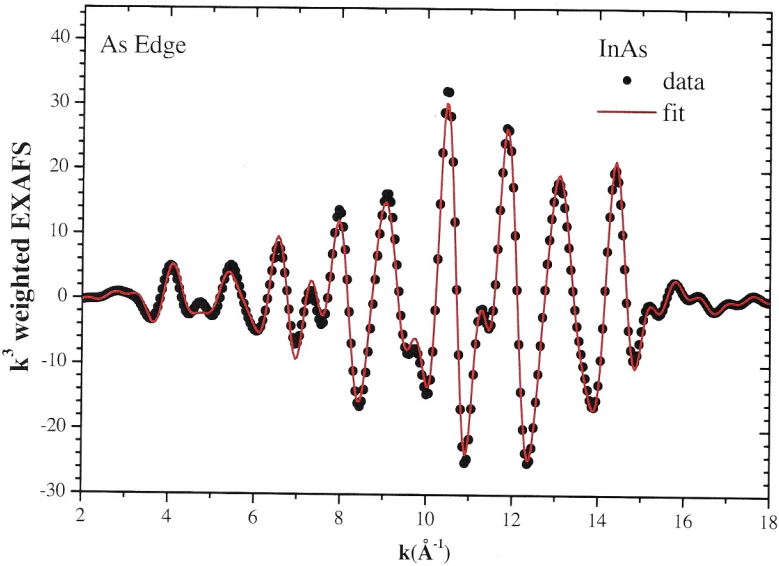

Figure 3-11 Best fit for InAs at the As K - edge to k^3 weighted back-transformed experimental data using ARTEMIS.

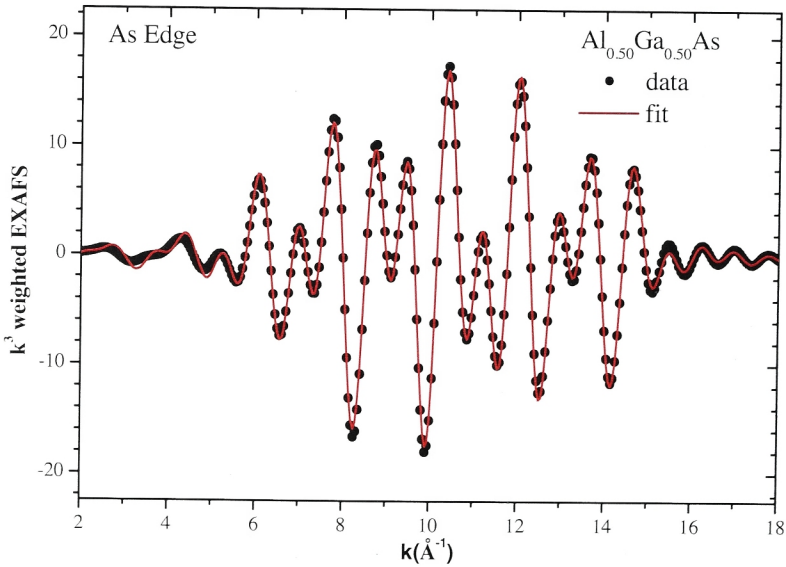

Figure 3-12 Best fit for $Al_{0.50}Ga_{0.50}As$ at the As K – edge to k^3 weighted back-transformed experimental data using ARTEMIS.

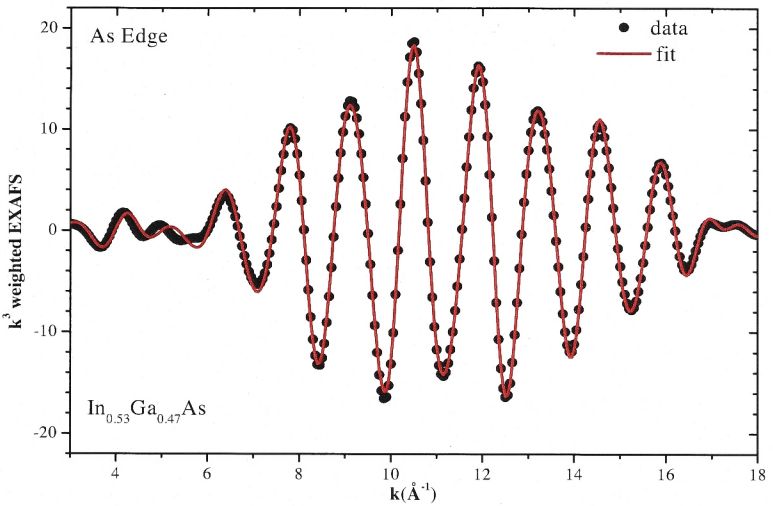

Figure 3-13 Best fit for$In_{0.53}Ga_{0.47}As$ at the As K – edge to k^3 weighted back-transformed experimental data using ARTEMIS.

Material	Bond (NN/NNN)	Bond Length (Å)		Angle	θ°	DWF_{NNN} (As-In-As/As-Ga-As)
		NN	NNN			
InAs	In-As/In-In	2.609 ± 0.002	4.273 ± 0.005	In-As-In	109.5 ± 0.2	0.0036 ± 0.0004
GaAs	Ga-As/Ga-Ga	2.437 ± 0.002	3.986 ± 0.004	Ga-As-Ga	109.7 ± 0.2	0.0039 ± 0.0008
$Al_{0.50}Ga_{0.50}As$	Al-As	2.439 ± 0.022		-	-	
	Ga-As/Ga-Ga	2.444 ± 0.001	3.995 ± 0.008	Ga-As-Ga	109.6 ± 0.2	0.0048 ± 0.0002
$In_{0.28}Ga_{0.72}As$	In-As	2.594 ± 0.004		-	-	0.01 ± 0.002
	Ga-As/Ga-Ga	2.454 ± 0.002	4.072 ± 0.01	Ga-As-Ga	112.3 ± 0.3	0.0073 ± 0.0008
$In_{0.53}Ga_{0.47}As$	In-As/In-In	2.591 ± 0.003	4.176 ± 0.006	In-As-In	107.5 ± 0.3	0.01 ± 0.002
	Ga-As/Ga-Ga	2.466 ± 0.003	4.104 ± 0.012	Ga-As-Ga	113.4 ± 0.5	0.0086 ± 0.0019
$In_{0.75}Ga_{0.25}As$	In-As/In-In	2.598 ± 0.003	4.192 ± 0.012	In-As-In	107.6 ± 0.5	0.0091 ± 0.0012
	Ga-As/Ga-Ga	2.47 ± 0.003	4.133 ± 0.045	Ga-As-Ga	113.6 ± 1.2	0.006 ± 0.0014

Table 3-1 Bond lengths, bond-angles and Debye Waller factors (DWF) calculated from EXAFS spectra of InAs, GaAs, $Al_{0.50}Ga_{0.50}As$ and $In_xGa_{1-x}As$.

Bond angles shown in Table 3-1 were determined using the bond lengths for the NN (R_{InAs} and R_{GaAs}) and the NNN ($R_{As\text{-}As}$) as shown schematically in Figure 3-14. Here, In and Ga are the NN and As is the NNN atom with As* as the central or absorbing atom. The measured bond lengths were used to determine the average bond angle (θ) between the absorber and the NNN atoms using Eq. 3.1. In addition, the Debye-Waller factor (DWF) was also determined from these fits. Values of these bond lengths, bond angles and DWF are also listed in Table 3-1 above.

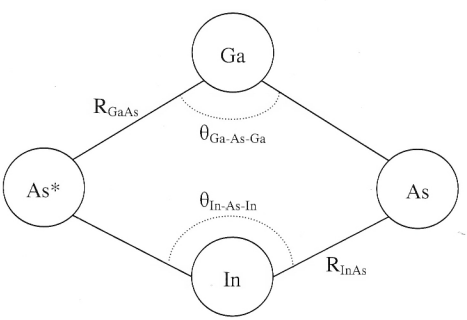

Figure 3-14 Schematic of bond length and bond angle for InGaAs.

$$\theta_{GaAs} = \cos^{-1}\left(\frac{2R_{GaAs}^2 - R_{AsAs}^2}{2\ R_{GaAs}^2}\right)\frac{180}{\pi} \tag{3.1}$$

Bond length values given in Table 3-1 are in good agreement with the theoretical values reported by Cai and Thorpe using the effective medium approximation (EMA) [39] and the experimental works of Mikkelsen and Boyce ($In_xGa_{1-x}As$) [40], Azevedo (InAs) [78] and Glover (GaAs) [79] *(see Table A-1 in the Appendix)*.

The NN bond lengths for GaAs, InAs and $In_xGa_{1-x}As$ from Table 3-1 are plotted in Figure 3-15 as a function of stoichiometry. In the Vegard limit, the ternary alloy is characterised by one common bond length (In-As = Ga-As) that varies as a function of stoichiometry. In contrast, two separate stoichiometry-independent bond lengths (In-As ≠ Ga-As) are predicted in the Bragg-Pauling limit. Predictions from the Vegard [80] and Bragg–Pauling [81, 82] models are also included in Figure 3-15. The experimental data shown in Figure 3-15 are clearly intermediate between the Vegard and Bragg-Pauling models resulting in a bimodal bond-length distribution in $In_xGa_{1-x}As$.

Cai and Thorpe [39, 83] defined a topological rigidity parameter (a**) as a measure of the dominant force constant. For a ternary compound ABC, a** is defined as:

$$a^{**}_{A-B} = 1 - \frac{R_{AB} - R'_{AB}}{R_{AB} - R_{BC}} \tag{3.2}$$

Where R_{AB} and R_{BC} are the unstrained or natural bond length of the binary compounds and R'_{AB} is strained bond length of distance AB in the ternary compound. When a** = 1 only bond bending is active and when a** = 0 only bond stretching is active. The value of a** calculated from Figure 3-15 was 0.84 ± 0.01 and 0.73 ± 0.01 for the In-As and Ga-As bond-length distributions, respectively, in complete agreement with an average value of 0.80 reported previously [22, 25]. These results indicate that the bimodal bond-length distribution of the $In_xGa_{1-x}As$ alloys is accommodated by both bond stretching and bond bending, although primarily via the latter, as consistent with a higher force constant for bond stretching. Note that the bond-length and bond-angles in

$Al_{0.50}Ga_{0.50}As$ are very similar to those in GaAs, and thus microscopic strain in this ternary alloy is minimal.

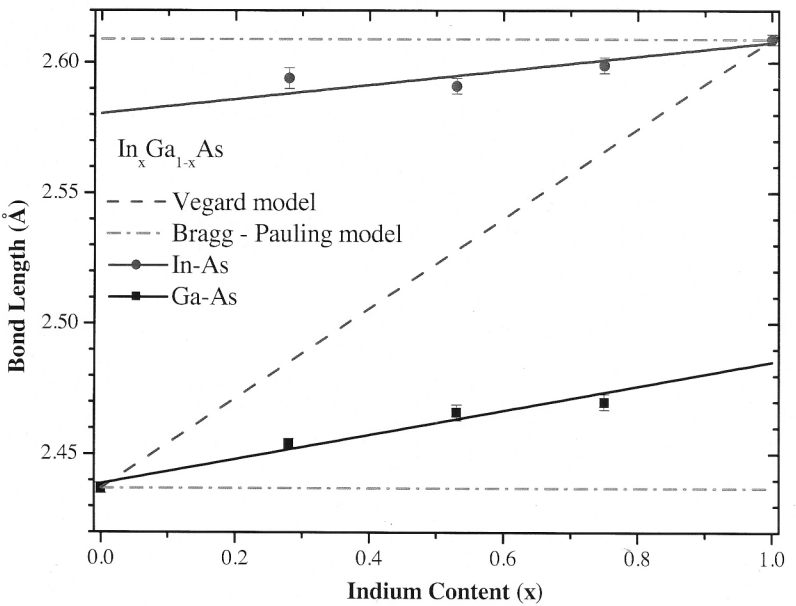

Figure 3-15 Nearest-neighbour bond lengths (In-As and Ga-As) for unimplanted $In_xGa_{1-x}As$ as a function of stoichiometry. The Vegard and Bragg-Pauling limits are included for comparison.

Referring again to Table 3-1, the tetrahedral value of 109.5° for the bond angle was measurable for the two binaries as expected and $Al_{0.50}Ga_{0.50}As$ where the bond-length distribution is effectively unimodal. In contrast, deviations from 109.5° are apparent for $In_xGa_{1-x}As$. Note that the bond angles comprised of two long (short) In-As (Ga-As) bonds are less (greater) than the tetrahedral value, as one might intuitively expect.

Figure 3-16 shows DWFs as a function of stoichiometry for the NNN shell about an As atom in $In_xGa_{1-x}As$. Structural disorder at the NNN shell in the ternary alloy is

significantly greater than that of the two binaries with a maximum at x = ~ 0.46. Note that this maximum in disorder is well correlated with the stoichiometry most easily amorphised as shown in Figure 3-7 (critical η_{dpa}) and discussed in section 3.3.1. Comparable results for structural disorder at the NNN shell have been reported by Jeong *et al.* [84] using complementary synchrotron-based x-ray diffraction to determine atomic pair distribution functions. Examining the $In_xGa_{1-x}As$ alloys as a function of stoichiometry, they observed a broadening of the peak widths for the NNN shell due to increased structural disorder with the latter a maximum for x = ~ 0.5. The results reported here agree well with those of Jeong *et al.* [84]. Jeong *et al.* further demonstrated that atomic displacements on the In/Ga sublattice were isotropic and of lesser magnitude (~ 60%) than the highly directional (<100> and <111>) displacements on the As sublattice. Such behaviour can also be studied using EXAFS as has been demonstrated by Schnohr *et al.* [85] where they measured anisotropic vibrations in crystalline and amorphous InP. They concluded that relative vibrations along the bond require bond stretching, however, this is not energetically favourable in III-V zinc-blende semiconductors. Relative vibrations perpendicular to the bond, however, change the bond angle that is energetically favoured in these III-V materials.

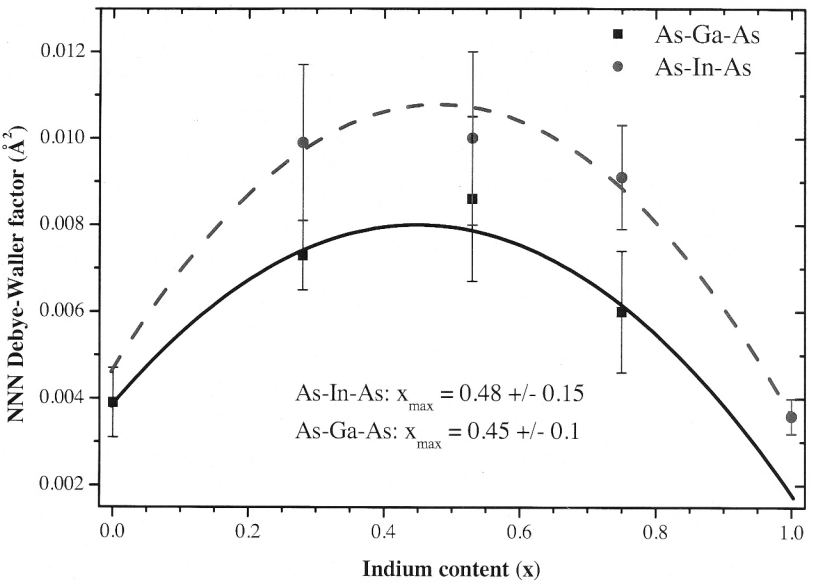

Figure 3-16 Debye-Waller factor for the next nearest neighbour about an As atom in unimplanted $In_xGa_{1-x}As$ as a function of stoichiometry.

Accommodating two distinctly separate bond lengths on the zinc-blende lattice as opposed to two very similar bond lengths, yields greater structural disorder in the inter-atomic distance distribution of the atoms comprising the NNN shell. Correlating EXAFS and RBS-C measurements, this study of the amorphisation of the $In_xGa_{1-x}As$ alloys as a function of stoichiometry has clearly demonstrated that the minimum in critical η_{dpa} was very well correlated with both the maxima in the probability for stimulated amorphisation (Figure 3-7) and the structural disorder at the next nearest neighbour shell (Figure 3-16). Thus, the structural disorder in the ternary alloys, concentrated primarily in the bond-angle distributions, appears to give rise to preferential sites for stimulated amorphisation, rendering the $In_xGa_{1-x}As$ alloys amorphous at lesser critical η_{dpa} values than for both InAs and GaAs.

3.4 Conclusion

The kinetics for the ion-implantation-induced amorphisation of $In_xGa_{1-x}As$ were determined with RBS-C over the entire stoichiometry range. Stoichiometries of x = ~ 0.06 – 0.53 were rendered amorphous at fluences lower than those required for the binary extremes. The crystalline-to-amorphous phase transformation was dominated by a stimulated amorphisation process, the probability for which was a maximum at the stoichiometry most easily amorphised. EXAFS measurements demonstrated the bimodal bond length distribution characteristic of the $In_xGa_{1-x}As$ alloy was primarily accommodated on the zinc-blende lattice via bond bending with deviations from the tetrahedral bond angle readily apparent in the $In_xGa_{1-x}As$. Correlating EXAFS and RBS-C measurements, structural disorder and the probability of stimulated amorphisation were both greatest at a common intermediate stoichiometry, where the ternary alloy was most easily amorphised. The anomalous amorphisation is clearly correlated with a bimodal bond length distribution. The latter yields structural disorder manifested as an increased NNN DWF that is largely accommodated in the bond angle distribution given bond bending is energetically favoured over bond stretching. We suggest this structural disorder serves as preferential nucleation sites for amorphous phase formation.

The validity of this model will be tested in the next chapter for $In_xGa_{1-x}P$ alloys as they exhibit a bimodal bond length distribution [41] similar to that observed in $In_xGa_{1-x}As$.

Chapter 4 $In_xGa_{1-x}P$

4.1 Introduction

$In_xGa_{1-x}P$ ternary alloys have attracted attention from the electronics industry as they are a good alternative to $Al_xGa_{1-x}As$ based devices. In addition $In_xGa_{1-x}P$ alloys exhibit one of the widest direct band gaps among non-nitride III-V semiconductors, making them attractive for the optoelectronics industry [86] especially as light-emitting diodes. Recently, $In_xGa_{1-x}P$ has also been investigated for possible use in solar cells [87-95] particularly in spatial and terrestrial applications due to its increased efficiency and superior radiation resistance.

Akano *et al.* [36] studied the amorphisation in InP at 80 K and RT using 330 keV O ions. They found an absence of any significant dynamic annealing for InP amorphisation under these conditions. Dynamic annealing in InP was not evident until at least 348 K. Similar results were also reported by Wendler [16] for InP implanted at various temperatures using 300 keV Si ions. Bezakova *et al.* [96] studied the ion implantation induced amorphisation in InP at 77 K using the perturbed angular correlation technique. They concluded that the amorphisation process in InP could be described using the direct impact amorphisation process and overlap of the disordered regions.

Krynicki *et al.* [97] studied the crystalline to amorphous transformations in GaP at 130 K and RT using 150 keV N and Cd ions. They found that the ion fluence required to amorphise GaP at 130 K and RT is similar for the heavier Cd ions whereas the ion fluence required using the lighter (N) ions differ by a factor of 2. They attributed this

difference in amorphisation fluence for lighter ions to dynamic annealing and attributed the amorphisation behaviour of GaP in general to homogenous amorphisation.

Jones and Santana [98] studied the amorphisation behaviour of various binary semiconductors and found that InP was more easily amorphised than GaP at 77 K using 20 keV Si ions.

Wesch *et al.* [15] (the Jena group) compared the room temperature ion implanted damage as a function of fluence for various ion species and a range of energies from 200 keV to 10 MeV for GaAs, GaP, InAs and InP. They found a remarkable in situ annealing for InAs and GaAs, which increased with ion energy and depended also on the ion mass implanted. This in situ annealing was not observed in InP and GaP.

The Jena group did considerable work on the ion implanted damage in III-V semiconductors under various implantation conditions. This has lead to an excellent review paper [16] to which the reader is referred for an in depth understanding of the influence of implantation conditions and parameters such as: ion mass, implantation temperature, ion flux, ion energy and ion fluence.

Schnohr *et al.* [99] have studied the atomic structure of InP amorphised by electronic and nuclear ion energy loss process using EXAFS. They found that the observed amorphisation process was due to direct impact.

In Chapter 3 it was shown that bimodal bond length distribution is correlated with the rapid amorphisation observed in $In_xGa_{1-x}As$. This bimodal bond length distribution gives

rise to structural disorder that serves as preferential sites for stimulated amorphisation. It has been shown both theoretically [39] and experimentally [41, 100] that $In_xGa_{1-x}P$ also exhibits a bimodal bond length distribution.

Although various studies have been carried out on the amorphisation behaviour of InP and GaP [14, 15, 36, 96-99, 101-105], surprisingly no published data could be found for the crystalline to amorphous phase transformation of $In_xGa_{1-x}P$. Hence, to address this gap, in addition to investigating the amorphisation behaviour of $In_xGa_{1-x}P$ at 300 K, the amorphisation behaviour at 15 K was also investigated in this chapter. At 15 K any defect diffusion or annealing (due to thermal effects) is largely suppressed [23, 102, 106, 107] and thus the resulting disorder should be the result of the primary process of damage formation in that material.

In summary, the aim of this chapter was to study the 15 K and 300 K amorphisation kinetics of $In_xGa_{1-x}P$ over the entire stoichiometry range using RBS-C. EXAFS was utilised to determine the bond length and bond angle distributions for $In_xGa_{1-x}P$ samples used in this study.

4.2 Experimental

Epitaxial $In_xGa_{1-x}P$ layers with x = 0.34, 0.50, 0.64 and 0.88 with layer thickness of 1, 2.5, 0.5 and 0.1 μm, respectively, were grown by metal organic chemical vapour deposition (MOCVD) on GaAs (100) substrates that were 10° off-cut towards <110>. This off-cut is necessary to avoid the characteristic spinodal decomposition and ordering observed in $In_xGa_{1-x}P$ alloys [108-110]. An intermediate layer of 0.05 μm AlAs was deposited on the GaAs substrate prior to $In_xGa_{1-x}P$ deposition. This layer was grown at a

temperature of 700 °C with a V/III flow rate of 91. This layer can be etched to separate the $In_xGa_{1-x}P$ layer from the substrate using an AlAs selective chemical etchant (10 % HF:H_2O) [73]. The lattice matched $In_{0.50}Ga_{0.50}P$ layer was grown at a temperature of 550 °C with a V/III flow rate of 149. A lower growth temperature compared to that of $In_xGa_{1-x}As$ is used here to minimise ordering effects. All other $In_xGa_{1-x}P$ layers were grown under similar conditions.

300 K implants for $In_xGa_{1-x}P$ along with InP and GaP were performed using 60 keV ^{74}Ge ions. RBS-C was utilised as described in Chapter 2, section 2. Figure 4-1 shows the RBS-C spectra of $In_{0.50}Ga_{0.50}P$ as a function of ion fluence, showing only the scattering contributions from the In sub-lattice. Plotted here is the normalised yield from RBS-C against depth. It is clear from Figure 4-1 that an increase in ion fluence leads to an increase in the backscattered ion yield up to 4 x 10^{13} ions cm^{-2} where the normalised yield reaches the random level. Increasing the ion fluence above this value to 2 x 10^{14} ions cm^{-2}, results only in broadening of the damaged layer in to the depth of the material. The ion fluence was converted to η_{dpa} as per Eq. 3.2. Details of $\Delta\chi_{min}$, η_{dpa}, critical η_{dpa} and probabilities of direct-impact (P_a) and stimulated (A_s) amorphisation, have been outlined in Chapter 2 and Chapter 3.

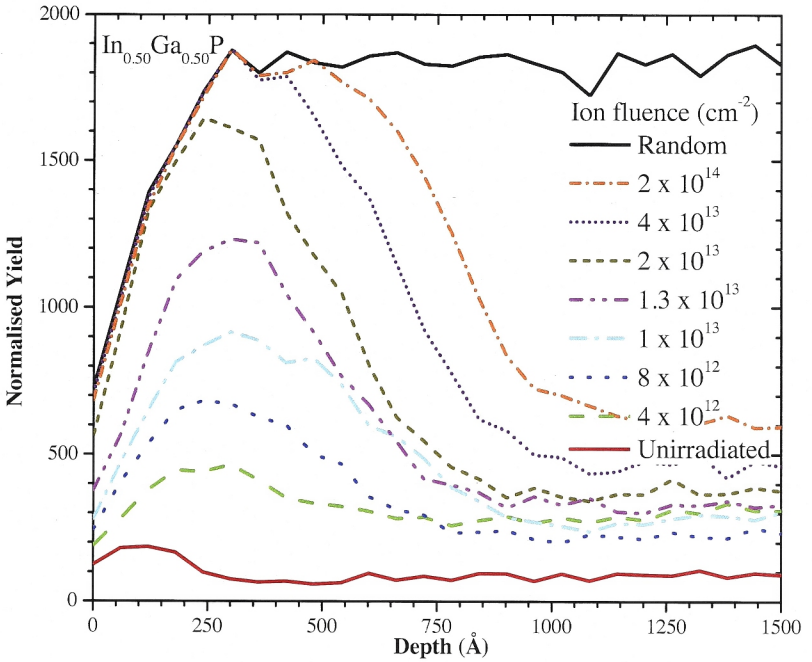

Figure 4-1 RBS-C spectra of $In_{0.50}Ga_{0.50}P$ irradiated at 300 K using 60 keV Ge ions.

For low temperature (15 K) implants, warming up of the samples between ion implantation and RBS-C measurements may change the primary defect distribution [111]. It is preferable to perform both the implantation and the RBS-C at these low temperatures. A facility to perform in situ ion implantation and RBS-C measurements is available at the Institut für Festkörperphysik, Friedrich-Schiller-Universität in Jena, Germany. The institute houses a special two-beam chamber where RBS-C measurements can be performed at 15 K immediately after ion implantation. This chamber is attached to two beamlines: a 400 kV implanter and a 3 MV accelerator. A detailed description of this setup can be found in reference [112].

EXAFS measurements for $In_xGa_{1-x}P$ with x = 0, 0.34, 0.50, 0.64 and 1, were performed at beamline 20-B of the Photon Factory in Japan. EXAFS data was collected at the In and Ga K edges in transmission mode at a temperature of ~ 10 – 15 K. $In_xGa_{1-x}P$ epitaxial layers were removed from the GaAs substrate by first masking the $In_xGa_{1-x}P$ layer with Apiezon wax and then dissolving the AlAs layer using a 10% $HF:H_2O$ solution as a selective etchant [73]. The wax was then dissolved using trichloroethylene and the epitaxial layer crushed and mixed with BN to make samples for EXAFS measurements. Structural parameters were determined over a photo-electron wavenumber (k) range of ~ 2 – 14 $Å^{-1}$ and non-phase-corrected radial distance of ~ 1.5 – 4.9 Å for the In edge and ~ 1.4 – 4.6 Å for the Ga edge data. Using these data, the first nearest neighbour (NN) and the next nearest neighbour (NNN) distances were determined. From these distances the bond angles for each NNN configuration were calculated (see Section 4.3.2). A complete multiple scattering analysis was applied.

4.3 Results and Discussion

4.3.1 RBS-C

With the exception of $In_{0.50}Ga_{0.50}P$/GaAs, all $In_xGa_{1-x}P$ layers were lattice mismatched with their respective substrates, generating misfit dislocations within the epitaxial layer during the growth process. For the given stoichiometries, the layer thickness exceeded the critical layer thickness reported by Kahn & Ritter [113]. Excluding the lattice matched $In_{0.50}Ga_{0.50}P$/GaAs, the lattice mismatch in $In_xGa_{1-x}P$ – GaAs is similar to that of $In_xGa_{1-x}As$ – InP and not worse than the worst case scenario considered for $In_xGa_{1-x}As$ in Section 3.3.1 where it was shown that the presence of misfit dislocations *does not* influence the critical η_{dpa} for the ternary alloy, $In_xGa_{1-x}As$.

4.3.1.1 Room Temperature (300 K) Implants

Figure 4-2 shows the fits for 300 K $\Delta\chi_{min}$ as a function of η_{dpa} over the entire stoichiometry range of $In_xGa_{1-x}P$. For clarity, individual experimental points have been excluded. For all stoichiometries investigated, it is apparent that the ternary alloy is amorphised at η_{dpa} values less than those required for either GaP or InP, with GaP having the highest η_{dpa} value, thus being the most difficult to amorphise. Compared with $In_xGa_{1-x}As$ from Chapter 3 where the difference in η_{dpa} values between InAs and GaAs was approximately two orders of magnitude, the difference in the case of $In_xGa_{1-x}P$ for GaP and InP is less pronounced. This difference is due to more prominent room temperature damage annealing in InAs compared with the other materials as discussed in Chapter 3.

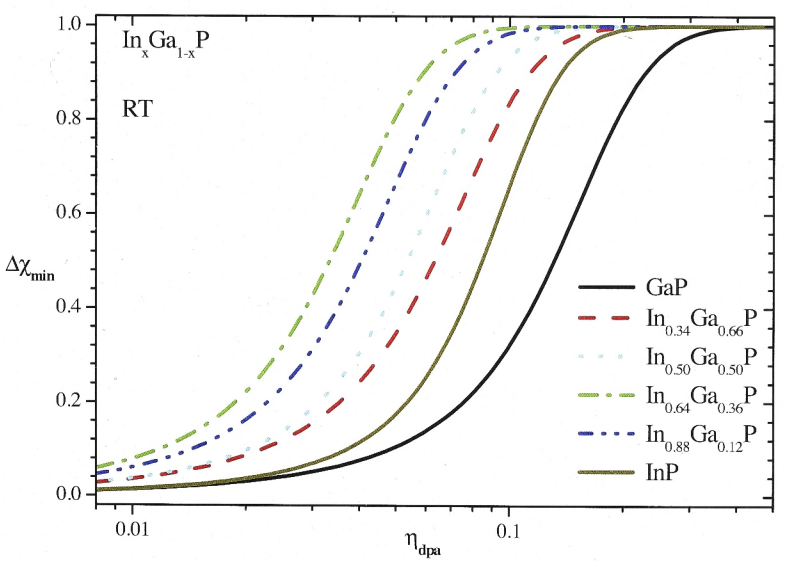

Figure 4-2 Delta $\Delta\chi_{min}$ as a function of η_{dpa} measured for $In_xGa_{1-x}P$ at 300 K. The curves are fits to the experimental data points with the latter not shown for clarity.

Values of P_a and A_s were derived from the fits in Figure 4-2 was described in Chapter 1 and Chapter 3 based on the Hecking model. Critical η_{dpa} values were also calculated from these plots. Values of η_{dpa}, and P_a and A_s are plotted in Figure 4-3 as a function of stoichiometry.

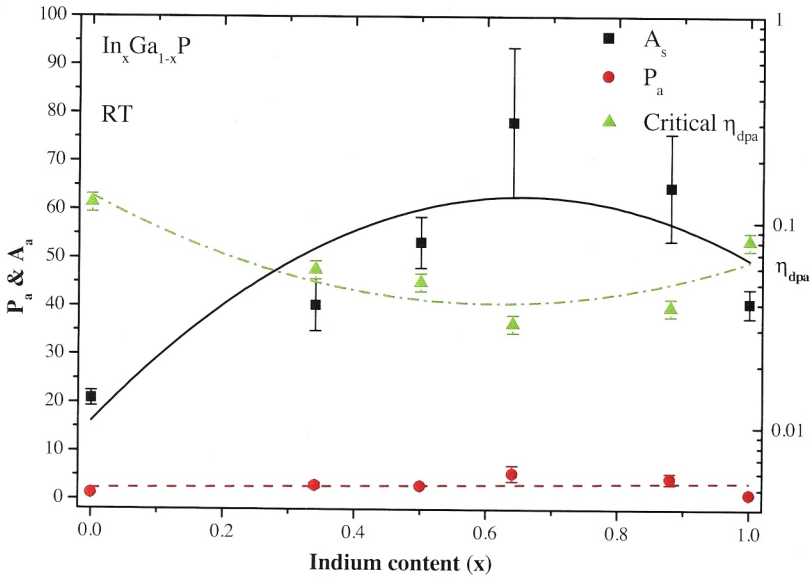

Figure 4-3 Critical η_{dpa} and probabilities of direct impact (Pa) and stimulated (As) amorphisation as a function of stoichiometry for 300 K implanted $In_xGa_{1-x}P$.

The quadratic fit to the η_{dpa} data indicates that $In_xGa_{1-x}P$ alloys with a stoichiometry of x = 0.65 +/- 0.25 were most easily amorphised. P_a is effectively independent of stoichiometry while A_s exhibits parabolic behaviour with a maximum at x = 0.61 +/- 0.23. Note that the maximum in A_s is well correlated with the minimum in critical η_{dpa}. Clearly a stimulated amorphisation process (A_s) is dominant relative to direct impact

amorphisation (P_a) over the entire stoichiometry range and the difference in critical η_{dpa} value as a function of stoichiometry are governed by differences in the probability of stimulated amorphisation. This behaviour is consistent with that observed for $In_xGa_{1-x}As$ in Chapter 3.

4.3.1.2 15 K Implants

The amorphisation kinetics of $In_xGa_{1-x}P$ were also investigated at 15 K. Low temperature ion implantation enables the investigation of the primary process of damage production, as at sufficiently low temperatures defects are not mobile and there is no thermal annealing of defects.

Figure 4-4 shows the $\Delta\chi_{min}$ curves of $In_xGa_{1-x}P$ samples implanted at 15 K. The amorphisation kinetics of the ternary $In_xGa_{1-x}P$ at 15 K are clearly different from those observed at 300 K. In the case of 15 K implantation, the amorphisation kinetics of the ternary compounds are intermediate between the two binary extremes. These results are similar to those reported for $Al_xGa_{1-x}As$ [23] and $In_xGa_{1-x}As$ [114] at this temperature.

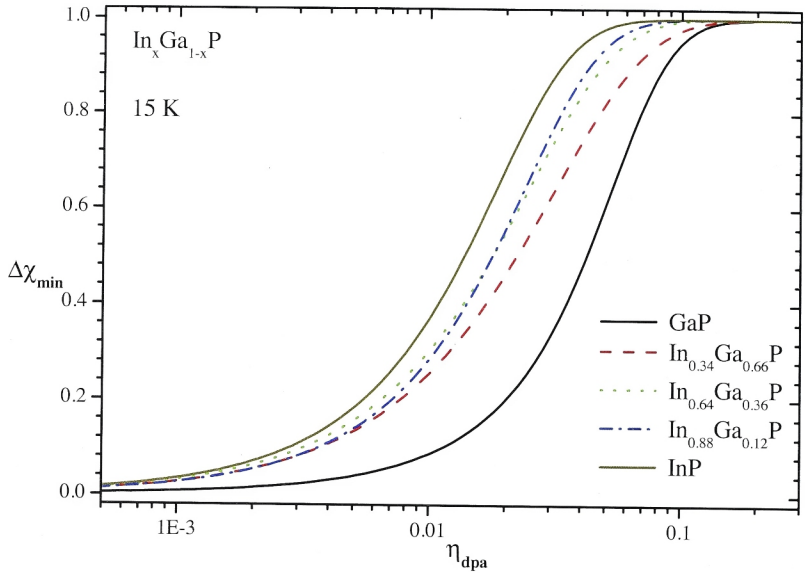

Figure 4-4 Delta $\Delta\chi_{min}$ as a function of η_{dpa} measured for $In_xGa_{1-x}P$ at 15 K. The curves are fits to the experimental data points with the latter not shown for clarity.

The critical η_{dpa} value at 15 K is smaller for all materials by approximately a factor of three, except in the case of InP where this difference is greater and is approximately a factor of six less than that observed at 300 K. In general, at 300 K, point defects are partially mobile, resulting in a pronounced in-situ defect recombination and annealing effect. However, at 15 K, the primarily produced defects are stable and thus, to amorphise materials at this low temperature, smaller values of η_{dpa} are required. This however, does not explain the greater reduction in η_{dpa} value observed for InP.

A possible explanation for the InP behaviour at 15 K can be derived from the atomic force constant, f. The cross-section of damage formation for binary III-V compounds at 15 K has been shown to have a systematic dependence on the atomic force constant [115]. This atomic force constant is taken as a measure of bond-strength, with a higher

force constant (i.e. higher bond-strength) resulting in a lower cross-section of damage formation and thus requiring higher η_{dpa} for amorphisation. The greater reduction in the η_{dpa} value of InP at 15 K can be explained by the lower force constant observed in InP (0.98×10^{26} Nm^{-1}) compared with that of GaP (1.2×10^{26} Nm^{-1}). The corresponding values of cross-section of damage formation at 15 K for InP and GaP are 6.41×10^{-14} cm^2 and 1.58×10^{-14} cm^2, respectively [115, 116].

A difference in activation energy, E_{act}, for the primary dynamic annealing process thought to be operating in InP versus GaP, could also be contributing to the greater reduction in η_{dpa} value of InP at 15K. The E_{act} describes the temperature dependence over the entire temperature range for a given material and given process, in this case, dynamic annealing. The data suggest that InP is more temperature dependent than GaP.

Figure 4-5 shows the P_a, A_s and the critical η_{dpa} values at 15 K as determined from the plots in Figure 4-4. At 300 K it was observed that stimulated amorphisation was the dominant process with P_a having a negligible role. However, in the case of 15 K, we observe that the amorphisation process is governed by both direct impact and stimulated amorphisation. The critical η_{dpa} values also confirm the trend observed in Figure 4-4 i.e. GaP is the most difficult to amorphise and InP the easiest. A similar trend at 20 K has been reported in $Al_xGa_{1-x}As$ [23].

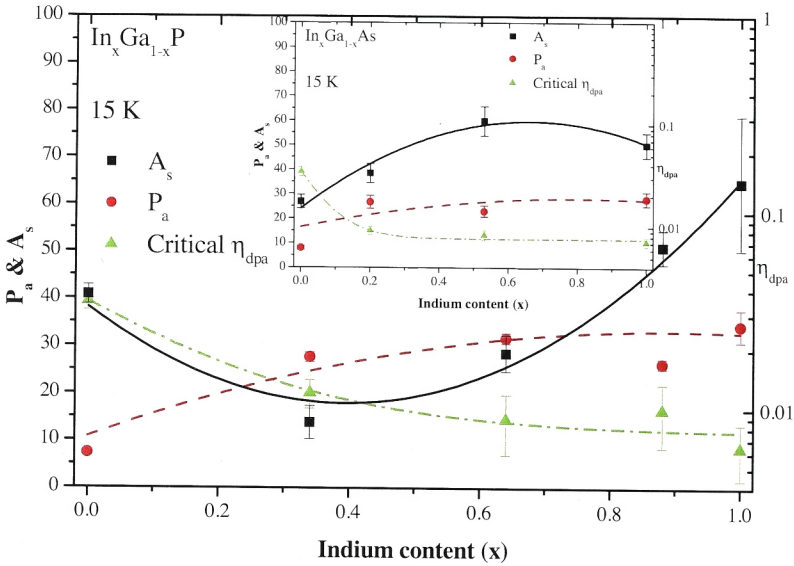

Figure 4-5 Critical η_{dpa} and probabilities of direct impact (P_a) and stimulated (A_s) amorphisation as a function of stoichiometry for $In_xGa_{1-x}P$ implanted at 15 K. Shown inset is Pa, As and critical η_{dpa} plot for $In_xGa_{1-x}As$ implanted at 15 K .

Shown inset in Figure 4-5 is the P_a, A_s and critical η_{dpa} plots for 15 K implantation in $In_xGa_{1-x}As$ using the data reported in Ref. [114]. Although the behaviour for A_s in $In_xGa_{1-x}As$ is opposite to that observed in $In_xGa_{1-x}P$, there is still a clear indication of contributions from both P_a and A_s to the amorphisation process. Moreover, the trend observed for critical η_{dpa} is similar to that observed for $In_xGa_{1-x}P$, with GaAs being the most difficult to amorphise and InAs the easiest.

4.3.2 EXAFS

In the previous section it has been shown that the 300 K amorphisation behaviour of $In_xGa_{1-x}P$ is very similar to that observed in $In_xGa_{1-x}As$ as outlined in Chapter 3. In Chapter 3 it was concluded that the structural disorder at the next nearest neighbour shell was correlated with the amorphisation behaviour observed in $In_xGa_{1-x}As$. The aim of this

section is to investigate if a similar trend is present in $In_xGa_{1-x}P$. EXAFS measurements were carried out at the In and Ga K edges for this purpose.

Figure 4-6 shows the non-phase-corrected Fourier-transformed EXAFS spectra of unimplanted InP, GaP and $In_{0.50}Ga_{0.50}P$ measured at the In K edge. A nearest neighbour (NN) peak is apparent for all samples at a non-phase-corrected radial distance of ~ 2.1 Å. This peak is due to scattering from the first shell P atoms. The ternary and binary alloys exhibit similar amplitudes because the NN shell for all samples is comprises of four P atoms.

In contrast, a marked difference in amplitude is observed in the next nearest neighbour peak (at ~ 3 – 4.5 Å) between the binary and ternary compounds, with $In_{0.50}Ga_{0.50}P$ having much reduced NNN amplitude compared with either InP or GaP. Whereas, for the binary compounds, the NNN shell consists of only In (for InP) and Ga (for GaP), the NNN shell for $In_{0.50}Ga_{0.50}P$ contains both In and Ga atoms. All NNN shells contain twelve atoms in total. The reduced NNN peak is characteristic of disordered material.

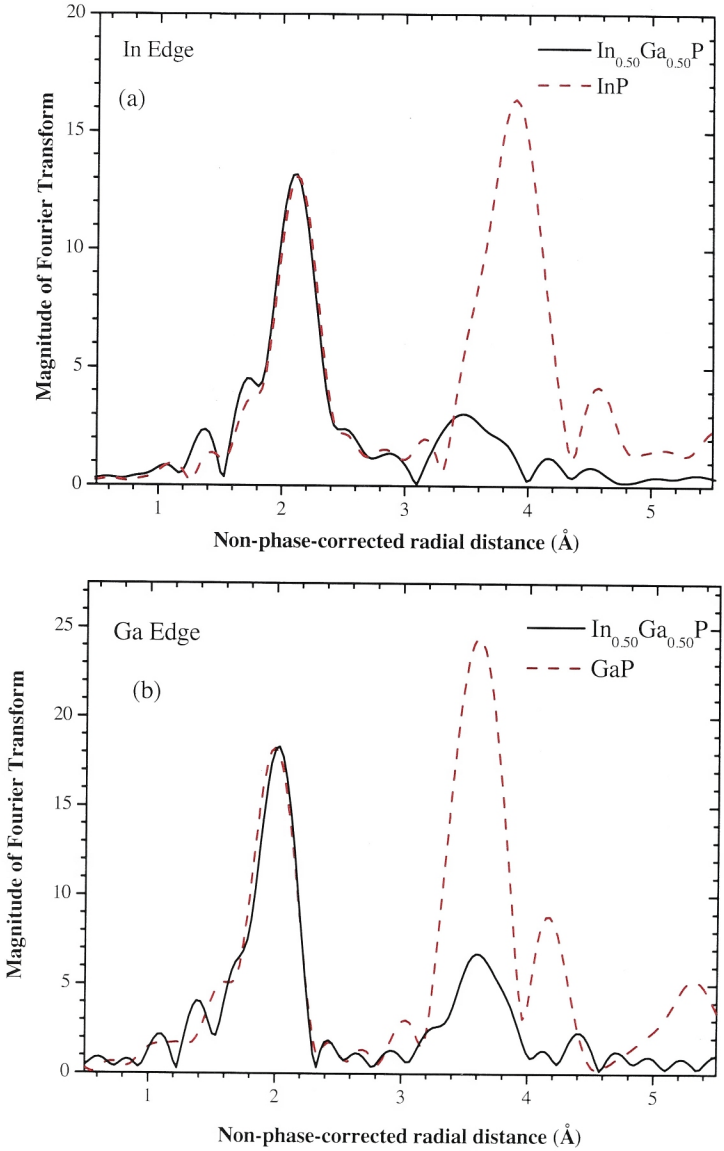

Figure 4-6 Fourier transform of EXAFS spectra for (a) crystalline InP and $In_{0.50}Ga_{0.50}P$ as measured at the In K edge and (b) crystalline GaP and $In_{0.50}Ga_{0.50}P$ measured at the Ga K edge.

ARTEMIS [63] was used to fit the EXAFS data as described previously in Section 4.2. The back transformed Ga K edge data and fits for GaP and $In_{0.50}Ga_{0.50}P$ are shown in Figure 4-7.

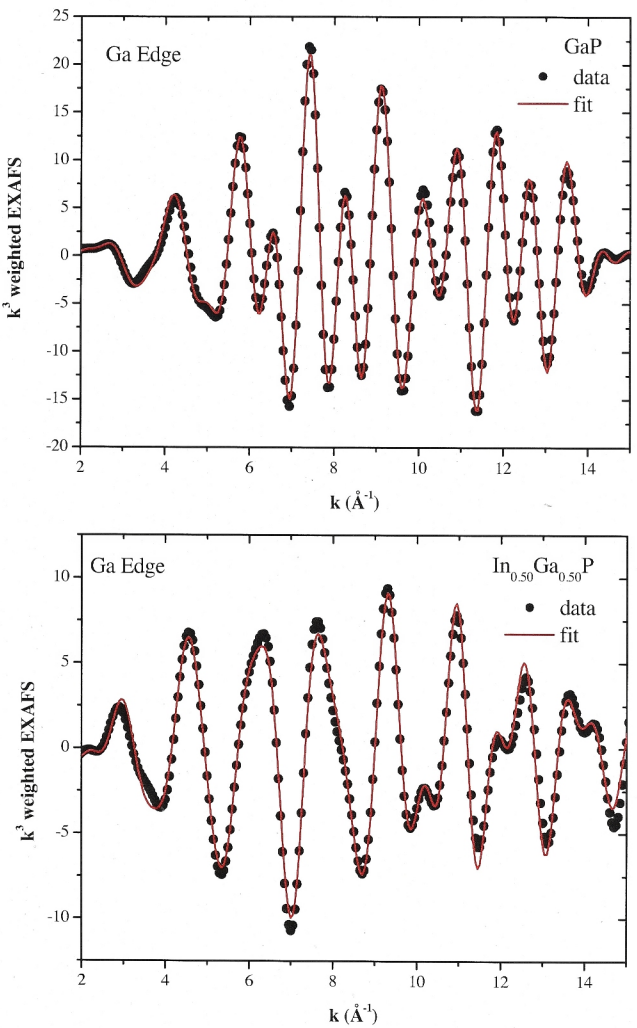

Figure 4-7 k^3-weighted back-transformed experimental data versus the photo-electron wave number k for measurements at the Ga K edge for (a) GaP and (b) for $In_{0.50}Ga_{0.50}P$.

Similar fits were performed for $In_{0.34}Ga_{0.66}P$ and $In_{0.66}Ga_{0.34}P$ at both the In and Ga K edges and for InP at the In edge. The resulting bond lengths, bond angles and DWF are listed in Table 3-1.

Material	Bond (NN/NNN)	Bond Length (Å)		Angle	θ°	DWF_{NNN} (In-P-In/Ga-P-Ga)
		NN	NNN			
GaP	Ga-P/Ga-Ga	2.35 ± 0.003	3.858 ± 0.004	Ga-P-Ga	110.3 ± 0.2	0.0041 ± 0.0003
$In_{0.34}Ga_{0.66}P$	In-P/In-In	2.506 ± 0.003	4.003 ± 0.018	In-P-In	106 ± 0.5	0.0068 ± 0.001
	Ga-P/Ga-Ga	2.359 ± 0.003	3.92 ± 0.011	Ga-P-Ga	112.4 ± 0.4	0.0061 ± 0.001
$In_{0.50}Ga_{0.50}P$	In-P/In-In	2.514 ± 0.003	4.041 ± 0.023	In-P-In	107 ± 0.6	0.008 ± 0.002
	Ga-P/Ga-Ga	2.374 ± 0.003	3.968 ± 0.013	Ga-P-Ga	113.4 ± 0.4	0.0066 ± 0.002
$In_{0.66}Ga_{0.34}P$	In-P/In-In	2.523 ± 0.002	4.1 ± 0.01	In-P-In	108.7 ± 0.3	0.0064 ± 0.001
	Ga-P/Ga-Ga	2.365 ± 0.003	3.99 ± 0.019	Ga-P-Ga	115 ± 0.6	0.0059 ± 0.002
InP	In-P/In-In	2.538 ± 0.003	4.157 ± 0.004	In-P-In	110 ± 0.2	0.0038 ± 0.0002

Table 4-1 Bond lengths, bond-angles and Debye Waller factors (DWF) calculated from EXAFS spectra of InP, GaP, and $In_xGa_{1-x}P$.

Figure 4-8 shows a schematic for $In_xGa_{1-x}P$ bond length and bond angles shown in Table 4-1. R_{InP} and R_{GaP} are the NN distances whereas the R_{GaGa} or R_{InIn} is the NNN distance. Bond length values given in Table 4-1 are in good agreement with the theoretical work of Cai and Thorpe [39] and the experimental work by [41, 100].

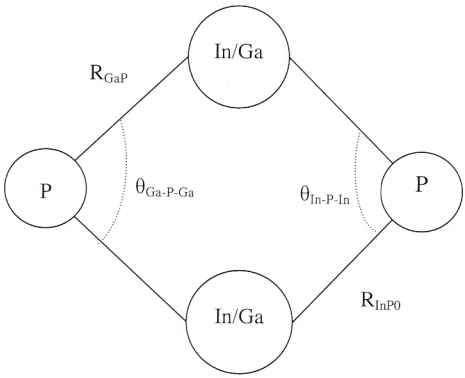

Figure 4-8 A schematic of bond length and bond angle for InGaP.

The NN bond lengths for In-P and Ga-P from Table 4-1 are plotted as a function of In content in Figure 4-9 along with the Vegard model where the alloy is characterised by one common bond length that varies as a function of stoichiometry. Clearly, a bimodal bond length distribution exists for both In-P and Ga-P with a linear dependence on stoichiometry that is much closer to their respective binary values than to the Vegard model.

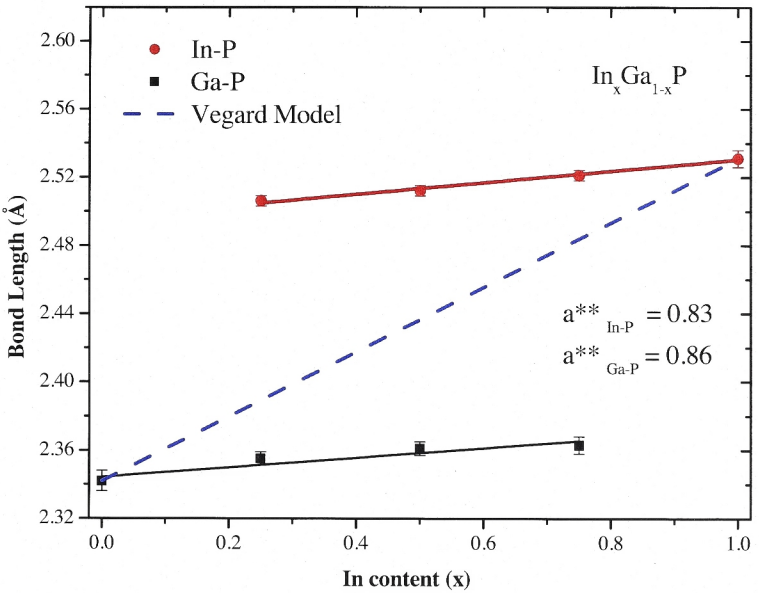

Figure 4-9 Nearest-neighbour bond lengths (In-P and Ga-P) for unimplanted $In_xGa_{1-x}P$ as a function of stoichiometry. The Vegard model is included for comparison.

The topological rigidity parameter (a**) (see Equation 3.2) calculated from the above plots was 0.83 ± 0.07 for In-P and 0.86 ± 0.07 for Ga-P bond length distribution in complete agreement with an average value of 0.8 reported previously [117]. This suggests that the structural disorder in $In_xGa_{1-x}P$ is concentrated primarily in the bond angle distributions.

Bond angles listed in Table 4-1 for InP and GaP agree very well with the tetrahedral value of 109.5° for zinc-blende structures. However, the bond angles for the ternaries deviate significantly from the tetrahedral value. The bond angles consist of two long In-P bonds in the case of In-P-In and thus have bond angles smaller than the tetrahedral

value. The opposite is true for Ga-P where the bonds in Ga-P-Ga are shorter and thus have bond angles larger than the tetrahedral value.

Figure 4-10 shows the DWF as a function of stoichiometry for the NNN shell about the In atom for In-P-In and about the Ga atom for Ga-P-Ga for $In_xGa_{1-x}P$. Structural disorder at the NNN shell in the ternary alloy is significantly greater than that of the two binaries with a maximum at x = ~ 0.5.

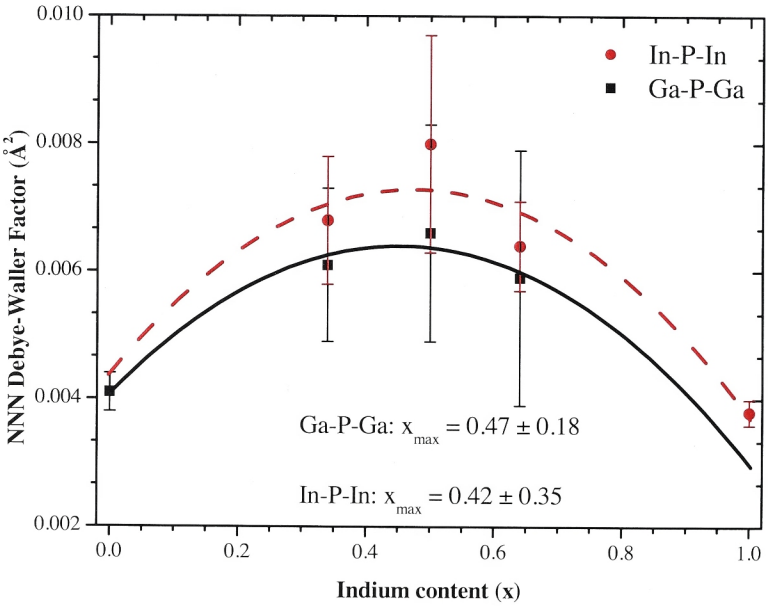

Figure 4-10 Debye-Waller factor for the next nearest neighbour in $In_xGa_{1-x}P$ as a function of stoichiometry.

Within the margins of experimental uncertainty, the maximum observed in structural disorder from EXAFS is well correlated with the maximum observed in stimulated amorphisation (A_s) and the minimum in critical η_{dpa} from RBS-C. That is, the stoichiometry that requires the least amount of η_{dpa} to render it amorphous is the one that

exhibits the maximum structural disorder and has the highest probability of stimulated amorphisation.

The change in bond angle with stoichiometry demonstrates that lattice mismatch in these ternary alloys is accommodated by both adjustments in bond length and bond angle. However, as demonstrated by the topological rigidity parameter (a**), distortion in bond angle distribution is far greater than that in bond length distribution.

This suggests that the structural disorder in these ternary alloys, concentrated primarily in the bond angle distributions, gives rise to preferential sites for stimulated amorphisation rendering $In_xGa_{1-x}P$ amorphous at η_{dpa} values less than those required for both InP and GaP.

4.4 Conclusion

The kinetics of the ion-implantation-induced amorphisation of $In_xGa_{1-x}P$ have been determined with RBS-C over the entire stoichiometry range at temperatures of 300 K and 15 K.

At 300 K, all stoichiometries for the ternary alloy were rendered amorphous at η_{dpa} values lower than those required for either of the two binary extremes. The crystalline-to-amorphous phase transformation was dominated by a stimulated amorphisation process, the probability for which was maximum at the stoichiometry most easily amorphised. EXAFS measurements demonstrated the bimodal bond length distribution characteristic of $In_xGa_{1-x}P$ was primarily accommodated on the zinc-blende lattice via bond bending with deviations from the tetrahedral bond angle readily apparent in the

ternary alloy. Correlating EXAFS and RBS-C measurements, structural disorder and the probability of stimulated amorphisation were both greatest at a common intermediate stoichiometry, where the ternary alloy was most easily amorphised. These results are similar to those observed in $In_xGa_{1-x}As$, suggesting a similar amorphisation mechanism is in place i.e. the anomalous amorphisation is a result of structural disorder. The bimodal bond length distribution in $In_xGa_{1-x}P$ leads to an increased NNN DWF that is largely accommodated in the bond angle distribution given bond bending is energetically favoured over bond stretching. It is this structural disorder that serves as preferential nucleation sites for amorphous phase formation.

At 15 K, however, the amorphisation behaviour of $In_xGa_{1-x}P$ for all stoichiometries studied was intermediate to the two binary extremes, with GaP requiring the highest and InP requiring the least amount of η_{dpa}. At 15 K both direct impact and stimulated amorphisation have significant contributions to the amorphisation process. In general, the critical η_{dpa} required to amorphise GaP and $In_xGa_{1-x}P$ was a factor of two less at 15 K than that required at 300 K. However, the critical η_{dpa} required to amorphise InP at 15 K was six times less than that required at 300 K. It is suggested that the greater reduction in the η_{dpa} value of InP at 15 K was due to the lower force constant observed in InP compared with that of GaP at these low temperatures.

The next chapter will investigate if a similar amorphisation mechanism as has been observed in $In_xGa_{1-x}As$ and $In_xGa_{1-x}P$ at 300 K is present in $Si_{1-x}Ge_x$ alloys.

Chapter 5 $Si_{1-x}Ge_x$

5.1 Introduction

In Chapter 3 the amorphisation of $In_xGa_{1-x}As$ was investigated, and the observed behaviour was attributed to existing structural disorder present in the material as a result of bond bending to accommodate the bimodal bond length distribution. This disorder serves as preferential nucleation sites for stimulated amorphisation. Having established the reason for the anomalous amorphisation, Chapter 4 investigated whether this applied to a similar material, $In_xGa_{1-x}P$, which also has a bimodal bond length distribution. It was found that $In_xGa_{1-x}P$ behaved in a similar way to $In_xGa_{1-x}As$.

In this chapter, we now extend the study to $Si_{1-x}Ge_x$, which has also been shown to have a composition dependent bond length not following the VCA [42, 118]. Three distinct bond lengths have been observed in $Si_{1-x}Ge_x$: Ge-Ge, Ge-Si and Si-Si. Whereas the previous two materials were III-Vs and had a zinc-blende structure, $Si_{1-x}Ge_x$ is a IV-IV material and has a diamond structure. Hence, if a multimodal/composition dependent bond length is the only factor influencing the amorphisation behaviour observed in the previous two chapters, we should expect $Si_{1-x}Ge_x$ to follow similar amorphisation kinetics. In this chapter the crystalline to amorphous phase transformation of $Si_{1-x}Ge_x$ alloys is reported and the resulting data fit using the Hecking model for defect accumulation and amorphisation [22].

Haynes *et al.* [119, 120] studied the amorphisation of $Si_{1-x}Ge_x$ as a function of fluence and temperature. They implanted $Si_{1-x}Ge_x$ layers with a fixed ion fluence of 6×10^{14} cm^{-2}

Si ions at temperature ranging between -100 and 150 °C. Although they did observe increased damage with increasing Ge content for a given fluence, a full crystalline to amorphous phase transformation was not reported. Similarly, Larsen *et al.* [121] and Linder *et al.* [122] also reported on $Si_{1-x}Ge_x$ amorphisation. They used 2 MeV Si ions at room temperature but they did not include Si and Ge in their data to compare with $Si_{1-x}Ge_x$ amorphisation. Linder *et al.* found that for a fixed ion fluence the damage produced in $Si_{1-x}Ge_x$ increased with increasing x i.e. samples with higher Ge content were easier to amorphise. Larsen *et al.* reported similar results noting an enhanced level of damage and a strong decrease in critical ion fluence required for the formation of a buried amorphous layer in $Si_{1-x}Ge_x$.

Lie *et al.* [123] carried out a comparative study of amorphisation behaviour in strained versus relaxed layers of $Si_{0.90}Ge_{0.10}$ and found that the two layers behaved in a similar manner and that the presence of strain did not affect the irradiation induced damage in $Si_{0.90}Ge_{0.10}$. Lie [124] later wrote a comprehensive review of ion implantation in $Si_{1-x}Ge_x$ alloys and reported data for the entire range of $Si_{1-x}Ge_x$ along with Si and Ge.

Decoster and Vantomme [125] studied the ion implantation induced damage in Ge as a function of ion fluence, mass, energy and current density and proposed three regions for the damage accumulation process. In the lowest fluence region, the strain and defect fraction was found to be linearly proportional to ion fluence and the defect density was directly proportional to the deposited energy which is converted into the creation of vacancies. The damage accumulation process in the second region was found to be more efficient as a result of increased defect density in the implanted layer. The third region

was found to start at the critical fluence for amorphisation, and this value was determined for a wide range of ion masses and energies.

Composition dependent bond lengths in crystalline $Si_{1-x}Ge_x$ have been reported by various authors [42, 118, 126, 127]. Kajiyama *et al.* [127] reported $Si_{1-x}Ge_x$ as having a Bragg-Pauling type bond behaviour i.e. the bond length in $Si_{1-x}Ge_x$ was independent of composition, in contrast to the theoretical predictions of Cai and Thorpe [83]. Later, Mousseau and Thorpe [128] attributed the difference between these theoretical and experimental results to hydrogen contamination of the $Si_{1-x}Ge_x$ samples of Kajiyama *et al.* Ridgway *et al.* [42] and Aldrich *et al.* [126] gave bond lengths for Ge-Ge and Ge-Si bond lengths measured at the Ge K edge. Ridgway *et al.* reported on an increased bond length as a function of Ge composition in $Si_{1-x}Ge_x$. Aubry *et al.* [118] performed EXAFS measurements at both the Si and Ge K edge in their study. They confirmed experimentally that the first nearest neighbour (NN) bond lengths of $Si_{1-x}Ge_x$ alloy including Si-Si, Ge-Si and Ge-Ge bonds maintain distinctly different bond lengths as predicted by the Valence force field based models. They also determined the topological rigidity parameter $a^{**} = 0.63$ for $Si_{1-x}Ge_x$.

In this chapter, Ge K edge EXAFS data were used to determine the NN and the next nearest neighbour (NNN) bond lengths and these bond lengths then used to calculate the $Si_{1-x}Ge_x$ bond angles. The Debye-Waller factor (DWF) at the NNN was also determined from the EXAFS data.

5.2 Experimental

$Si_{1-x}Ge_x$ layers with $0.04 \leq x \leq 1$ were grown using molecular beam epitaxy (MBE) on Si and Si-on-insulator substrates[2] at 600 ° C. These samples were provided by collaborators (J. L. Hansen and A. N. Larsen) from Aarhus University in Aarhus, Denmark. Samples were annealed at temperatures $\leq$ 900 ° C both in-situ and ex-situ to relieve residual strain through dislocation formation. Layers grown on Si-on-insulator substrates were used for EXAFS measurements. Stoichiometries of these layers were determined using RBS as outlined in section 2.2.

Samples with x = 0.04, 0.2, 0.46 and 0.66 were implanted using ^{74}Ge ions at the Friedrich-Schiller-Universität in Jena, Germany. RBS-C measurements on these samples were performed to quantify the ion implanted disorder. Nominally undoped Si and Ge samples were implanted using ^{74}Ge ions at the ion implanter facility at ANU. The implanted energy was varied between 200 and 300 keV to obtain comparable depth of ^{74}Ge ions in all samples. Samples with x = 0.04 were also implanted and measured in Canberra to enable a calibration between implants performed in Jena and Canberra. A difference in dosimetry was apparent, and is detailed in the next section.

RBS-C measurements were performed as described in Chapter 3, section 3.2 to determine $\Delta\chi_{min}$. The backscattered ion yield in the case of $Si_{1-x}Ge_x$ was integrated over a depth range of typically 200 – 1500 Å, at which depth the implantation-induced vacancy production (determined from SRIM 2003 [17]) decreased to two-thirds of the maximum value. Figure 5-1 shows RBS-C spectra of $Si_{0.80}Ge_{0.20}$ as a function of fluence showing scattering from Ge. Here an increase in fluence results in an increase in backscattering

[2] 0.2 μm Si/0.4 μm SiO_2/Si substrate

yield, which is indicative of increased disorder in these materials. The conversion from backscattered ion energy to depth was performed using the DICADA program [48].

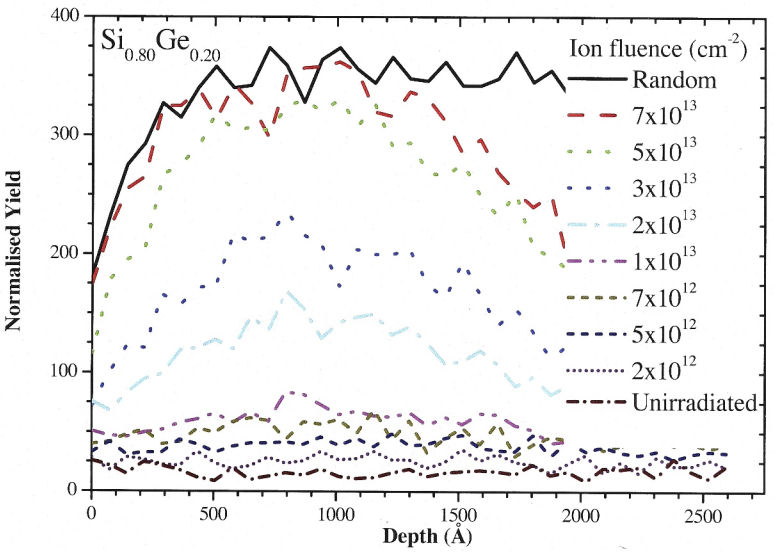

Figure 5-1 RBS-C spectra of $Si_{0.80}Ge_{0.20}$ irradiated at 300 K.

EXAFS measurements were performed in transmission mode at the Ge K edge using beamline 20-B at the Photon Factory in Japan at a temperature of 10 K. Prior to the EXAFS measurements, the MBE layers were separated from the substrate by preferentially dissolving the SiO_2 layer using a 1:2 HF:H_2O solution as described by Ridgway *et al.* [42, 129]. ARTEMIS [63, 64] was used to determine the structural parameters over a photo-electron wavenumber (k) range of 3.8 – 15.2 and a non-phase-corrected radial distance (r) range of 1.3 – 4 Å. For each sample, the coordination number for the NN shell was set to a total of four and reflected the stoichiometric ratio of Si and Ge found in that sample. Similarly, for the NNN shell, the coordination

number was set to 12, and again reflected the stoichiometric ratio in the material. Bond lengths for the NN and NNN were used to determine the bond angles, in a similar manner to previous chapters.

5.3 Results and Discussion

5.3.1 RBS-C

To check for any difference in dosimetry between the implants performed in Jena and in Canberra, $Si_{0.96}Ge_{0.04}$ was implanted using the same energy, and subsequently measured using RBS-C under similar conditions, at both facilities. The resulting $\Delta\chi_{min}$ data and Hecking model [22, 25] fits are shown in Figure 5-2 where a clear offset (a factor of ~ 1.65) is observed.

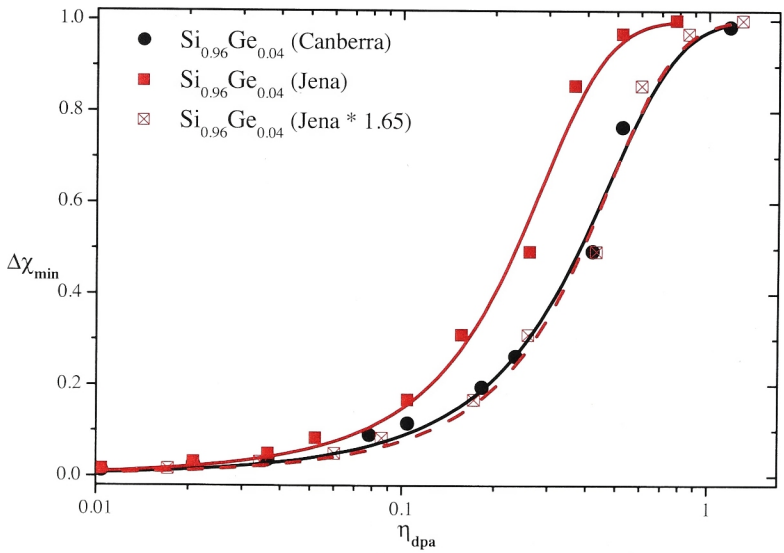

Figure 5-2 $\Delta\chi_{min}$ as a function of number of displacements per atom comparing difference in dosimetry for $Si_{0.96}Ge_{0.04}$ implanted and measured under similar conditions in Jena and in Canberra.

The parameters (P_a, A_s and critical η_{dpa}) determined from the Hecking model fits for the Canberra and Jena data are shown in Table 5-1. Included also in Table 5-1 are the parameters determined from the fit of the adjusted data.

	P_a	A_s	Critical η_{dpa}
$Si_{0.96}Ge_{0.04}$ (Canberra)	0.73 ± 0.13	5.05 ± 0.8	0.33 ± 0.08
$Si_{0.96}Ge_{0.04}$ (Jena)	1.01 ± 0.19	9.28 ± 1.24	0.22 ± 0.05
$Si_{0.96}Ge_{0.04}$ Jena*1.65	0.67 ± 0.12	5.62 ± 0.75	0.36 ± 0.08

Table 5-1 Pa, As and critical ηdpa values for $Si_{0.96}Ge_{0.04}$

Due to the difference in dosimetry the unadjusted values for $Si_{0.96}Ge_{0.04}$ (Jena) are different to those of $Si_{0.96}Ge_{0.04}$ (Canberra). However, the adjusted values for these parameters are the same for both measured in Canberra and in Jena. All $Si_{1-x}Ge_x$ samples implanted in Jena (and discussed from here onwards) were scaled to reflect the above difference in dosimetry so that a meaningful comparison could be made for the entire stoichiometry range.

The presence of misfit dislocations, and their effect on the amorphisation kinetics of the alloy, needed to be considered for $Si_{1-x}Ge_x$ just as they were for $In_xGa_{1-x}As$ (see Chapter 3). Ion implantation for Si and Ge was performed on bulk substrate materials free from misfit dislocations whereas amorphisation studies on $Si_{1-x}Ge_x$ were performed on materials grown (beyond the critical thickness) on Si substrates which, due to the lattice mismatch, have misfit dislocations present in them.

To study the worst case scenario, a Ge layer was grown on a Si substrate. Both Ge on Si (Ge/Si) and Ge were implanted simultaneously with 300 keV Ge ions at 300 K. The resulting damage was measured using RBS-C and $\Delta\chi_{min}$ as a function of η_{dpa} plotted is shown in Figure 5-3.

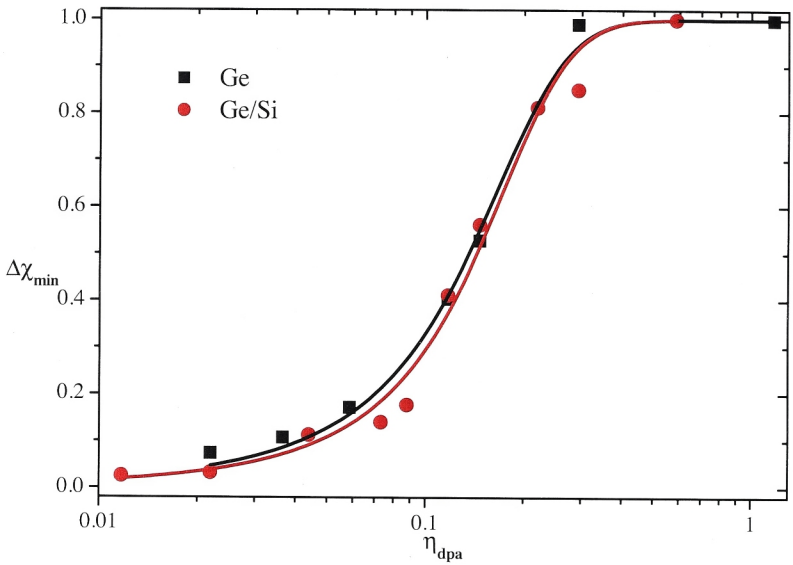

Figure 5-3 $\Delta\chi_{min}$ as a function of number of displacements per atom comparing amorphisation kinetics of bulk Ge and Ge/Si with 300 keV Ge ions at 300 K.

Both Ge and Ge/Si have near identical amorphisation behaviour and equal values of P_a, A_s and critical η_{dpa} (Table 5-2) were determined from the Hecking fits of Figure 5-3. This clearly indicates that the presence of misfit dislocations did not influence the amorphisation kinetics of Ge, and hence would not influence amorphisation of $Si_{1-x}Ge_x$ alloys which is expected to have a lower misfit density than Ge on Si.

	P_a	A_s	Critical η_{dpa}
Ge	1.85 ± 0.36	15.35 ± 2.57	0.12 ± 0.03
Ge/Si	1.53 ± 0.39	16.09 ± 2.94	0.14 ± 0.04

Table 5-2 P_a, A_s and critical η_{dpa} values for Ge and Ge/Si

Figure 5-4 shows the fits for $\Delta\chi_{min}$ as a function of η_{dpa} over the entire stoichiometry range for $Si_{1-x}Ge_x$. It is clear that Si is the most difficult to amorphise, and that the critical value of η_{dpa} required for amorphisation decreases with increasing Ge content, with Ge being the easiest to amorphise. The amorphisation behaviour of $Si_{1-x}Ge_x$ is similar to that observed in $Al_xGa_{1-x}As$ [9] and discussed in earlier chapters where the η_{dpa} required to amorphise $Al_xGa_{1-x}As$ increased with increasing Al content. This is contrary to the amorphisation behaviour observed in $In_xGa_{1-x}As$ and $In_xGa_{1-x}P$, as outlined in Chapters 3 and 4 respectively.

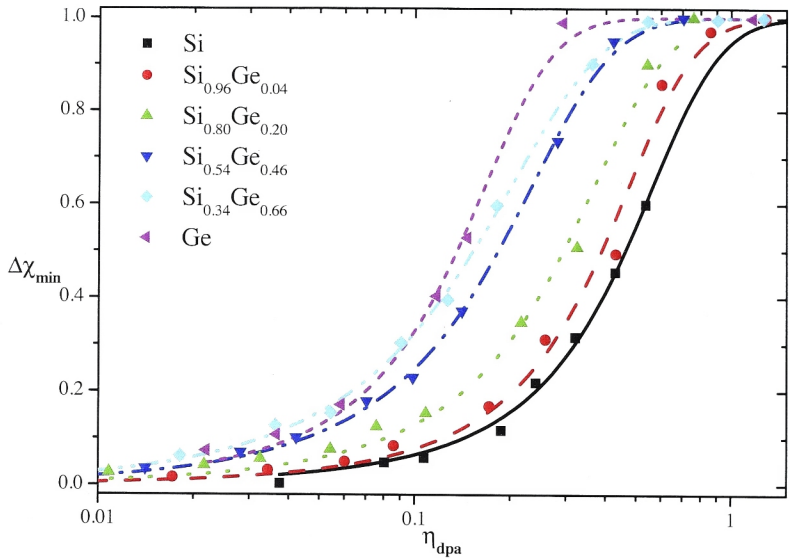

Figure 5-4 $\Delta\chi_{min}$ as a function of η_{dpa} measured over the entire stoichiometry range x for $Si_{1-x}Ge_x$. The plotted curves are fits using the Hecking model to the experimental data points.

Values of P_a, A_s and critical η_{dpa} derived from the data are plotted as a function of Ge content in Figure 5-5. In contrast with $In_xGa_{1-x}As$ and $In_xGa_{1-x}P$, $Si_{1-x}Ge_x$ does not exhibit a quadratic behaviour for A_s or critical η_{dpa} where an intermediate stoichiometry was the easiest to amorphise. However, the probability for stimulated amorphisation (A_s) is still the dominant factor as compared with the probability of direct impact amorphisation (P_a). Ge, which is easiest to amorphise has the lowest critical η_{dpa}, and the highest value for A_s. This correlation is the same as observed in both $In_xGa_{1-x}As$ and $In_xGa_{1-x}P$.

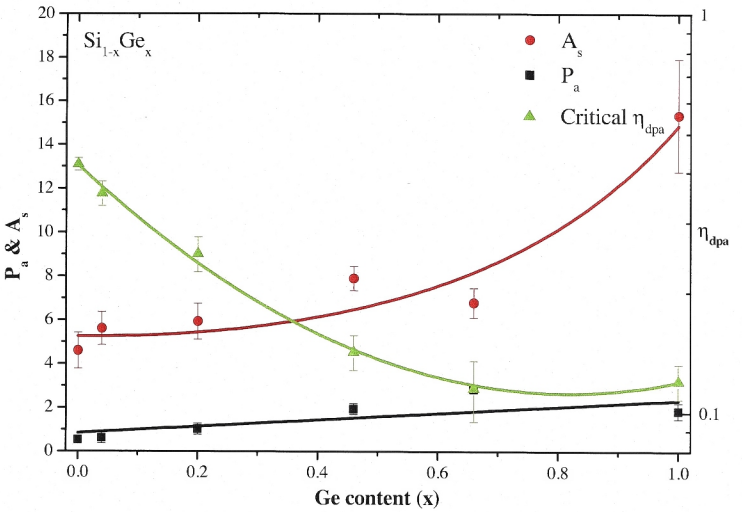

Figure 5-5 Critical η_{dpa} and probabilities for direct impact (P_a) and stimulated amorphisation (A_s) as a function of stoichiometry for $Si_{1-x}Ge_x$.

A similar trend for $Si_{1-x}Ge_x$ amorphisation was reported by Lie [124] using 100 – 300 keV Si ions. All data presented in reference [124] were from pseudomorphically strained $Si_{1-x}Ge_x$ layers, however, as shown by Lie *et al.* [123] the presence of pseudomorphic strain had no significant effect on the resulting implantation induced disorder in these materials.

To compare the results of this study to that of reference [124], their data were converted to η_{dpa} values and the resulting $\Delta\chi_{min}$, P_a and A_s, and critical η_{dpa} plots are shown in Figure 5-6 and Figure 5-7, respectively. The amorphisation trends of this study and those shown by Lie are similar.

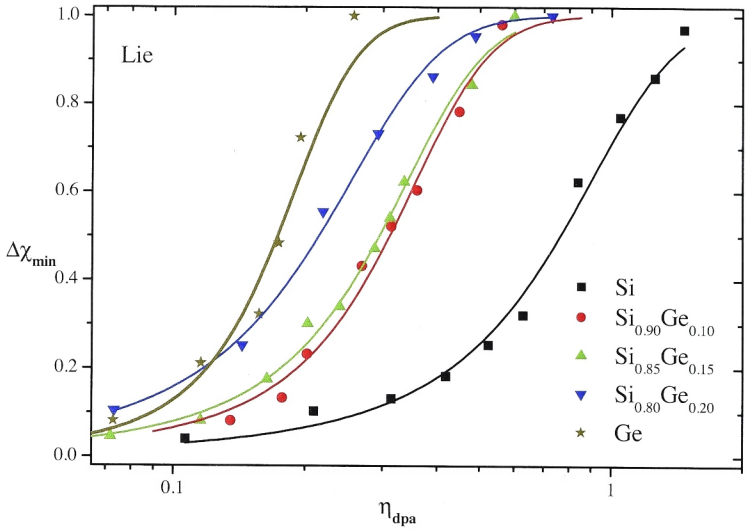

Figure 5-6 $\Delta\chi_{min}$ vs. η_{dpa} plots of Lie data from reference [124].

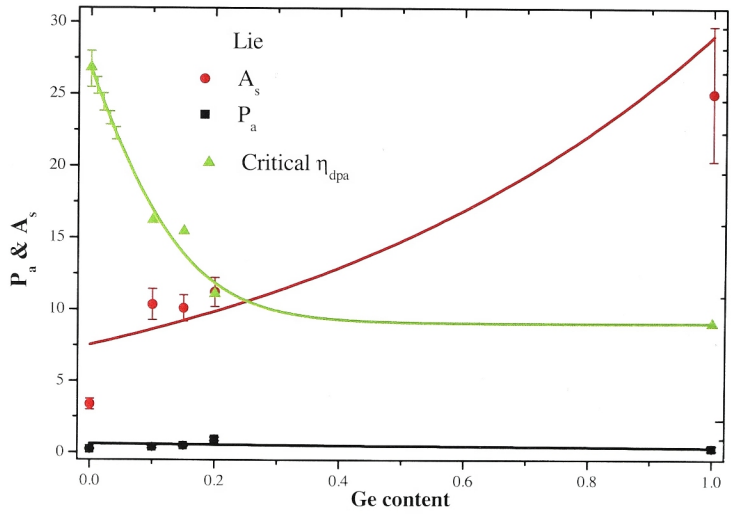

Figure 5-7 Critical η_{dpa}, P_a and A_s determined from Hecking fits to Lie data from reference [124].

Higher values of A_s and consequently of critical η_{dpa} in reference [124] are possibly as a result of Si ions being used in reference [124] as compared to Ge in this study. Although it is expected that η_{dpa} should normalise the effect of ion mass, however, exceptions do occur. A similar trend has been reported by Wendler [16] in GaAs, where despite equal η_{dpa} values, the ion mass clearly influenced damage production. Further study needs to be performed to determine this discrepancy in data observed for $Si_{1-x}Ge_x$ between data presented in this study and that of Lie for amorphisation due to heavier and lighter ions.

5.3.2 EXAFS

EXAFS was utilised to probe the short-range order about Ge atoms in the $Si_{1-x}Ge_x$ samples to gain an understanding of why the amorphisation process in $Si_{1-x}Ge_x$ is different from that in $In_xGa_{1-x}As$ and $In_xGa_{1-x}P$.

Figure 5-8 shows Fourier-transformed EXAFS spectra of unimplanted $Si_{1-x}Ge_x$ and Ge measured at the Ge K edge. A NN and NNN peak is apparent in all spectra at a non-phase-corrected radial distance of ~ 2.1 and 3.7 Å, respectively. The NN and NNN shells for Ge consist of four and 12 Ge atoms, respectively, whereas in $Si_{1-x}Ge_x$ the NN shell is a mix of both Si and Ge atoms (four and 12 in total, respectively). The highest NN and NNN amplitudes are observed for pure Ge. A reduction in amplitude with decreasing Ge content is clearly evident as a direct result of the atomic number (Z) dependence of the scattering strength of the Si and Ge atoms. The DWF for $Si_{1-x}Ge_x$ (shown later in Table 5-3) is much lower compared with both $In_xGa_{1-x}As$ and $In_xGa_{1-x}P$, and as a result, is not expected to account for the observed reduction in amplitude for NNN.

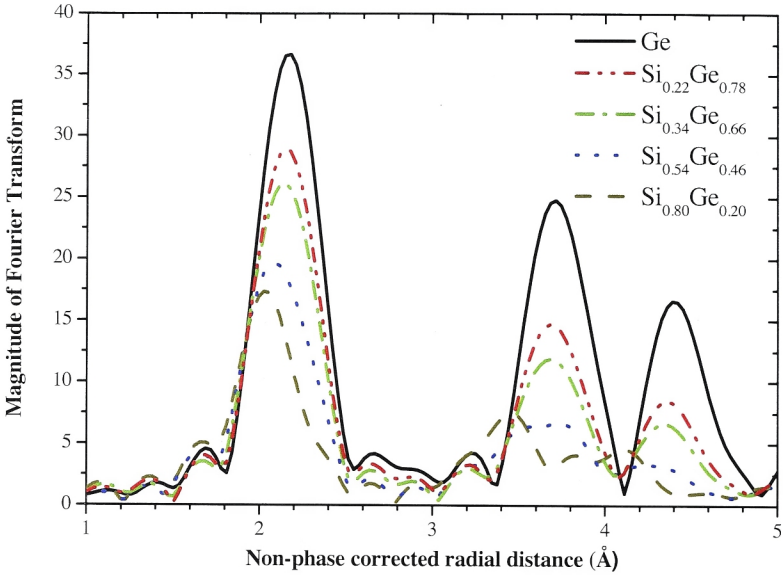

Figure 5-8 Fourier transform of EXAFS spectra measured at the Ge K edge for $Si_{1-x}Ge_x$.

The reduced amplitude of the NNN peak that we saw in $In_xGa_{1-x}As$ and $In_xGa_{1-x}P$ is not present in $Si_{1-x}Ge_x$. The reduction in amplitude of the NNN peak in $Si_{1-x}Ge_x$ is instead similar to that observed in $Al_{0.50}Ga_{0.50}As$. In general, a gradual reduction in the amplitude of the NNN peak, similar to that of the NN peak, is observed in $Si_{1-x}Ge_x$, as a result of decreasing Ge content due to the Z dependence.

Figure 5-9 shows fits to the EXAFS data for crystalline Ge and $Ge_{0.54}Si_{0.46}$ using ARTEMIS [63] with parameters defined earlier in section 3.2. The fits are in excellent agreement with the back transformed experimental data.

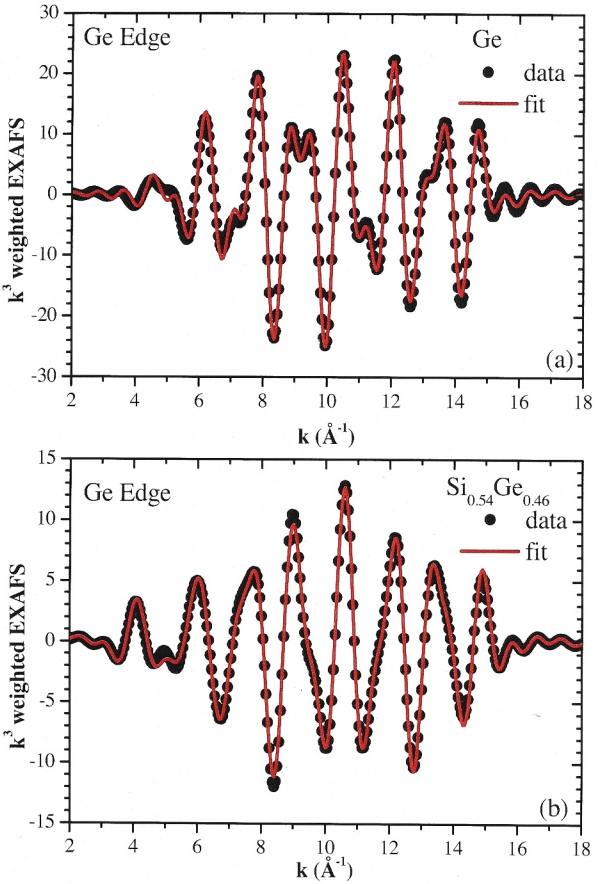

Figure 5-9 Best fit for Ge and $Si_{0.54}Ge_{0.46}$ at the Ge K edge to k^3 weighted experimental data using ARTEMIS.

Similar fits were performed for other stoichiometries and the bond lengths and DWF for the NN and NNN determined from these fits. The NN and NNN bond lengths were then used to determine the average bond angle between NNN and the absorbing atom using Eq. 3.3. These values are listed in Table 5-3.

Material	Bond Length (Å)				Bond Angle (θ°)		DWF_{NNN} (Ge-Ge-Ge)
	NN		NNN				
	R_{Ge-Ge}	R_{Ge-Si}	R_{Ge-Ge}	R_{Ge-Si}	Ge-Ge-Ge	Ge-Si-Ge	
$Si_{0.96}Ge_{0.04}$	--	2.383 ± 0.002	--	3.874 ± 0.006	--	--	0.0044 ± 0.0011
$Si_{0.80}Ge_{0.20}$	2.424 ± 0.006	2.391 ± 0.003	3.887 ± 0.058	3.895 ± 0.009	106.6 ± 1.67	108.75 ± 1.63	0.004 ± 0.0018
$Si_{0.54}Ge_{0.46}$	2.432 ± 0.002	2.392 ± 0.004	3.922 ± 0.004	3.938 ± 0.006	107.48 ± 0.17	110.13 ± 0.28	0.0039 ± 0.0003
$Si_{0.34}Ge_{0.66}$	2.438 ± 0.001	2.388 ± 0.008	3.958 ± 0.002	3.974 ± 0.017	108.53 ± 0.09	111.94 ± 0.53	0.0046 ± 0.0003
$Si_{0.22}Ge_{0.78}$	2.442 ± 0.001	2.404 ± 0.014	3.975 ± 0.004	3.989 ± 0.058	108.95 ± 0.13	111.53 ± 0.93	0.0049 ± 0.0004
Ge	2.447 ± 0.001	--	4.005 ± 0.003	--	109.84 ± 0.09	--	0.0039 ± 0.0002

Table 5-3 Bond lengths, bond-angles and Debye Waller factors (DWF) calculated from EXAFS spectra of InAs, GaAs, $Al_{0.50}Ga_{0.50}As$ and $In_xGa_{1-x}As$.

NN and NNN bond lengths in Table 5-3 are in good agreement with the theoretical values reported by Mousseau and Thorpe [130] and the experimental results for NN of Ridgway *et al.* [42] and Aubry *et al.* [118]. The theoretical model of Mousseau and Thorpe suggests an increase in bond lengths for NN Si-Si, Ge-Ge and Ge-Si with increasing Ge content. In addition, they also predict an increase in the NNN distance for Ge-Ge, Ge-Si and Si-Si bond lengths. Bond length for NNN Ge from Table 5-3 is also in good agreement with the experimental results shown for bulk Ge by Araujo *et al.* [131] and Sun *et al.* [132].

Note that the bond angles reported in Table 5-3 for the $Si_{1-x}Ge_x$ alloy do not deviate as significantly from the tetrahedral bond angle as was the case for $In_xGa_{1-x}As$ (Table 3-1) and $In_xGa_{1-x}P$ (Table 4-1). This indicates that the disorder at the NNN in $Si_{1-x}Ge_x$ should be less than that observed in $In_xGa_{1-x}As$ and $In_xGa_{1-x}P$.

The NN bond lengths for $Si_{1-x}Ge_x$ are plotted in Figure 5-10. Note that data shown in this plot for the Si-Si bond-length are taken from the work of Aubry *et al.* [118] and were acquired at RT as opposed to 10 K for Ge-Ge and Ge-Si data. Nonetheless, the values of a** calculated from Figure 5-10 for Ge-Ge (0.68 ± 0.03) and Ge-Si (0.76 ± 0.09) agree well with those reported by Aubury *et al.* for their RT data.

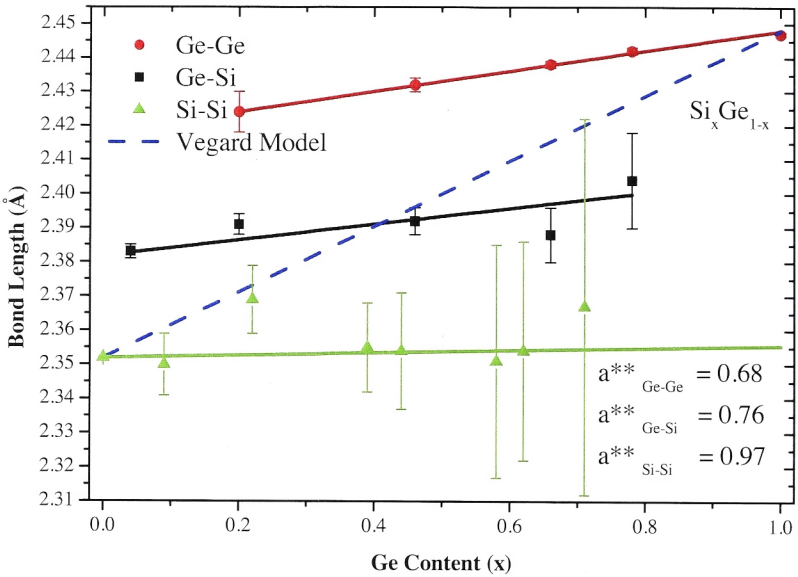

Figure 5-10 Nearest neighbour bond lengths (Ge-Ge, Ge-Si and Si-Si) for unimplanted $Si_{1-x}Ge_x$ as a function of stoichiometry.

From Figure 5-10, $Si_{1-x}Ge_x$ has a trimodal bond-length distribution consisting of Ge-Ge, Ge-Si and Si-Si bond lengths as opposed to $In_xGa_{1-x}As$ and $In_xGa_{1-x}P$ which have bimodal bond-length distributions. The Si-Si bond-length in $Si_{1-x}Ge_x$ does not change with changing composition and remains close to the Si-Si bond-length observed in pure Si. This also suggests that the increased Ge content in $Si_{1-x}Ge_x$ is primarily accommodated via bond bending as opposed to bond stretching in Si-Si, thus resulting in a value of a** for Si-Si (0.97 ± 0.14) very close to one, which represents the Bragg-Pauling condition of only bond bending being active. Similar values of a** for $Si_{1-x}Ge_x$ have previously been reported by Aldrich *et al.* [126].

At first the 'Z-plot' in Figure 5-10 seems similar to that for $In_xGa_{1-x}As$ (Figure 3-15) and $In_xGa_{1-x}P$ (Figure 4-9). However, when plotted on the same scale (Figure 5-11), it is evident that although the Z-plots of $In_xGa_{1-x}As$ and $In_xGa_{1-x}P$ are similar, the difference between the R_{GeGe}, R_{GeSi} and R_{SiSi} bond length in $Si_{1-x}Ge_x$ is much less than the difference between R_{InAs} (R_{InP}) and R_{GaAs} (R_{GaP}) bond lengths. The data for the Z-plot of $Al_xGa_{1-x}As$ were calculated from the theoretical predictions of Cai and Thorpe [39] and appear to be almost a straight line when plotted on this scale.

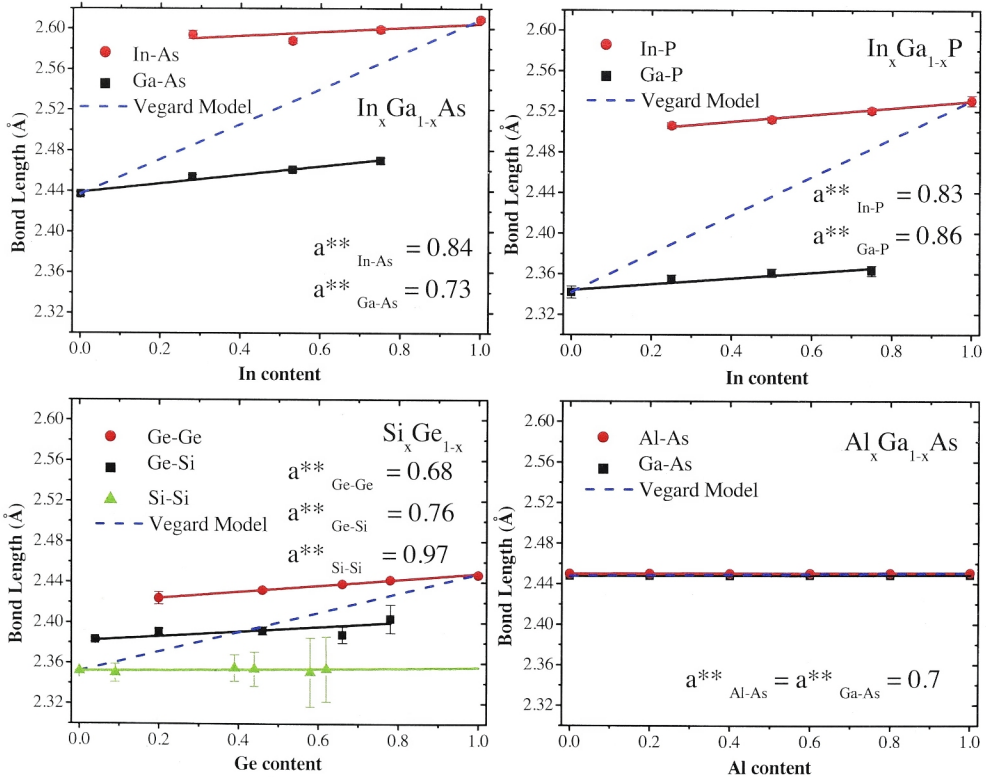

Figure 5-11 Nearest-neighbour bond lengths for $In_xGa_{1-x}As$, $In_xGa_{1-x}P$, $Si_{1-x}Ge_x$ and $Al_xGa_{1-x}As$.

The DWFs for the NNN shell of $In_xGa_{1-x}As$, $In_xGa_{1-x}P$ and $Si_{1-x}Ge_x$ are shown in Figure 5-12. It is evident that the disorder observed in $In_xGa_{1-x}As$ and $In_xGa_{1-x}P$ at the NNN is much reduced in $Si_{1-x}Ge_x$ and effectively independent of Ge content. One reason for this could be that in the $Si_{1-x}Ge_x$ system both Si and Ge are completely miscible and do not have separate anion and cation sublattices.

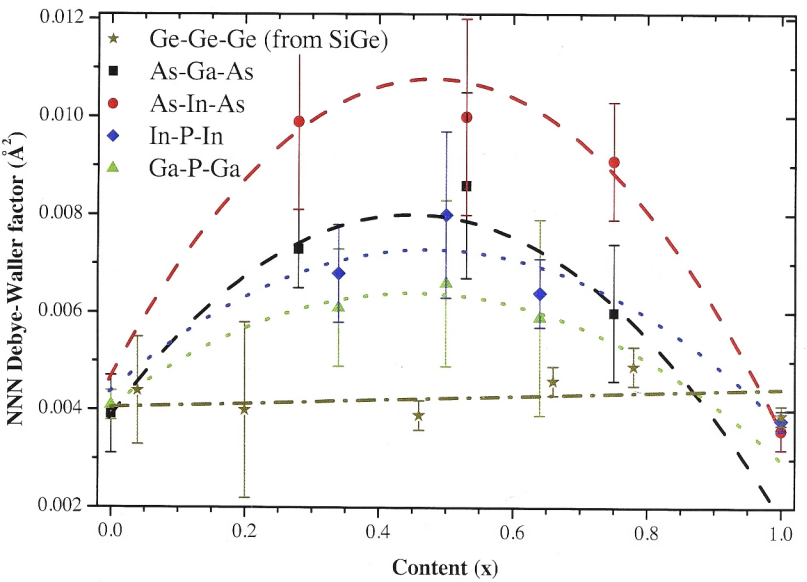

Figure 5-12 Debye-Waller factor of the NNN for $Si_{1-x}Ge_x$ about a Ge atom as a function of Ge content x. For comparison, Debye-Waller factor for $In_xGa_{1-x}As$ and $In_xGa_{1-x}P$ are also shown.

Correlating the EXAFS and RBS-C measurements, the fact that the $Si_{1-x}Ge_x$ amorphisation kinetics are more like $Al_xGa_{1-x}As$ as opposed to those of $In_xGa_{1-x}As$ or $In_xGa_{1-x}P$, is attributed to less bond angle distortion at the NNN in $Si_{1-x}Ge_x$. The amorphisation kinetics, however, are still dominated by the probability for stimulated amorphisation as opposed to the probability for direct impact amorphisation as shown in

Figure 5-7. Due to the lack of disorder at the NNN, a maximum A_s (or minimum critical η_{dpa}) value was not observed at an intermediate stoichiometry value. Instead, both A_s and critical η_{dpa}, increase and decrease, respectively, with increasing Ge content. The correlation between the stoichiometry with the highest A_s value being the easiest to amorphise still exists, as is the case for Ge. This is similar to the amorphisation behaviour of $Al_xGa_{1-x}As$ as shown by Tan *et al.* [9] and discussed earlier in Chapter 1.

5.4 Conclusion

The amorphisation kinetics of $Si_{1-x}Ge_x$ along with those of both Si and Ge have been investigated over the entire stoichiometry range. The value of critical η_{dpa} required to amorphise $Si_{1-x}Ge_x$ decreased with increasing Ge content. This was in stark contrast to the amorphisation kinetics observed in $In_xGa_{1-x}As$ and $In_xGa_{1-x}P$ and has more in common with the amorphisation kinetics observed in $Al_xGa_{1-x}As$.

$Si_{1-x}Ge_x$ has a trimodal bond length distribution consisting of Ge-Ge, Ge-Si and Si-Si bond lengths. The Si-Si bond length does not change significantly with increasing Ge content and remains closer to the original Si-Si value observed in pure Si. The Ge-Ge and Ge-Si bond lengths do vary with increasing Ge content, with the former showing a greater change in bond length than the later. This is also evident from the topological rigidity parameter a** with a higher value of a** suggesting a bigger role of bond bending. It should be noted that both bond bending and bond stretching play a role in accommodating the strain introduced due to change in stoichiometry, the degree of which is indicated by the value of a**.

The observed difference in $Si_{1-x}Ge_x$ amorphisation from that of $In_xGa_{1-x}As$ and $In_xGa_{1-x}P$ can be best understood by considering the DWF for the NNN shell for the materials in question. Compared with both $In_xGa_{1-x}As$ and $In_xGa_{1-x}P$, where the DWF for the NNN shell varies as a function of stoichiometry, the DWF for the NNN shell for $Si_{1-x}Ge_x$ is virtually independent of stoichiometry. This is due to the fact that there is no separate anion – cation sublattice, and nor are there any anti-site defects in $Si_{1-x}Ge_x$ as found in both $In_xGa_{1-x}As$ and $In_xGa_{1-x}P$. It is due to this reduced disorder at the NNN shell that the amorphisation kinetics observed in $Si_{1-x}Ge_x$ are similar to those observed in $Al_xGa_{1-x}As$ as opposed to those of $In_xGa_{1-x}As$ and $In_xGa_{1-x}P$.

Chapter 6 Conclusions and Further Work

This thesis has investigated the amorphisation kinetics of $In_xGa_{1-x}As$, $In_xGa_{1-x}P$ and $Si_{1-x}Ge_x$. The amorphisation behaviour in all three alloys was expected to be similar, and unlike the behaviour observed in $Al_xGa_{1-x}As$, where the amorphisation kinetics are intermediate to the two binary extremes.

The approach taken for each material was to first use RBS-C to study the crystalline to amorphous transformation of implanted materials as a function of stoichiometry, and then to use EXAFS measurements to study the local atomic structure of the materials. By making use of the Hecking model, the RBS-C work yielded the probabilities for both stimulated amorphisation and direct impact amorphisation, helping to determine the dominant mechanism for amorphisation and its relationship to stoichiometry. The EXAFS studies allowed determination of bond lengths, bond angles and DWF; the correlation of this structural information with the observed amorphisation behaviour from the RBS-C work led to an explanation of the amorphisation kinetics in the three systems studied.

Both $In_xGa_{1-x}As$ and $In_xGa_{1-x}P$ were found to have similar amorphisation kinetics, in which some of the stoichiometries amorphised at fluences less than those required to amorphise the two binary extremes in the respective alloys. These alloys were found to have a bimodal bond length distribution, leading to bond angle distortion *and* disorder at the NNN shell. The rapid amorphisation observed in both $In_xGa_{1-x}As$ and $In_xGa_{1-x}P$ was

attributed to this structural disorder which gave rise to preferential sites for stimulated amorphisation.

Similar amorphisation kinetics were expected from $Si_{1-x}Ge_x$, because, like the ternary compounds, $Si_{1-x}Ge_x$ has multimodal bond length distributions, in this case, trimodal. However, its amorphisation kinetics were found to be similar to those observed in $Al_xGa_{1-x}As$. This was due to the much reduced disorder observed at the NNN shell in $Si_{1-x}Ge_x$ compared with both $In_xGa_{1-x}As$ and $In_xGa_{1-x}P$.

It was hence concluded that bond angle distortion and, more importantly, disorder at the NNN shell, were the main reasons for the amorphisation kinetics observed in $In_xGa_{1-x}As$ and $In_xGa_{1-x}P$. Simply having a bimodal (or trimodal) bond length distribution in an alloy is not reason enough to expect rapid amorphisation in that material.

The significance of these findings is that they offer a substantiated explanation for the anomalous amorphisation observed in two ternary compound semiconductors $In_xGa_{1-x}As$ and $In_xGa_{1-x}P$ that are used in the electronics/photonics industry. This could have applications in selecting materials where this type of amorphisation behaviour is desired, because the structural disorder at the NNN, as indicated by its DWF, should predict this anomaly.

Materials that could be usefully investigated along these lines include other ternary compounds such as $Al_xGa_{1-x}N$, $In_xGa_{1-x}N$, $In_xGa_{1-x}Sb$, $Al_xGa_{1-x}Sb$, $Cd_xHg_{1-x}Te$ and $Cd_xZn_{1-x}Te$. If we first consider the $In_xGa_{1-x}N$, $In_xGa_{1-x}Sb$ and $Cd_xZn_{1-x}Te$ systems, the binary constituents of these materials all have a significant difference in lattice constant

similar to that of $In_xGa_{1-x}As$ and $In_xGa_{1-x}P$ (recall Figure 1-1), which could be expected to produce bond angle distributions sufficient to cause anomalous amorphisation behaviour similar to that of $In_xGa_{1-x}As$ and $In_xGa_{1-x}P$. In contrast, $Al_xGa_{1-x}N$, $Al_xGa_{1-x}Sb$ and $Cd_xHg_{1-x}Te$ have lattice constants close together, and hence should show amorphisation kinetics similar to those observed in $Al_xGa_{1-x}As$.

A further area to explore in such materials would be a comprehensive study into the DWF of the NNN shells and the bond angles, to determine whether a threshold value of the bond angle exists at which a given material transitions from amorphisation kinetics similar to those of $In_xGa_{1-x}As$ and $In_xGa_{1-x}P$, over to amorphisation kinetics characteristic of $Al_xGa_{1-x}As$ and $Si_{1-x}Ge_x$.

Appendix

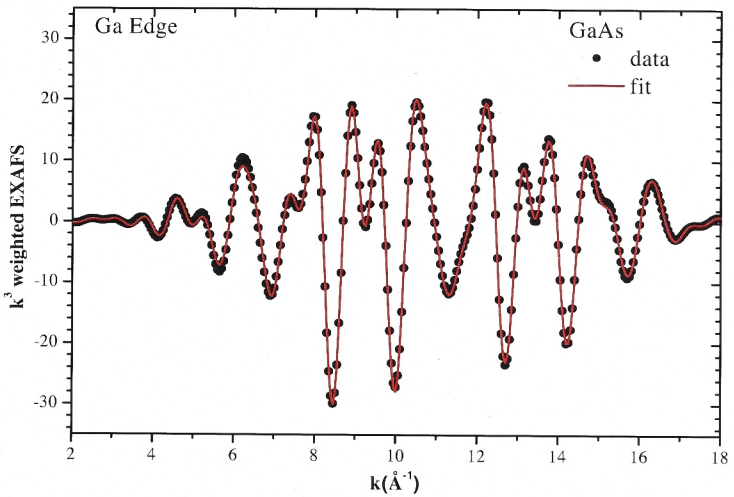

Figure A-1 Best fit for GaAs at the Ga K - edge to k^3 weighted back-transformed experimental data using ARTEMIS.

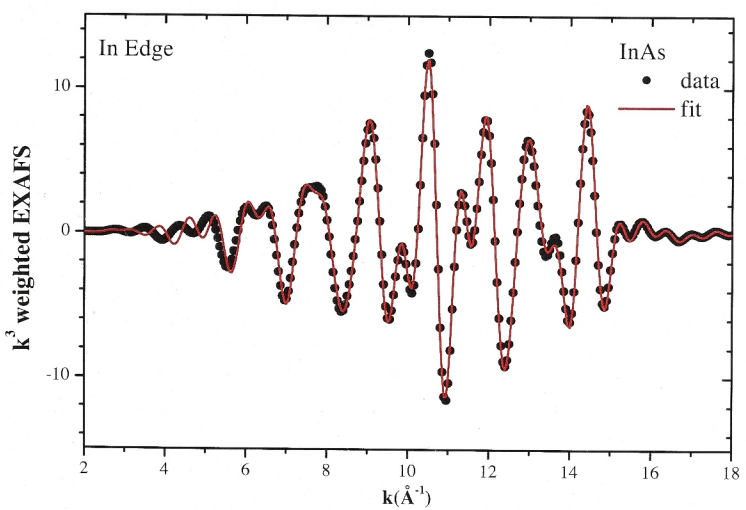

Figure A-2 Best fit for InAs at the In K - edge to k^3 weighted back-transformed experimental data using ARTEMIS.

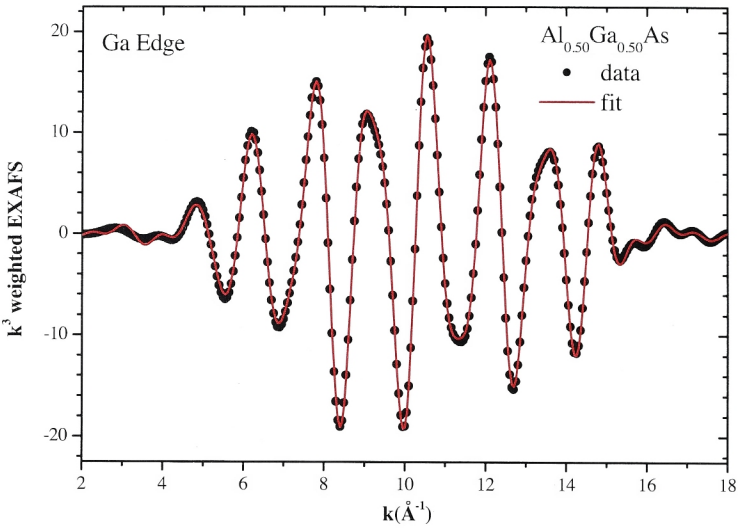

Figure A-3 Best fit for $Al_{0.50}Ga_{0.50}As$ at the Ga K - edge to k^3 weighted back-transformed experimental data using ARTEMIS.

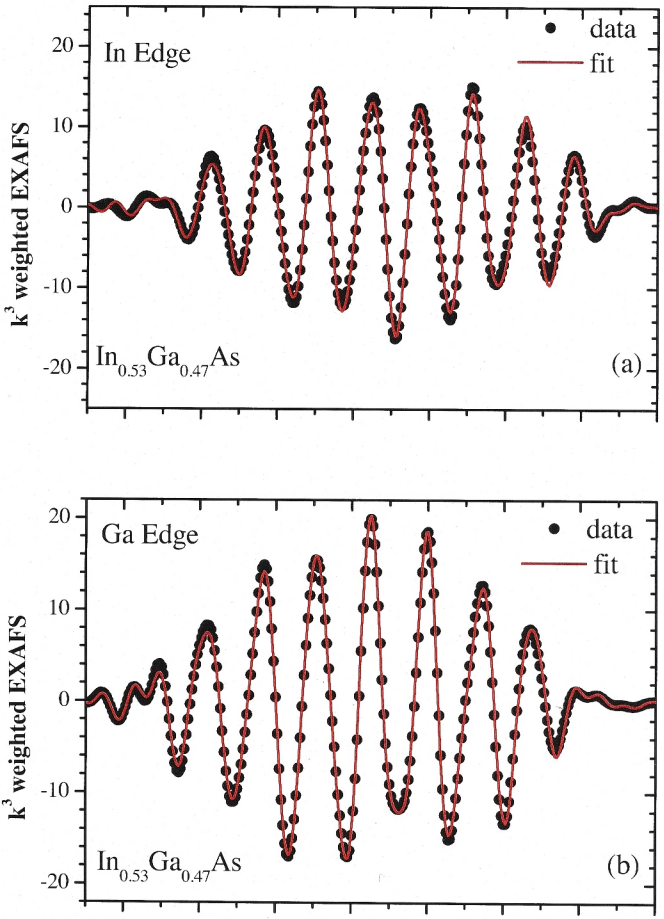

Figure A-4 Best fits for $In_{0.53}Ga_{0.47}As$ at the In and Gas K - edge to k^3 weighted back-transformed experimental data using ARTEMIS.

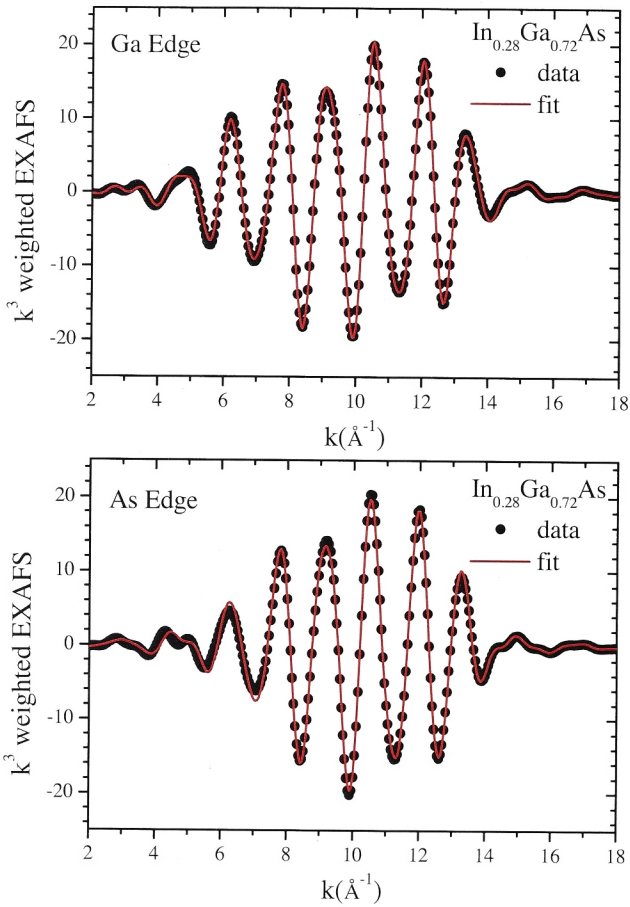

Figure A-5 Best fit for $In_{0.28}Ga_{0.72}As$ at the Ga and As K edge to k^3 weighted back-transformed experimental data using ARTEMIS.

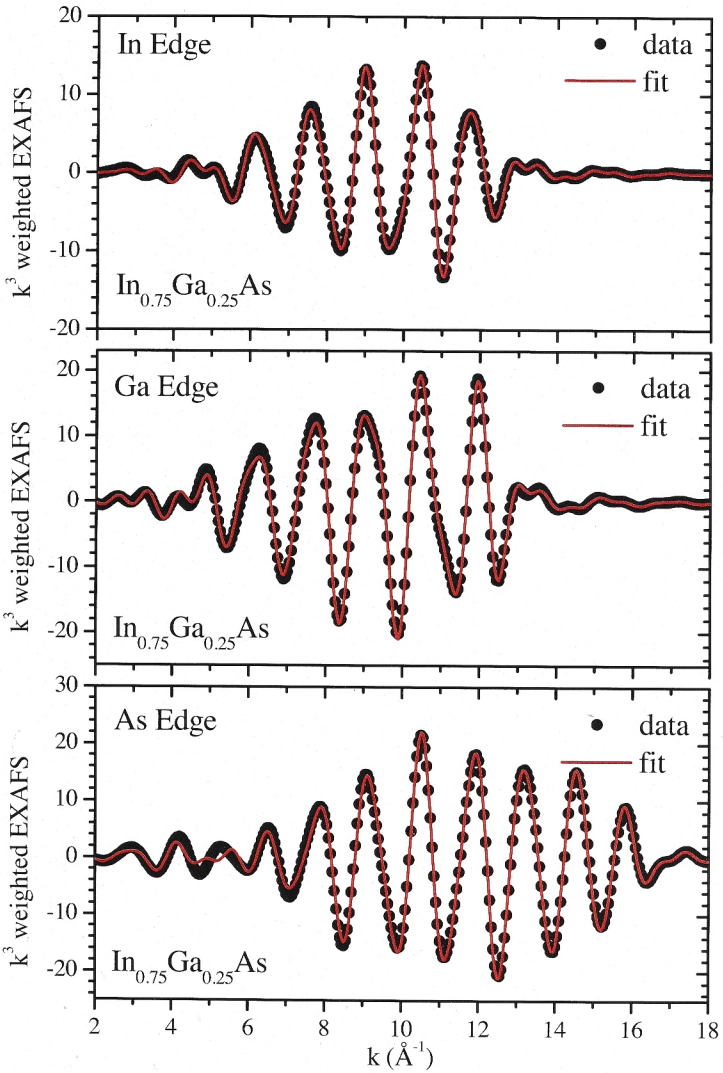

Figure A-6 Best fits for$In_{0.75}Ga_{0.25}As$ at the In, Ga and As K – edge to k^3 weighted back-transformed experimental data using ARTEMIS

Material	Bond (NN/NNN)	Bond Length (Å)						
		Mikkelsen and Boyce		Cai and Thorpe	Glover	Azevedo	This Study	
		NN	NNN	NN	NN	NN	NN	NNN
InAs	In-As	2.622		2.624		2.617 ± 0.006	2.609 ± 0.002	4.273 ± 0.005
GaAs	Ga-As	2.449		2.449	2.448 ± 0.003		2.437 ± 0.002	3.986 ± 0.004
$In_{0.20}Ga_{0.80}As$	In-As/In-In	-	-	2.597	-	-	-	-
	Ga-As/Ga-Ga	-	-	2.456	-	-	-	-
$In_{0.25}Ga_{0.75}As$	In-As/In-In	2.596	4.112	-	-	-	-	-
	Ga-As/Ga-Ga	2.462	4.027	-	-	-	-	-
$In_{0.28}Ga_{0.72}As$	In-As/In-In	-	-	-	-	-	2.594 ± 0.004	-
	Ga-As/Ga-Ga	-	-	-	-	-	2.454 ± 0.002	4.072 ± 0.01
$In_{0.50}Ga_{0.50}As$	In-As/In-In	2.608	4.181	2.607	-	-	-	-
	Ga-As/Ga-Ga	2.469	4.087	2.468	-	-	-	-
$In_{0.53}Ga_{0.47}As$	In-As/In-In	-	-	-	-	-	2.591 ± 0.003	4.176 ± 0.006
	Ga-As/Ga-Ga	-	-	-	-	-	2.466 ± 0.003	4.104 ± 0.012
$In_{0.75}Ga_{0.25}As$	In-As/In-In	2.615	4.239	-	-	-	2.598 ± 0.003	4.192 ± 0.012
	Ga-As/Ga-Ga	2.477	4.128	-	-	-	2.47 ± 0.003	4.133 ± 0.045
$In_{0.80}Ga_{0.20}As$	In-As/In-In	-	-	2.616	-	-	-	-
	Ga-As/Ga-Ga	-	-	2.475	-	-	-	-

Table A-1 Bond lengths for InAs, GaAs and $In_xGa_{1-x}As$ as reported by Mikkelsen and Boyce [40], Cai and Thorpe [39], Glover [79], Azevedo [78] and this study. All values reported here (except for this study) have been read offfrom graphs reported in the above references.

References

[1] J.C. Boisvert, A. Masalykin, G.S. Kinsey, T. Isshiki, M. Haddad, R. Sudharsanan, X. Zheng, and J.C. Campbell, Proc. SPIE **5406** (2004) 13.

[2] http://www.sensorsinc.com/products.html.

[3] J. John, L. Zimmermann, P. Merken, G. Borghs, C.A. Van Hoof, and S. Nemeth, Proc. SPIE **4820** (2003) 453.

[4] J. John, L. Zimmermann, S. Nemeth, T. Colin, P. Merken, S. Borghs, and C.A. Van Hoof, Proc. SPIE **4369** (2001) 692.

[5] S. Prasad, Materials Today **12** (2009) 34.

[6] A. Scavennec, M. Billard, P. Blanconnier, E. Caquot, P. Carer, L. Giraudet, L. Nguyen, F. Lugiez, and J.P. Praseuth, Proc. SPIE **1362** (1991) 331.

[7] S. Adachi, J. Appl. Phys. **58** (1985) R1.

[8] *Properties of Lattice-matched and Strained Indium Gallium Arsenide, EMIS data review series No. 8*, edited by P. Bhattacharya INSPEC, London, 1993.

[9] H.H. Tan, C. Jagadish, J.S. Williams, J. Zou, D.J.H. Cockayne, and A. Sikorski, J. Appl. Phys. **77** (1995) 87.

[10] W. Wesch and M.C. Ridgway, Mater. Sci. Semicond. Process. **7** (2004) 35.

[11] S. Moffatt, Nucl. Instrum. Methods Phys. Res. B **96** (1995) 1.

[12] S.X. Wang, L.M. Wang, and R.C. Ewing, Phys. Rev. B **63** (2000) 024105.

[13] E. Wendler, Mater. Sci. Forum **248 - 249** (1997) 261

[14] E. Wendler, T. Opfermann, and P.I. Gaiduk, J. Appl. Phys. **82** (1997) 5965.

[15] W. Wesch, E. Wendler, T. Bachmann, and O. Herre, Nucl. Instrum. Methods Phys. Res. B **96** (1995) 290.

[16] E. Wendler, Nucl. Instrum. Methods Phys. Res. B **267** (2009) 2680.

[17] J.F. Ziegler, Nucl. Instrum. Methods Phys. Res. B **219-220** (2004) 1027.

[18] I. Jencic, J. Peternelj, and I.M. Robertson, Nucl. Instrum. Methods Phys. Res. B **102** (1995) 202.

[19] R.A. Brown and J.S. Williams, Phys. Rev. B **64** (2001) 155202.

[20] F.F. Morehead and B.L. Crowder, Radiat. Eff. **6** (1970) 27.

[21] J. Nord, K. Nordlund, and J. Keinonen, Phys. Rev. B **65** (2002) 165329.

[22] N. Hecking, K.F. Heidemann, and E.T. Kaat, Nucl. Instrum. Methods Phys. Res. B **15** (1986) 760.

[23] B. Breeger, E. Wendler, C. Schubert, and W. Wesch, Nucl. Instrum. Methods Phys. Res. B **148** (1999) 468.

[24] E. Wendler and P.I. Gaiduk, Nucl. Instrum. Methods Phys. Res. B **136-138** (1998) 488.

[25] W.J. Weber, Nucl. Instrum. Methods Phys. Res. B **166** (2000) 98.

[26] K. Gartner, Nucl. Instrum. Methods Phys. Res. Sect. B-Beam Interact. Mater. Atoms **252** (2006) 190.

[27] K. Gartner, Nucl. Instrum. Methods Phys. Res. Sect. B-Beam Interact. Mater. Atoms **268** (2010) 149.

[28] K. Gartner and T. Clauss, Nucl. Instrum. Methods Phys. Res. Sect. B-Beam Interact. Mater. Atoms **268** (2010) 155.

[29] I. Jencic, M.W. Bench, and I.M. Robertson, J. Appl. Phys. **69** (1991) 1297.

[30] B.W. Lagow, I.M. Robertson, L.E. Rehn, P.M. Baldo, J.J. Coleman, and T.S. Yeoh, J. Mater. Res. **15** (2000) 2043.

[31] B.W. Lagow, B.A. Turkot, I.M. Robertson, J.J. Coleman, S.D. Roh, D.V. Forbes, L.E. Rehn, and P.M. Baldo, IEEE J. Sel. Top. Quantum Electron. **4** (1998) 606.

[32] P. Partyka, R.S. Averback, D.V. Forbes, J.J. Coleman, and P. Ehrhart, J. Appl. Phys. **83** (1998) 1265.

[33] A. Stonert, A. Turos, L. Nowicki, B. Breeger, E. Wendler, and W. Wesch, Mod. Phys. Lett. B **15** (2001) 1437.

[34] A. Stonert, A. Turos, L. Nowicki, B. Breeger, E. Wendler, and W. Wesch, Nucl. Instrum. Methods Phys. Res. Sect. B-Beam Interact. Mater. Atoms **175** (2001) 219.

[35] E.D. Crozier, J.J. Rehr, and R. Ingalls in *X-ray Absorption - Principles, Applications and Techniques of EXAFS, SEXAFS and XANES*, edited by D.C. Koningsberger, R. Prins Vol. 92 John Wiley & Sons, New York, 1988, p. 373.

[36] U.G. Akano, I.V. Mitchell, F.R. Shepherd, and C.J. Miner, Nucl. Instrum. Methods Phys. Res. B **106** (1995) 308.

[37] K.M. Yu in *Microstructural Processes in Irradiated Materials*, edited by S.J. Zinkle, G.E. Lucas, R.C. Ewing, J.S. Williams, MRS Symposium Proceedings Vol. 540 Materials Research Society, Pittsburgh, 1999, p. 79.

[38] K.M. Yu and L. Hsu, Appl. Phys. Lett. **69** (1996) 824.

[39] Y. Cai and M.F. Thorpe, Phys. Rev. B **46** (1992) 15879.

[40] J.C. Mikkelsen and J.B. Boyce, Phys. Rev. B **28** (1983) 7130.

[41] C.S. Schnohr, L.L. Araujo, P. Kluth, D.J. Sprouster, G.J. Foran, and M.C. Ridgway, Phys. Rev. B **78** (2008) 115201.

[42] M.C. Ridgway, K.M. Yu, C.J. Glover, G.J. Foran, C. Clerc, J.L. Hansen, and A.N. Larsen, Phys. Rev. B **60** (1999) 10831.

[43] H. Ryssel and I. Ruge, *Ion Implantation*, John Wiley & Sons Ltd., 1986.

[44] J.F. Ziegler, *Ion Implantation: Science and Technology*, Elsevier Science Publishers, 1992.

[45] http://en.wikipedia.org/wiki/File:ScatteringDiagram.svg.

[46] W. Brandt, Channeling in Crystals from Scientific American, Inc. (1968).

[47] L.C. Feldman, J.W. Mayer, and S.T. Picraux, *Materials Analysis by Ion Channeling-Submicron Crystallography*, Academic Press Inc., New York, 1982.

[48] K. Gartner, K. Hehl, and G. Schlotzhauer, Nucl. Instrum. Methods Phys. Res. B **4** (1984) 55.

[49] W.-K. Chu, J.W. Mayer, and M.-A. Nicolet in *Backscattering Spectrometry*, edited by Vol. Academic Press Inc., New York, 1978, p. 223.

[50] D.E. Sayers, E.A. Stern, and F.W. Lytle, Phys. Rev. Lett. **27** (1971) 1204.

[51] H. Fricke, Phys. Rev. **16** (1920) 202.

[52] R.d.L. Kronig, Zeits. f. Physik **70** (1931) 317.

[53] D.C. Koningsberger and R. Prins, *X-ray Absorption - Principles, Applications, Techniques of EXAFS, SEXAFS and XANES*, John Wiley & Sons, New York, 1988.

[54] E.S. Stern in *X-ray Absorption - Principles, Applications and Techniques of EXAFS, SEXAFS and XANES*, edited by D.C. Koningsberger, R. Prins Vol. 92 John Wiley & Sons, New York, 1988, p. 3.

[55] D.E. Sayers and B.A. Bunker in *X-ray Absorption - Principles, Applications and Techniques of EXAFS, SEXAFS and XANES*, edited by D.C. Koningsberger, R. Prins Vol. 92 John Wiley & Sons, New York, 1988, p. 211.

[56] S.P. Cramer in *X-ray Absorption - Principles, Applications and Techniques of EXAFS, SEXAFS and XANES*, edited by D.C. Koningsberger, R. Prins Vol. 92 John Wiley & Sons, New York, 1988, p. 257.

[57] R. Prins and D.C. Koningsberger in *X-ray Absorption - Principles, Applications and Techniques of EXAFS, SEXAFS and XANES*, edited by D.C. Koningsberger, R. Prins Vol. 92 John Wiley & Sons, New York, 1988, p. 321.

[58] http://en.wikipedia.org/wiki/SOLEIL.

[59] http://www.synchrotron.org.au/index.php/synchrotron-science/how-is-synchrotron-light-created/.

[60] M. Newville, Fundamentals of XAFS http://xafs.org/Tutorials, Consortium for Advanced Radiation Sources, University of Chicago, Chicago, USA (2001).

[61] J.J. Rehr and R.C. Albers, Rev. Mod. Phys. **72** (2000) 621.

[62] J.J. Rehr and R.C. Albers, Phys. Rev. B **41** (1990) 8139.

[63] B. Ravel and M. Newville, J. Synchrotron Radiat. **12** (2005) 537.

[64] M. Newville, J. Synchrotron Radiat. **8** (2001) 322.

[65] J.B. Boyce, T.M. Hayes, and J.C. Mikkelsen, Phys. Rev. B **23** (1981) 2876.

[66] A. Scavennec, M. Billard, P. Blanconnier, E. Caquot, P. Carer, L. Giraudet, L. Nguyen, F. Lugiez, and J.-P. Praseuth, InGaAs/InP monolithic photoreceivers for 1.3-1.5 um optical fiber transmission, Proc. SPIE, 1991, p. 331.

[67] J. John, L. Zimmermann, P. Merken, S. de Groote, G. Borghs, C. Van Hoof, S. Nemeth, and T. Colin, Extended-wavelength InGaAs on GaAs hybrid image sensors in S. Marija (Ed.), Proc. SPIE, 2003, p. 263.

[68] L. Zimmermann, J. John, M.d. Weerd, M. Slaman, S. Nemeth, P. Merken, S. Borghs, and C.A.V. Hoof, InGaAs on GaAs extended wavelength linear detector arrays in J.B. Gail, R. Manijeh (Eds.), Proc. SPIE. SPIE, 2001, p. 77.

[69] S. Arscott, P. Mounaix, and D. Lippens, J. Vac. Sci. Technol. B **18** (2000) 150.

[70] A.R. Clawson, Mater. Sci. Eng. R. **31** (2001) 1.

[71] G.C. DeSalvo, W.F. Tseng, and J. Comas, J. Electrochem. Soc. **139** (1992) 831.

[72] C. Greus, A. Forchel, J. Straka, K. Pieger, and M. Emmerling, J. Vac. Sci. Technol., B **9** (1991) 2882.

[73] Y. Sasaki, T. Katayama, T. Koishi, K. Shibahara, S. Yokoyama, S. Miyazaki, and H. Hirose, J. Electrochem. Soc. **146** (1999) 710.

[74] T.G. Andersson, Z.G. Chen, V.D. Kulakovskii, A. Uddin, and J.T. Vallin, Appl. Phys. Lett. **51** (1987) 752.

[75] J.W. Matthews and A.E. Blakeslee, J. Cryst. Growth **27** (1974) 118.

[76] F.C. Frank and J.H. Vandermerwe, Proc. Roy. Soc. A **198** (1949) 205.

[77] S.P. Edirisinghe, A. Staton-Bevan, P.N. Fawcett, and B.A. Joyce, J. Vac. Sci. Technol. B **13** (1995) 967.

[78] G.d.M. Azevedo, M.C. Ridgway, K.M. Yu, C.J. Glover, and G.J. Foran, Nucl. Instrum. Methods Phys. Res. B **190** (2002) 851.

[79] C.J. Glover, K.M. Yu, M.C. Ridgway, and G.J. Foran, Jpn. J. Appl. Phys. **38** (1999) 548.

[80] L. Vegard, Z. Phys. **5** (1921) 17.

[81] W.L. Bragg, Philos. Mag. **40** (1920) 169.

[82] L. Pauling, *The nature of the chemical bond and the structure of molecules and crystals*, Cornell University Press, Ithaca, NY, 1940.

[83] Y. Cai and M.F. Thorpe, Phys. Rev. B **46** (1992) 15872.

[84] I.K. Jeong, F. Mohiuddin-Jacobs, V. Petkov, S.J.L. Billinge, and S. Kycia, Phys. Rev. B **63** (2001) 205202.

[85] C.S. Schnohr, P. Kluth, L.L. Araujo, D.J. Sprouster, A.P. Byrne, G.J. Foran, and M.C. Ridgway, Phys. Rev. B **79** (2009) 195203.

[86] J. Novak, S. Hasenhohrl, I. Vavra, and M. Kucera, Appl. Phys. A-Mater. Sci. Process. **87** (2007) 511.

[87] W.C. Yang, C. Lo, C.Y. Wei, and W.S. Lour, IEEE Electron Device Lett. **32** (2011) 1412.

[88] Y.A. Chang, Z.Y. Li, H.C. Kuo, T.C. Lu, S.F. Yang, L.W. Lai, L.H. Lai, and S.C. Wang, Semicond. Sci. and Tech. **24** (2009).

[89] H.P.T. Nguyen, K.H. Kim, H. Lim, and J.J. Lee, International Workshop on Advanced Material for New and Renewable Energy **1169** (2009) 149.

[90] S.A. Ringel, et al., Progress in Photovoltaics **10** (2002) 417.

[91] T. Takamoto, E. Ikeda, H. Kurita, and M. Ohmori, Appl. Phys. Lett. **70** (1997) 381.

[92] M. Yamaguchi, Solar Energy Materials and Solar Cells **68** (2001) 31.

[93] M. Yamaguchi, Solar Energy Materials and Solar Cells **75** (2003) 261.

[94] M. Yamaguchi, T. Okuda, and S.J. Taylor, Appl. Phys. Lett. **70** (1997) 2180.

[95] M. Yamaguchi, T. Okuda, S.J. Taylor, T. Takamoto, E. Ikeda, and H. Kurita, Appl. Phys. Lett. **70** (1997) 1566.

[96] E. Bezakova, A.P. Byrne, C.J. Glover, M.C. Ridgway, and R. Vianden, App. Phys. Lett. **75** (1999) 1923.

[97] J. Krynicki, A. Kozanecki, W. Szyszko, and R. Groetzschel, Radiat. Eff. **115** (1990) 219.

[98] K.S. Jones and C.J. Santana, J. Mater. Res. **6** (1991) 1048.

[99] C.S. Schnohr, P. Kluth, A.P. Byrne, G.J. Foran, and M.C. Ridgway, Phys. Rev. B **77** (2008) 073204.

[100] J.B. Boyce and J.C. Mikkelsen Jr, J. Cryst. Growth **98** (1989) 37.

[101] E. Wendler in *Application of Accelerators in Research and Industry*, edited by J.L. Duggan, I.L. Morgan Vol. 680, 2003, p. 670.

[102] E. Wendler, B. Breeger, C. Schubert, and W. Wesch, Nucl. Instrum. Methods Phys. Res. Sect. B-Beam Interact. Mater. Atoms **147** (1999) 155.

[103] W. Wesch, E. Wendler, G. Gotz, and N.P. Kekelidse, J. Appl. Phys. **65** (1989) 519.

[104] P. Auvray, A. Guivarc'h, H. L'Haridon, G. Pelous, M. Salvi, and P. Henoc, J. Appl. Phys. **53** (1982) 6202.

[105] V.L. Wrick, W.J. Choyke, and C.F. Tzeng, Electronics Letters **17** (1981) 752.

[106] B. Breeger, E. Wendler, C. Schubert, and W. Wesch, Nucl. Instrum. Methods Phys. Res. B **161-163** (2000) 415.

[107] N.P. Tognetti, G. Carter, D.V. Stevanovic, and D.A. Thompson, Radiat. Eff. **66** (1982) 15.

[108] M. Kondow, H. Kakibayashi, and S. Minagawa, J. Cryst. Growth **88** (1988) 291.

[109] M. Zorn, et al., Phys. Rev. B **60** (1999) 8185.

[110] F. Léonard and R. Desai, Thin Solid Films **357** (1999) 46.

[111] A. Turos, A. Stonert, B. Breeger, E. Wendler, W. Wesch, and R. Fromknecht, Nucl. Instrum. Methods Phys. Res. Sect. B-Beam Interact. Mater. Atoms **148** (1999) 401.

[112] B. Breeger, E. Wendler, W. Trippensee, C. Schubert, and W. Wesch, Nucl. Instrum. Methods Phys. Res. B **174** (2001) 199.

[113] M. Kahn and D. Ritter, Appl. Phys. Lett. **79** (2001) 2928.

[114] W. Wesch, E. Wendler, Z.S. Hussain, S.M. Kluth, and M.C. Ridgway, Nucl. Instrum. Methods Phys. Res. B **242** (2006) 480.

[115] E. Wendler and W. Wesch in *Advances in Solid State Physics*, edited by B. Kramer Vol. 44, 2004, p. 339.

[116] E. Wendler and W. Wesch, Nucl. Instrum. Methods Phys. Res. B **242** (2006) 562.

[117] *Ternary and Multinary Compounds*, edited by A. Zunger, S.K. Deb Materials Research Society, Pittsburgh, PA, 1987.

[118] J.C. Aubry, T. Tyliszczak, A.P. Hitchcock, J.M. Baribeau, and T.E. Jackman, Phys. Rev. B **59** (1999) 12872.

[119] T.E. Haynes and O.W. Holland, Nucl. Instrum. Methods B **80-81** (1993) 901.

[120] T.E. Haynes and O.W. Holland, Appl. Phys. Lett. **61** (1992) 61.

[121] A.N. Larsen, et al., J. Appl. Phys. **81** (1997) 2208.

[122] J.K.N. Lindner, Nucl. Instrum. Methods Phys. Res. B **127-128** (1997) 401.

[123] D.Y.C. Lie, A. Vantomme, F. Eisen, J.T. Vreeland, M.A. Nicolet, T.K. Carns, V. Arbet-Engels, and K.L. Wang, J. Appl. Phys. **74** (1993) 6039.

[124] D.Y.C. Lie, J. Electron. Mater. **27** (1998) 377.

[125] S. Decoster and A. Vantomme, J. Phys. D: Appl. Phys. **42** (2009).

[126] D.B. Aldrich, R.J. Nemanich, and D.E. Sayers, Phys. Rev. B **50** (1994) 15026.

[127] H. Kajiyama, S.-i. Muramatsu, T. Shimada, and Y. Nishino, Phys. Rev. B **45** (1992) 14005.

[128] N. Mousseau and M.F. Thorpe, Phys. Rev. B **48** (1993) 5172.

[129] M.C. Ridgway, et al. in *Applications of Synchrotron Radiation Techniques to Materials Science IV*, edited by S.M. Mini, S.R. Stock, D.L. Perry, L.J. Terminello Vol. 524 Materials Research Society, Warrendale, 1998, p. 309.

[130] N. Mousseau and M.F. Thorpe, Phys. Rev. B **46** (1992) 15887.

[131] L.L. Araujo, G.J. Foran, and M.C. Ridgway, J. Phys.-Condes. Matter **20** (2008).

[132] Z. Sun, S. Wei, A.V. Kolobov, H. Oyanagi, and K. Brunner, Phys. Rev. B **71** (2005) 245334.